UNIVERSITY OF CALIFORNIA SAN DIEGO

A study on faceted particle formation of perovskites and oxidation behavior of carbides

A Dissertation submitted in partial satisfaction of the requirements
for the degree Doctor of Philosophy

in

Materials Science and Engineering

by

Maritza Sanchez

Committee in charge:

Professor Olivia A. Graeve, Chair
Professor Javier Garay
Professor Jian Luo
Professor Vitali Nesterenko

2023

The Dissertation of Maritza Sanchez is approved, and it is acceptable in quality and form for publication on microfilm and electronically.

University of California San Diego

2023

DEDICATION

This dissertation and my doctoral degree are dedicated to my parents and little sister, Jose Reyes Sanchez, Maria Del Rocio Bernal, and Nohely Sanchez. Without their love and support none of this would have been possible. I love you all with everything that I have and everything that I am. This Ph.D. degree is dedicated to my Abuelita Chelo, the strongest and most resilient person I know. Rest and peace. I love and miss you every day.

TABLE OF CONTENTS

LIST OF FIGURES

LIST OF TABLES

LIST OF ABBREVIATIONS

BT	Barium Titanate
ST	Strontium Titanate
XRD	X-ray Diffraction
SEM	Scanning electron microscopy
TEM	Transmission electron microscopy
TaC	Tantalum Carbide
HfC	Hafnium Carbide

ACKNOWLEDGEMENTS

To my family, especially my parents who made me being here possible. This degree is for you both. Your hard work and sacrifices have given the opportunity to become a doctora and a professor.

To my little sister, I hope that I have served as a good role model for you. I hope that you feel like you can achieve anything that you set your mind to because you are intelligent and powerful.

To my partner, who went through the roller coaster of graduate school emotions with me. Your support does not go unnoticed. Thank you always listening and doing all the little things that meant so much.

To my graduate school friends and lab mates, Robyn Ridley, Ingram Vargas, Jordan Campbell, Fabian Martinez, Ivan Torres, Stephanie Ortega. You all made this experience doable. You reminded me of my potential, and your help will forever by appreciated. You are all absolutely amazing and some of the best people I have ever met. We have built lifelong friendships.

To my mentors, Mauro Rodriguez, Shana Slebioda, and Nancy Ronquillo. You are all my role models and my biggest support system. Thank you for sharing all your resources and knowledge.

To my dog, Loki. Thank you for being my emotional support through my last couple of years in graduate school.

To Paul and Jin, thank you for being the best dynamic research duo a person can ask for. I literally would not have made it to this point without all your help and hours spent in the lab. You both pushed me to become a better mentor, researcher, and scholar.

Chapter 1, in part is currently being prepared for submission for publication of the material. Sanchez, Maritza; Barraza, Paul; Zhou, Jin; and Graeve, Olivia, A. The dissertation author was the primary author of this chapter.

Chapter 2, in part is currently being prepared for submission for publication of the material. Sanchez, Maritza; Barraza, Paul; Ayars, Jarren; Zhou, Jin; and Graeve, Olivia, A. The dissertation author was the primary author of this chapter.

Chapter 3, in part, has been submitted for publication of the material as it may appear in Advanced Engineering Materials, 2023, Sanchez, Maritza; Acord, Katherine A., Freuh, Samuel, Rueschhoff, Lisa M., Graeve, Olivia A., Wiley, 2023. The dissertation author was the primary researcher and author of this paper.

VITA

2016 Bachelor of Science in Mechanical Engineering, California State University, Los Angeles

2017 Master of Science in Materials Science and Engineering, University of California, San Diego

2023 Doctor of Philosophy in Materials Science and Engineering, University of California San Diego

PUBLICATIONS

First author:

M. Sanchez, K.A. Acord, S. Frueh, L.M. Rueschhoff, O.A. Graeve, "Phase transitions and oxidation behavior during oxyacetylene torch testing of TaC-HfC solid solutions", Advanced Engineering Materials, April 2023, 2300138. DOI: 10.1002/adem.202300138

Co-author:

J. Ha, E. Novitskaya, N. Lam, **M. Sanchez**, Y.H. Kim, Z. Li, W.B. Im, O.A. Graeve, J. McKittrick, "Synthesis of Mn4+ activated Na2SiF6 red-emitting phosphors using an ionic liquid,", Journal of Luminescence, Volume 218, Feb 2020, 116835. DOI: 10.1016/j.jlumin.2019.116835

J. Ha, Y.H. Kim, E. Novitskaya, **M. Sanchez**, O.A. Graeve, W.B. Im, S.P. Ong, and J. McKittrick, "ColorTunable Single-phase Eu2+ and Ce3+ Co-activated Sr2LiAlO4 Phosphors," Journal of Materials Chemistry C, in print (2019). DOI: 10.1039/C8TC05777J

ABSTRACT OF THE DISSERTATION

A study on faceted particle formation of perovskites and oxidation behavior of carbides

by

Maritza Sanchez

Doctor of Philosophy in Materials Science and Engineering

University of California San Diego, 2023

Professor Olivia A. Graeve, Chair

Perovskite materials, specifically barium titanate (BT) and strontium titanate (ST), hold significant potential for a range of applications, including ferroelectric devices and multilayer capacitors. The particle morphology of these materials can significantly influence their electronic properties, such as their dielectric constant and ferroelectric behavior. Our study aims to understand the formation mechanisms of faceted particles of BT and ST, synthesized using both molten hydrothermal and aqueous hydrothermal methods. Our experimental results obtained

through scanning electron microscopy (SEM) reveal successful development of faceted particles for BT using the molten hydrothermal method and for ST using the aqueous hydrothermal method. However, X-ray diffraction results indicate the presence of unreacted $SrCO_3$ and an amorphous structure in the ST sample synthesized by the molten hydrothermal method, pointing towards an in-situ growth mechanism of ST. Transmission electron microscopy (TEM) results suggest that the formation of faceted particles occurs through the aggregation of smaller crystallites in identical crystallographic directions. This research provides valuable insights into the particle morphology control of perovskite materials through different synthesis methods, shedding light on their potential in advanced electronic applications.

Tantalum carbide (TaC) and hafnium carbide (HfC) have some of the highest melting temperatures among the transition metal carbides, borides, and nitrides, making them promising materials for high-speed flight and high temperature structural applications. Solid solutions of TaC and HfC are of particular interest due to their enhanced oxidation resistance compared to pure TaC or HfC. This study looks at the effect of Hf content on the oxidation resistance of TaC-HfC sintered specimens. Five compositions (100 vol.% TaC, 80 vol.% TaC + 20 vol.% HfC, 50 vol.% TaC + 50 vol.% HfC, 20 vol.% TaC + 80 vol.% HfC, and 100 vol.% HfC) were fabricated into bulk samples using spark plasma sintering (2173 K, 50 MPa, 10 min hold). Oxidation behavior of a subset of the compositions (100 vol.% TaC, 80 vol.% TaC + 20 vol.% HfC, and 50 vol.% TaC + 50 vol.% HfC) was analyzed using an oxyacetylene torch for 60 s. The TaC-HfC samples exhibited a reduction in the oxide scale thickness and the mass ablation rate with increasing HfC content. The improved oxidation resistance can be attributed to the formation of a $Hf_6Ta_2O_{17}$ phase. This phase enhances oxidation resistance by reducing oxygen diffusion and serving as a protective layer for the unoxidized material. The superior oxidation resistance of

TaC-HfC samples makes these materials strong contenders for the development of high-speed flight coatings.

INTRODUCTION

Morphology control of particle has been a growing interest because of the improvements in material properties. Particularly for oxide materials, this suggests enhanced electronic, magnetic, chemical, and optical properties. Controlling the final particle morphology requires manipulation of the surface energies of crystallographic facets. Reducing the energy of traditionally high energy crystal faces allows for other orientations with traditional lower surface energies to grow. The growth in these untraditional crystallographic directions is what enables the development of unique particle morphologies. Cubic particles are particularly interesting because of their ability to self-assemble into ordered arrangements. The flat faces of the cubic particles also allow for each particle to sit compactly with its 6 neighboring cubes. The ability to create a compact, ordered structure of cubic particles also reduces the amount of void space in between particles and permits good cube-to-cube contact. The ordered structure and the reduction of porosity can also lead to enhanced bulk properties of the material.

Different synthesis methods have been used to create cubic particles of different oxide materials. Depending on the type of synthesis method used, different synthesis parameters and additions will affect the outcome of the particle morphology. Many synthesis methods utilize hydroxides or salts to create a synthesis environment that produces a slow enough reaction to allow the particles to form distinct morphologies. The addition of additives and surfactants also help in reducing the surface energies of specific crystallographic planes, which depends on the starting precursors and the type of surfactant used. These are the most common methods used to obtain cubic particle morphologies of oxide materials.

In this thesis, we analyze the particle morphology of barium titanate and strontium titanate using two synthesis methods (molten hydrothermal and aqueous hydrothermal). Identifying the correct synthesis method and synthesis parameters are vital in the final particle morphology. Perovskites like barium and strontium titanate are a good starting point in attempting to also understand how the cubic particles form and what are some of the growth mechanisms associated with them. Through the analysis

of these materials, we hope to be able to apply these methods to other materials as well in attempts to control the particle morphology.

The second project of this thesis looks at the oxidation resistance of tantalum carbide and tantalum carbide-hafnium carbide solid solutions with an oxyacetylene torch. Tantalum and hafnium carbide have some of the highest melting temperatures among all the carbides making them ideal candidates for applications like high-speed flight. Tantalum carbide alone has been shown to have low oxidation resistance and would not be suitable for these applications because of that. The addition of hafnium carbide is a promising solution to attempt to improve the oxidation resistance of hafnium carbide. This project looks at identifying the composition of tantalum carbide and hafnium carbide that shows the highest oxidation resistance. This study will also provide a more comprehensive understanding of the oxidation behavior of these materials in different torch environments to complement previous studies conducted in a plasma torch environment.

Chapter 1 Formation of cubic particle morphologies of oxide materials

1.2 Introduction

Controlling the size and morphology of ceramic materials, particularly oxides, has been growing interest because of the ability to use them as molecular building blocks to control the properties of the material at the bulk scale. Different morphologies give rise to unique properties that can be enhanced at the bulk scale by manipulating the exposed crystal facets of the particle and building ordered arrangements of superlattices from the molecular building blocks.

Previous studies have shown that particles with non-traditional morphologies like cubic or polyhedron can be arranged into closely packed superlattices [1][2][3][4][5][6][7][8][9][10][11][12][13][14][15]. The unique morphology of the particles and the ability to order them into superstructures have allowed for enhancements in various material properties (i.e., electric, magnetic, structural). For piezoelectric ceramic materials like perovskites, thin film ordered superlattices of cubic particles have shown enhancements of the electronic properties like the dielectric constant [16][17][18][19]. The faceted sides of the particles allow for more compact placement, reducing the overall porosity of the thin film. The reduction of pores leads to overall better dielectric performance. Similarly other type of oxide materials like nickel oxide have also shown an enhancement in their optical activity and catalytic response [36]. These early studies on the effect of particle morphology on the properties of the material have made understanding the formation mechanisms behind unique morphologies important. Cubic particle morphologies are especially interesting because of their exposed facets, tendency to self-organize into ordered arrangements, and the facile ways in creating them.

Overall, the biggest driving force that dictates the final particle morphology of a material is the surface energies of the crystallographic planes. By stabilizing the certain crystal planes, other

crystallographic orientations are allowed to grow to form these unique particle structures. The surface energies of certain crystallographic planes can be manipulated through a number of different ways that will be discussed here. The goal of this chapter is to understand why cubic particles of oxides form and under what conditions.

1.3 Nickel Oxide, AO

Oxides with an AO structure, like nickel oxide (NiO) have had applications as catalysts [20][21], electrode materials for lithium ion batteries and fuel cells [22][23][24], electrochemical supercapacitors [25][26][27], magnetic materials [28], thin film transistors [29][30], UV photo detectors [31], and organic/inorganic solar cells [32]. Controlling the particle morphology of nickel oxide can lead to improved photocatalytic and optoelectronic properties.

NiO nanocubes have been previously synthesized through a number of methods, including a surfactant-assisted [33], sol-gel [34][35], and chemical precipitation methods [36]. For the surfactant-assisted synthesis, cetyltrimethylammonium bromide (CTAB) or sodium dodecyl sulfate (SDS) were used as surfactants through a microemulsion strategy [33]. The type of surfactant used was the main indicator on the final particle morphology of NiO. The addition of CTAB led to the formation of rods and the addition of SDS produced cubic morphologies (Figure 1). The surfactant was suggested to act as a template for the formation of specific particle structures. Other synthesis studies, have shown that indeed cubic particles can be formed with the addition of CTAB but it is highly dependent on the amount that is added to the synthesis [34]. The addition of 5% CTAB was shown to produce cubic particles. At low concentrations of surfactant, the final morphology that forms can be attributed to the interactions between the metal ions and the head of the surfactants (Figure 2).

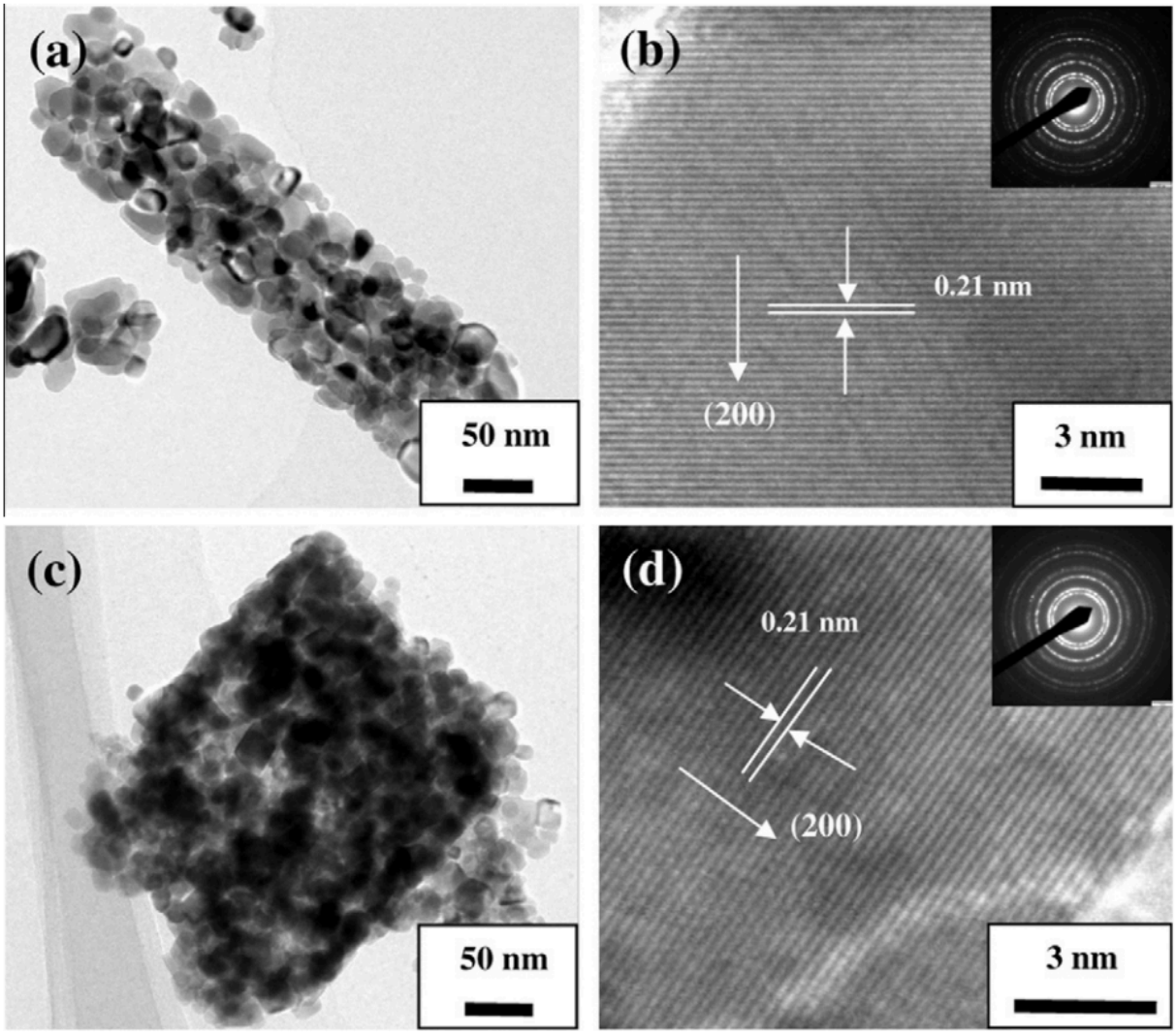

Figure 1 Particle morphologies of NiO using (a) CTAB and (b) SDS as the surfactant [33].

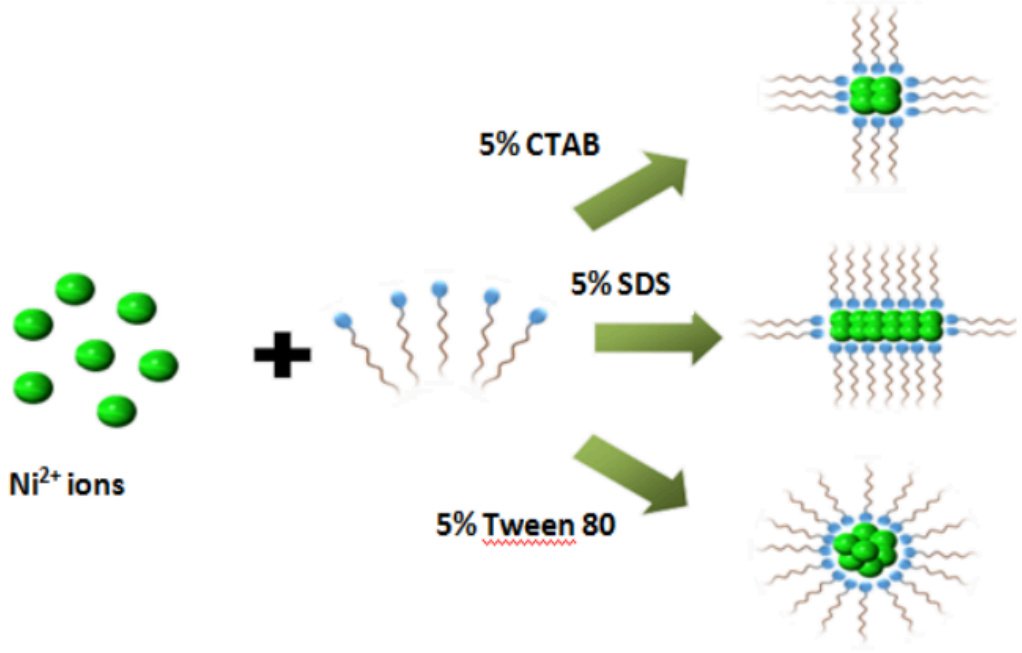

Figure 2 Interactions between metal ions and surfactant used in the synthesis of NiO to produce various particle morphologies [34].

Understanding the formation of cubic particle morphology in NiO is crucial in developing enhanced materials. Previous studies have shown preliminary data on the improved optical properties of NiO nanocubes [36]. Sheen, et al found that in combination with electron irradiation the optical activity and photo response of NiO nanocubes can be enhanced. This study has begun to show the potential of improved properties of AO materials with cubic particle morphology.

1.4 Cerium Oxide, AO_2

Oxides with an AO_2 structures, like cerium oxide or ceria (CeO_2) have had applications as catalysts [37], fuel cells, solar cells, UV blocks, oxygen sensors, polishing materials [38], water splitting, oxygen storage, and the oxidation of volatile organic constituents [39]. The

development of ceria particles with specific particle morphologies, like cubic particles, can enhance the catalytic behavior and as well as other properties.

Ceria cubic particle morphologies have been synthesized primarily by a hydrothermal method [40][41][42][43][38][44][45][46][47][48] or a microwave-assisted synthesis method [49][39][50][51]. Other synthesis methods have been less frequently employed like a gradual hydrolysis of cerium chloride solution [52] and a surfactant-assisted colloidal synthesis [53]. Various research studies have looked at the factors that influence the particle morphology for each of these synthesis methods.

The hydrothermal method has been employed with and without the addition of surfactants and additives. For the hydrothermal synthesis without the use of surfactants, the factors that affect the formation of cubic particle morphologies are the precursors used and the basicity of the solution [40][54][50][43]. The use of cerium nitrate $Ce(NO_3)_2$ has been shown to produce ceria cubic particles over other precursors like cerium acetate and cerium chloride [43]. The NO^{-3} oxidizing anion allows cerium (III) ions to oxide to form ceria and their preferential absorbance onto the {100} planes changed the surface energy of the ceria crystals formed which led to {100} enclosed planes [43]. This allowed for the development of ceria cubic particles. Not only does utilizing cerium nitrate as a precursor help in the formation of cubic particles but so does the pH of the solution. In order to make the solution basic, cerium nitrate could be used as a precursor or a nitrate salt like sodium nitrate $NaNO_3$ could be incorporated into the synthesis [54]. The formation of nanocubes is related to dissolution-recrystallization process that happens because of the basic conditions that the nitrate precursor or salt create. The NO^{3-} ions from the nitrate precursor or salt absorb onto the {100} surfaces of ceria nuclei producing cubic particles enclosed in {100} planes (Figure 3) [54].

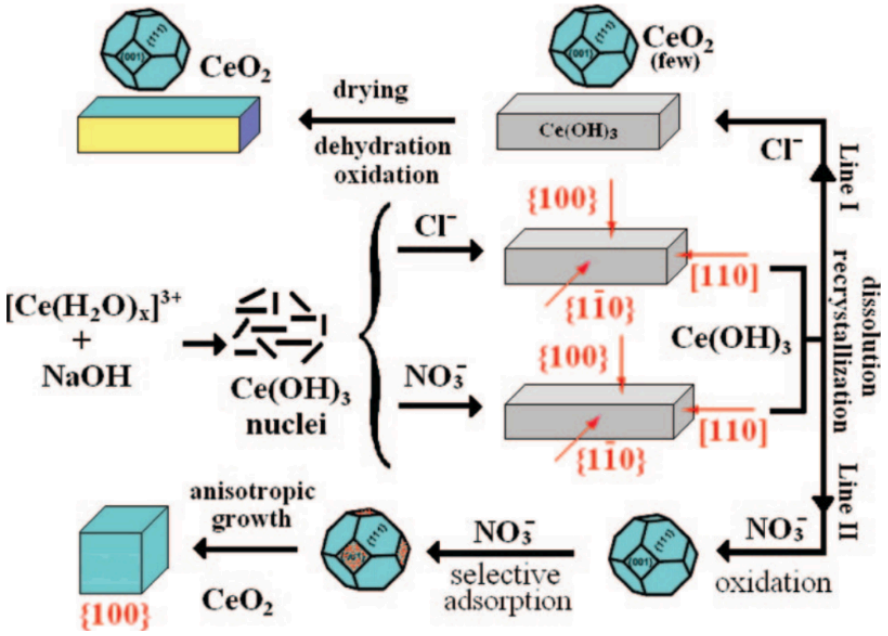

Figure 3 Diagram of the formation mechanism of ceria cubic particles through conversion from nanorods [54].

The hydrothermal synthesis of ceria has also been conducted with the use of dopants, surfactants and/or additives. A urea-assisted hydrothermal synthesis method has been employed to create cubic particles of ceria [41]. A high concentration of urea causes saturation of the aqueous phase which results in the coalition of nanocrystals in a mutual crystallographic direction. Gradual hydrolysis synthesis of ceria nanocubes has also shown that the addition of polyvinylpyrrolidone (PVP) promotes the growth of cubic particle morphology [52]. Experiments that did not have the addition of PVP did not show the cubic particle morphology. The addition of other additives like NH_4Cl can also allow for the development of hollow cubic particle structures (Figure 4) [52].

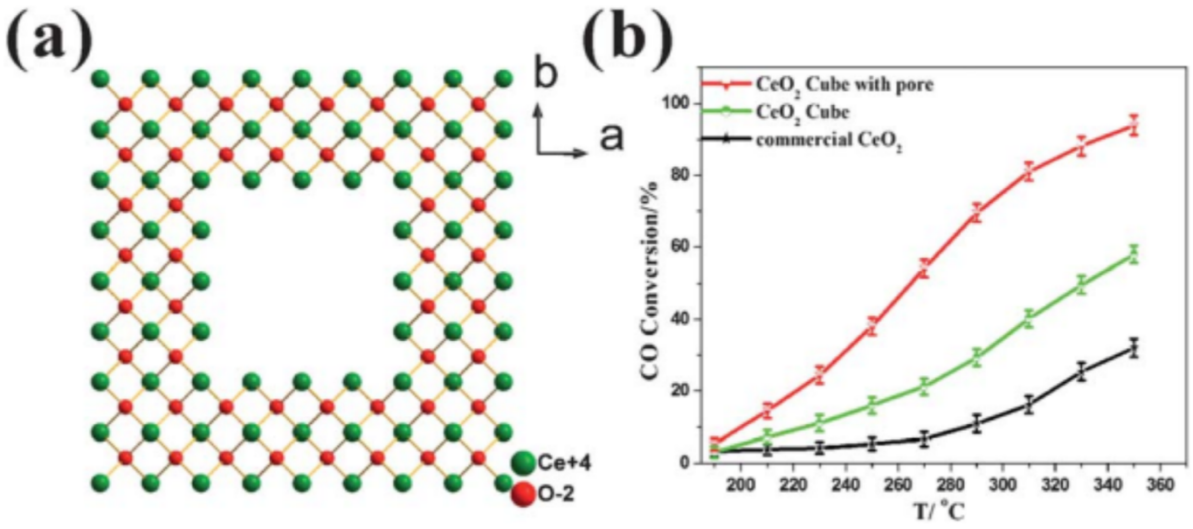

Figure 4 (a) Hollow cubic ceria particle structure and (b) percent conversion of CO in the presence of ceria particles [52].

The addition of lanthanides as dopants have also been shown to produce cubic particles of ceria (Figure 5) [55]. Low concentrations of dopants ($0.05<x<0.1$) enable the development of ceria nanocubes. Specific dopants like Gadolinium and Samarium greatly facilitate the growth of ceria nanocubes by creating more oxygen vacancies or defects thus increasing the surface area of the particles [55]. The higher surface energy of the particles leads to the formation of the cubic morphology. Other groups have used surface modifying agents, like sodium nitrate, to control the growth of certain crystallographic directions, where the surface modifying agents bind to facets and change formation energy to enhance or prevent growth in these facets [49]. More specifically the added nitrate ions increase the chemical potential which allows for stronger binding of the ions on the {100} faces of the ceria nuclei [41] [43].

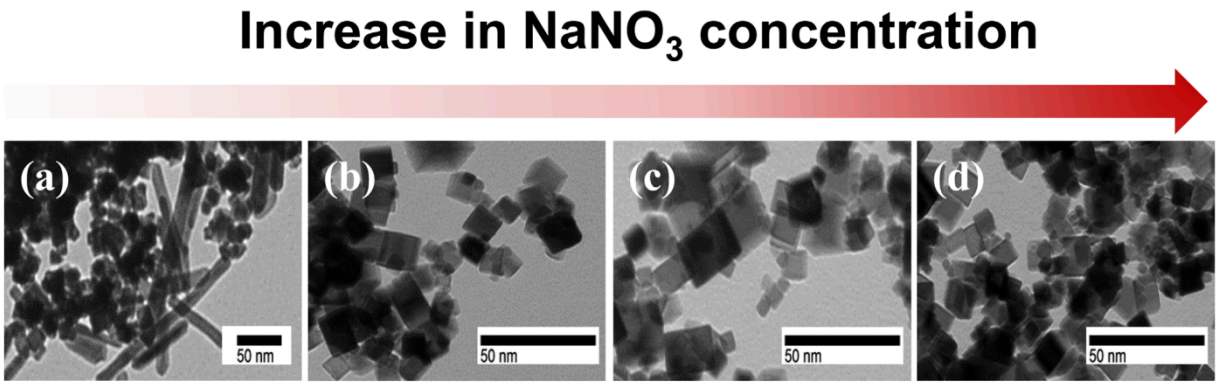

Figure 5 Morphology of ceria particles with increasing $NaNO_3$ concentration. Larger cubic particles are formed with higher $NaNO_3$ concentration [49].

There have been extensive studies on the development of cubic particles of ceria. Overall the addition of surfactants, dopants, and additives lead to a controlled growth of specific crystallographic orientations that promote the formation of cubic particles.

1.4 Perovskite, ABO_3

Perovskite materials like barium titanate ($BaTiO_3$) and strontium titanate ($SrTiO_3$) have been of great interest for applications as ferroelectrics, multilayer capacitors, thermistors, transducers and infrared detectors [56][57][58]. Controlling the particle morphology of these materials has opened new opportunities for increased electronic properties like enhanced dielectric constants. Specifically, the cubic particle structure lattice defects within the interface region of cubes allows for a higher dielectric constant of the material [57].

These faceted particle structures have been synthesized through a number of methods including molten salt [59][60], microwave-assisted [61], composite-hydroxide [62][63][64][65], solvothermal [66], and aqueous surfactant-assisted [56][12][57][67][13][16][14][68][69]. Depending on the type of synthesis there are several parameters that have a strong effect on the

type of morphology that forms for perovskite materials. These synthesis methods allow for the slow and controlled formation of specific crystal facets.

In the composite-hydroxide-mediated method, the melting point of the hydroxides is a lot lower, so it allows for reduced temperatures to be used to synthesize these perovskite materials [63]. An ample amount of time for the reaction to occur and begin to grow the crystal facets is also important [60]. Shorter synthesis times do not allow for crystals to grow into well-defined cubic particles. Synthesis times below 12 hours yield small percentages of faceted morphologies with a majority of sphere-like or random morphologies. The longer synthesis times, typically greater than 12 hours, allow for a slower and controlled environment in which small crystals can add on to each other to form clear faceted cubic particles (Figure 1). Typical synthesis times that form clear faceted cubic morphologies range from 12-24 hours for strontium titanate [60] and 24-48 hours for barium titanate [63]. The addition of the hydroxides facilitates the nucleation of barium and strontium titanate from the precursor materials. To reduce the overall energy of the system the nucleates begin to aggregate to form larger particles [62]. These aggregates can then form cubic particle morphologies through a surface reconstruction (Figure 2). Salts like sodium chloride (NaCl) and potassium chloride (KCl) have also been used in molten-salt synthesis of barium titanate [59]. The scale of the cubic particles are in the nano regime and had sizes ranging from 70-100 nm depending on the time and temperature of the synthesis [63]. Other growth mechanisms have also been observed for specific structures of starting materials. Titania (TiO_2) nanorods used as a precursor material, along with metal salts and NaOH, for the synthesis of barium and strontium titanate has led to the development of cubic particle morphologies [60] (Figure 3). Yang, et al showed that 180°C and time over 12 hours was crucial in developing the cubic particle morphologies with smooth surfaces.

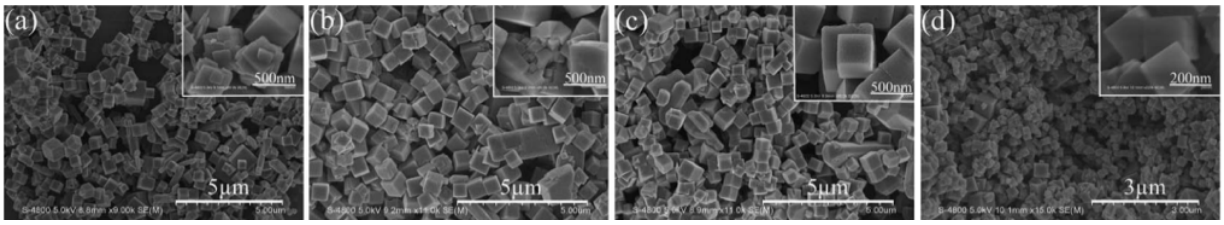

Figure 6 Influence of time on synthesis of strontium titanate for 1, 3, 6, and 12 hours [60].

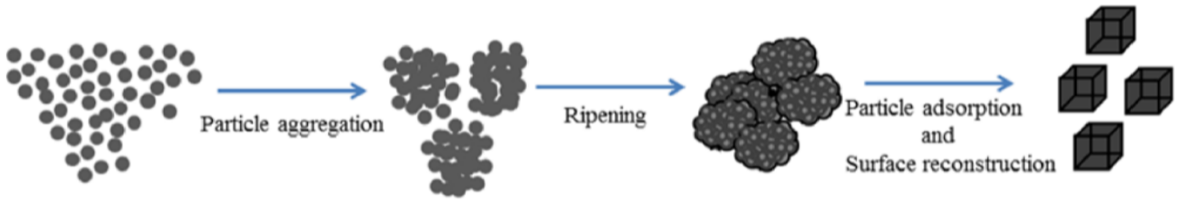

Figure 7 Growth mechanism of barium titanate through the composite-hydroxide-mediated synthesis method [7].

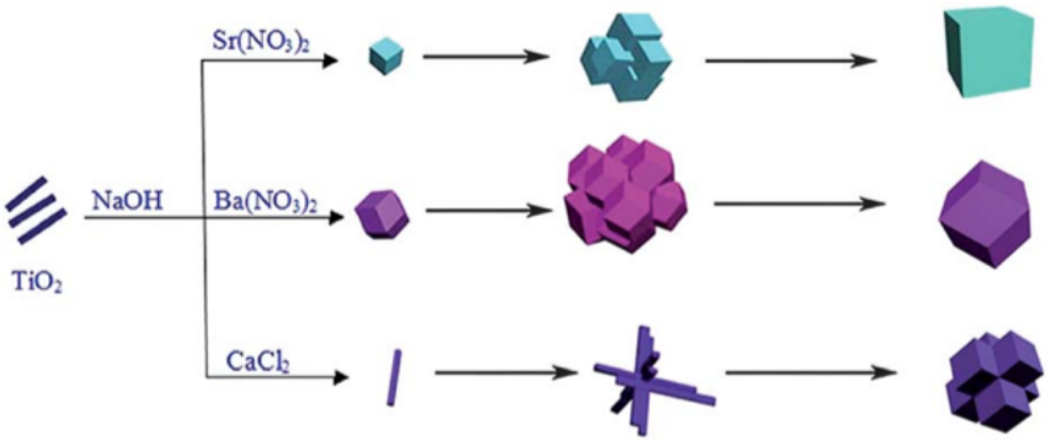

Figure 8 Growth mechanism using titania nanorods as a precursor for the synthesis of strontium titanate and barium titanate faceted morphologies [5].

For aqueous synthesis methods there many parameters that play a role in the formation of cubic morphologies of perovskite materials, this includes type of solvent used, pH of solution, and the addition of surfactants. Solvents like hexane, toluene, 1-butanol, 1-decanol, phenyl ether, and benzyl ether have been used to synthesize cubic particles [11]. The polarity of the solvent is what causes the stabilization of certain crystallographic planes that lead to the formation of nanocubes (Figure 4). Solvents with lower dielectric constants stabilize the terminal (001) planes that are crucial for cubic morphology formation. The combination of the effect of the solvent and the concentration of the salts used in the synthesis can lead to well defined cubic particles with good size control. Increasing concentrations of the salt precursors lead to smaller particle sizes of the nanocubes [11]. The addition of a surfactant has been shown to greatly influence the growth of specific crystal facets by slowing the growth rate and stabilization of certain faces allowing for cubic particles to form [56]. The surfactant also has allowed for highly dispersed colloidal solutions by creating hydrophobic surfaces (Figure 5).

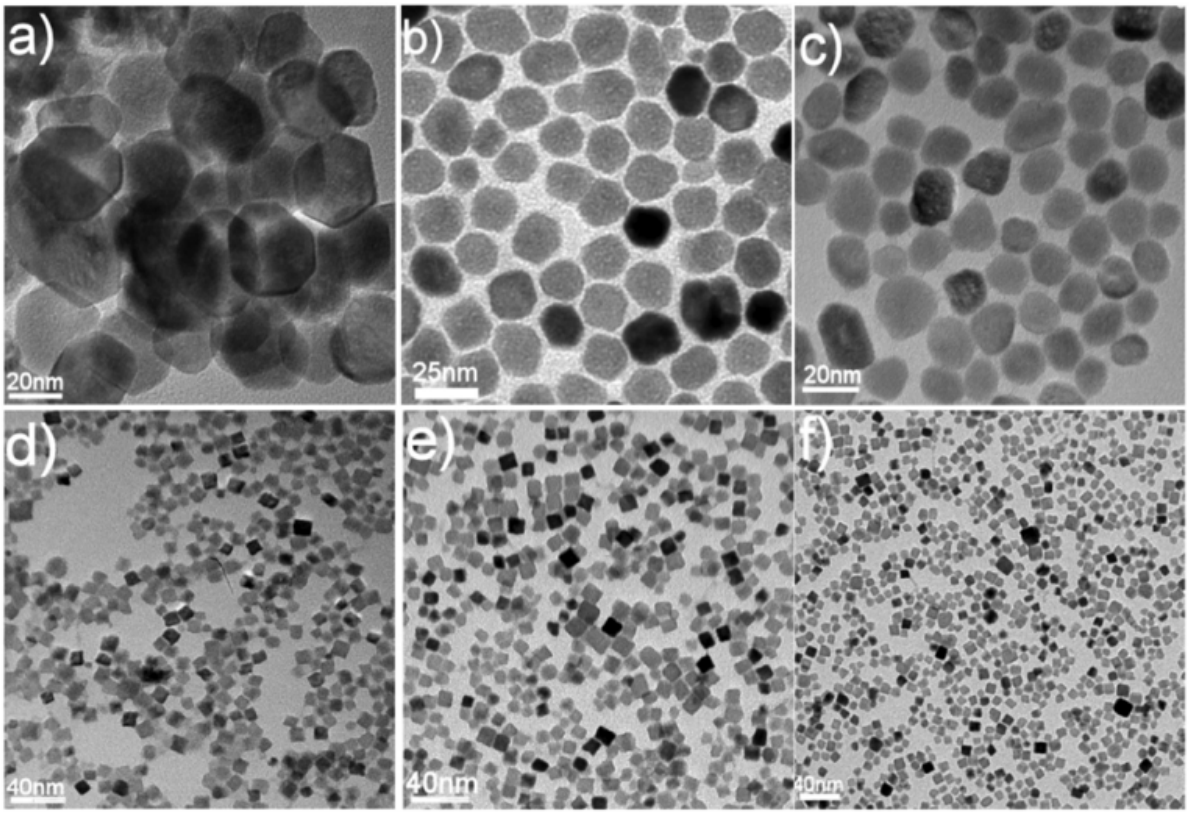

Figure 9 Effects of solvent on particle morphology of barium titanate a) benzyl alcohol, b) diethylene glycol, c) diethylene glycol monobutyl ether, d) toluene, e) phenyl ether, f) benzyl ether [11].

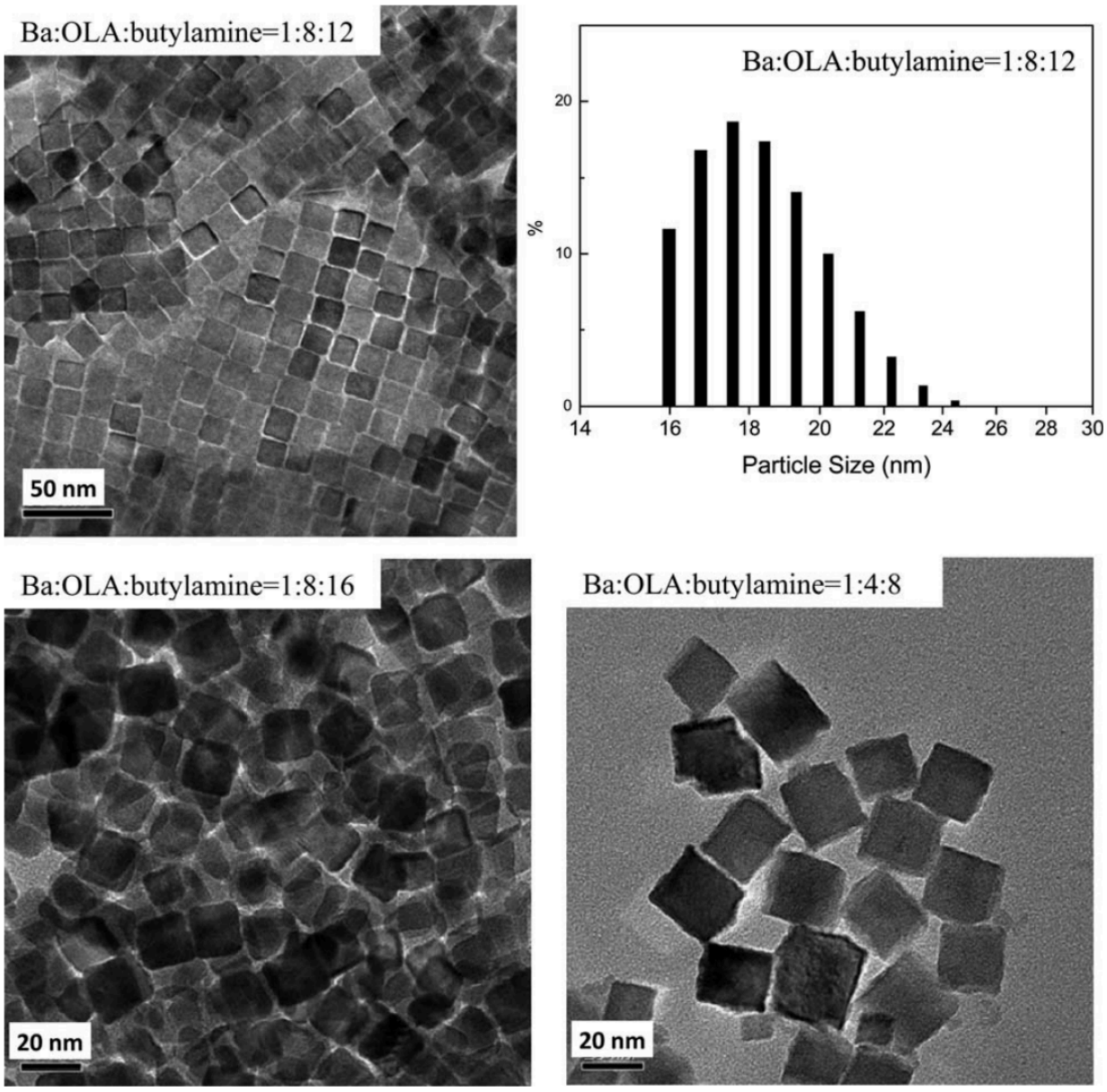

Figure 10 Highly dispersed barium titanate nanocubes synthesized with a surfactant [56]

The two main growth mechanisms in aqueous synthesis are in situ and dissolution-precipitation. The in-situ growth process involves the nucleation of nanocubes in the amorphous colloidal gel of the titanium precursor and the coalescence and aggregation of the nucleates into larger cubic particles. Within the colloidal gel there the nucleates orient themselves into

preferential directions to aggregate and reduce the high energy surfaces and the overall free energy of the system [70]. The cubic shape post nucleation was fully developed and maintained due to the control of the surfactant. The suppressed crystal growth of certain crystallographic planes allows for faster exposure of characteristic planes of the cubic structure.

The addition of a surfactant allows for absorption of onto some of these planes to slow down their growth. This exposes other planes and allows for their accelerated growth giving rise to special structures like nanocubes. Surfactants like polyethylene glycol (PEG) have a preferential absorption onto the metal ions. In $BaTiO_3$ the {110} surfaces have a higher density of metal ions, so PEG creates a protective shell on these surfaces because of the preferential absorption onto metal ions. This protective shell reduces the growth rate along these directions so other surfaces like {100} are able to grow faster giving rise to the cubic particle structure [71]. Similarly, when oleic acid is used as a surfactant, it has preferential absorption onto the planes with higher density of metal ions thus slowing down the growth of specific crystallographic planes. Although, the growth mechanism transitions from in situ to dissolution-precipitation with the addition of and additive like hydrazine or tert-butylamine.

As stated before, surfactants prefer absorption onto surfaces with higher metal ion densities. An important factor in the successful production of cubic particle morphologies is controlling the growth rate of the (100) surfaces. Slowing down the growth in these directions is crucial in producing cubic structures. The surface energies of the (100), (110), and (111) surfaces are quite similar. Hydrazine has preferential absorption on the Ti-O terminated surfaces, so it allows the surfactant like oleic acid to absorb onto the other high atom density surfaces like (100) through intercalation with Ba ions since the density of Ba ions is highest in the (100) planes. Whereas the lack of hydrazine would promote the absorption of oleic acid on the (110) surfaces

leading to an in-situ growth mechanism. The addition of hydrazine has a great effect on the morphology that forms. The combined effect of hydrazine and oleic acid also allow for high dispersity and size control of the nanocubes [18]. The lack of surfactant and additive will lead to nanocrystals with mixed facets to reduce to total surface free energy of the system.

1.5 Spinel, AB_2O_4

Spinel materials, more specifically ferrites have been of great interest because of their magnetic properties and ferromagnetic behavior. Materials like cobalt ferrite have promise in applications like photocatalysis, lithium-ion batteries, and enzymatic mimetics because of its high coercivity, moderate saturation magnetization, large magnetostrictive coefficient, and great mechanical hardness and chemical stability [72]. The development of cubic particle morphologies of these materials gives rise to enhancements in their properties and the opportunities for new applications.

Traditionally magnetic nanocubes have been obtained by thermal decomposition of the corresponding organometallic compounds, but this method is toxic and energy-consuming [72]. Although many groups still utilize this type of synthesis method to develop cubic particle morphologies [73][74][75], other synthesis methods have been explored. These types of synthesis methods include sonochemical [72], hydrothermal [76], nonhydrolytic with seed-mediated growth [6], and aqueous [77].

There are many different parameters that affect the development of cubic morphologies for spinel materials. In most synthesis methods the type of solvent used and whether it is aqueous, or alcoholic can have an effect. The type of surface modification done on the nanocubes can increase the yield of these faceted morphologies, control the particle size, and

improve the dispersibility. The addition of sodium oleate, which provides a hydrophobic surface, the deposition of CTA+ ions on specific crystal facets and capping the nanocubes with PVP have all been used as surface modification techniques to produce cubic particles shown in Figure 11 [74]. One of the biggest driving factors in the successful production of spinel nanocubes is the slow growth rate. Slowing down the growth rate and having slow heating rates allows for specific crystallographic facets to be exposed and grow to form the cubic morphology.

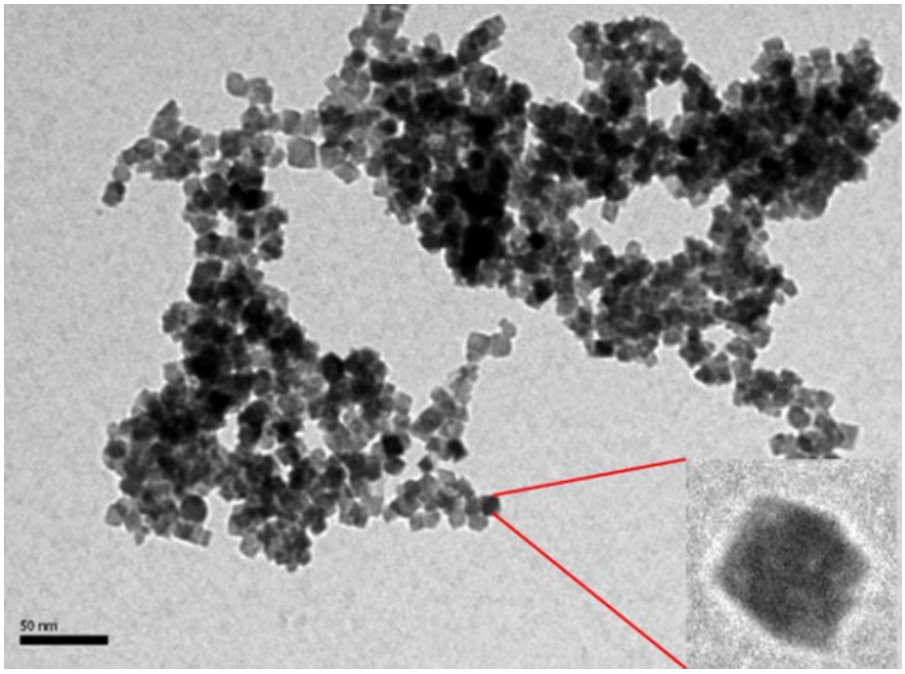

Figure 11 Transmission electron micrograph of cubic particles of MnFe [74].

For cobalt ferrite, depending on the synthesis type, there are a couple of factors that affect the morphology. The first it the Co to Fe ratio and the surfactant to metal ratio. This ratio played an important role in controlling the size of the nanocubes. The more Co precursor amount, the less available surfactant there was to regulate the growth of the particles. This caused the particles to grow bigger (Figure 12) [78]. The use of poly(N-vinyl-2-pyrrolidone) or PVP

reduced graphene oxide-FeOOH as a precursor helped in the development of cubic particles. PVP serves as a stable capping agent for cobalt ferrite. The combination of the capping agent and ethanol restrict the crystal growth of cobalt ferrite nanoparticles during the second step in the synthesis. This helps form uniform cubic nanostructures that are controlled and established [75]. The use of ethanol has been shown to have a direct effect on controlling the morphology because ethanol molecules are absorbed onto the crystal surfaces, and they limit the growth rate of the particles [72].

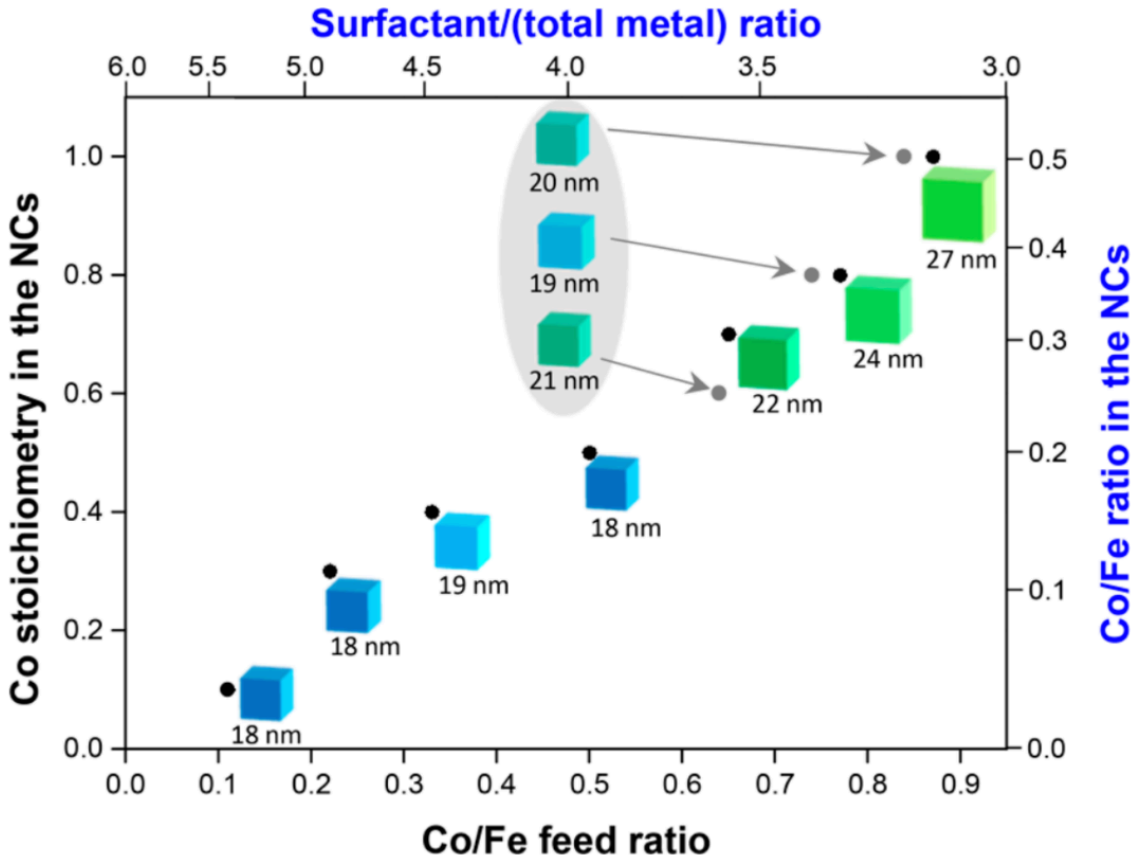

Figure 12 Plot showing the growth of cobalt ferrite nanocubes with increasing Co/Fe feed ratio and Co/Fe ratio in the nanocrystals [78].

Similarly, for manganese ferrite, the formation mechanism of the nanocubes is favored by the preferential growth of the surfactant molecules adsorption. More specifically, the use of CTA+ ions help in the directional growth of the nanocubes. In the initial stage of the reaction, the nanoparticles grow equally in all directions. After adsorption of the CTA+ ions on specific crystal facets (100), spherical nanoparticles transform into cubic by controlling the growth rates along different crystal axes. They only allow growth in the [111] directions [74]. For other materials like zinc ferrite, ethylenediamine serves as a precipitant and pH controller that influences the morphological evolution and size distribution of the nanocubes (Figure 13) [77].

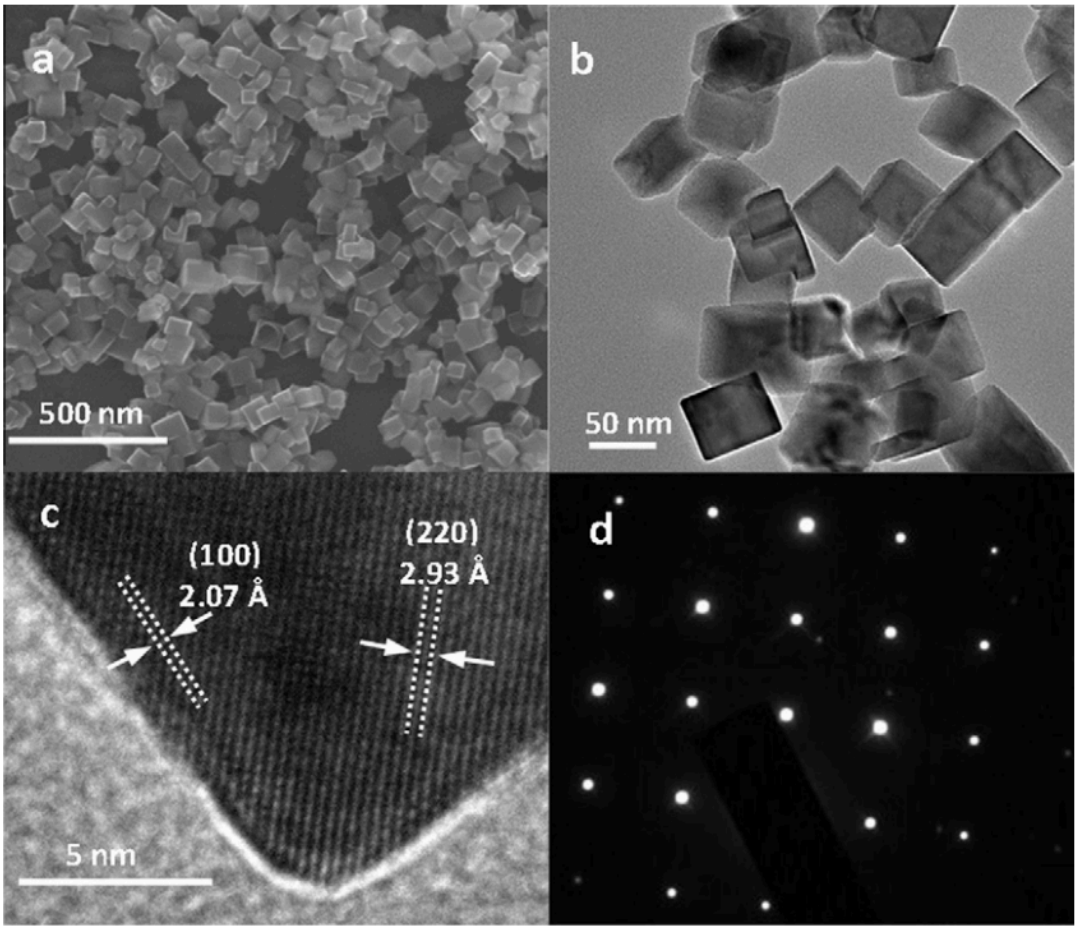

Figure 13 Scanning electron and transmission electron micrographs of $ZnFe_2O_4$ cubic particles [77].

Compared to the hydrothermal synthesis methods of the perovskite materials, the development of cobalt oxide nanocubes depends on several factors like hydrothermal time, temperature, type of surfactant, concentration, and the molar ratios of the starting materials. In addition, these parameters can also affect the overall size and shape of the particles. In general, large quantitates of nanocubes with good uniformity were achieved with the surfactant SDS and at a synthesis temperature of 140°C for 12 hours.

1.6 A_3O_4

Iron and cobalt oxide (Fe_3O_4 & Co_3O_4) exhibit superior magnetic, optical, and transport properties. These properties make these materials great for applications like catalysis, pigments, electrochemistry information storage, sensors, and biomedicine [4][79]. The development of anisotropic structures of iron oxide has been shown to give rise to enhanced properties and new applications like bio targeting and magnetic resonance imaging [4].

Generally, these materials have been developed using solvothermal/hydrothermal, nitrate-salt-mediated, coprecipitation, and thermal decomposition methods [80] [79] [81][82]. Depending on the synthesis, there are many factors that affect the shape and size of the nanoparticles. The reaction temperature and time are especially important for the nitrate-salt-mediated method [79]. Similarly, the reaction temperature and time play an important role in the solvothermal synthesis process. The concentration and the molar ratio of reactants and surfactant affect the size and shape of the resulting particles shown in Figure 14 [83]. Some solvothermal synthesis procedures include the addition of β-amyrin, where the absence or presence of this can dictate the final particle morphology. Synthesis techniques that are less commonly used

include a modified polyol process in organic phase, where the heating rate and reflux time have a large effect on the resulting nanoparticles [5].

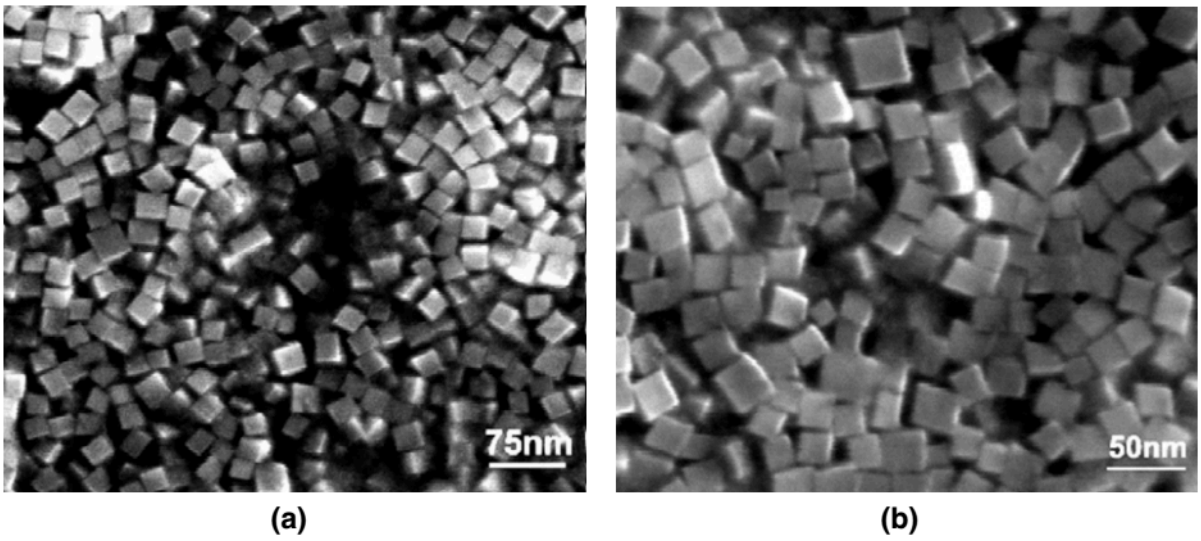

Figure 14 Scanning electron images of Co_3O_4 cubic particles synthesized with SDS as a surfactant [83].

More specifically, parameters that directly influence the morphology are a chemically stable environment, the ratio of the surfactant like oleic acid to iron, reaction time, reaction temperature, pH of solution, concentration, the precursors used, and the addition of a surfactant. The balance of chemical potential of monomers and the chemical potential of different crystals is crucial in developing the cubic morphology of these materials. For iron oxide, with increasing temperature iron acetylacetonate exchanges iron cations with the oleate anions to form monomers [84]. The monomers accumulate and reach oversaturation. Once oversaturation is reached, nuclei are generated. When the chemical potential of monomers is higher than those of the crystal planes, they can change from a high chemical potential state to any of the planes of lower chemical potential. The rate at which monomers are deposited varies for every facet and depends on the kinetic constants. The {111} planes are the most densely packed and have a high

steric hinderance so the arrival of new monomers will be inhibited. The energy barrier that monomers have to overcome to deposit on this plane is higher than other planes so the {111} planes will grow the slowest. Once the chemical potential of the monomer decays enough, deposition on the {110} planes stop and continues on the {111} facets thus leading to the cubic particle morphology formation (Figure 15).

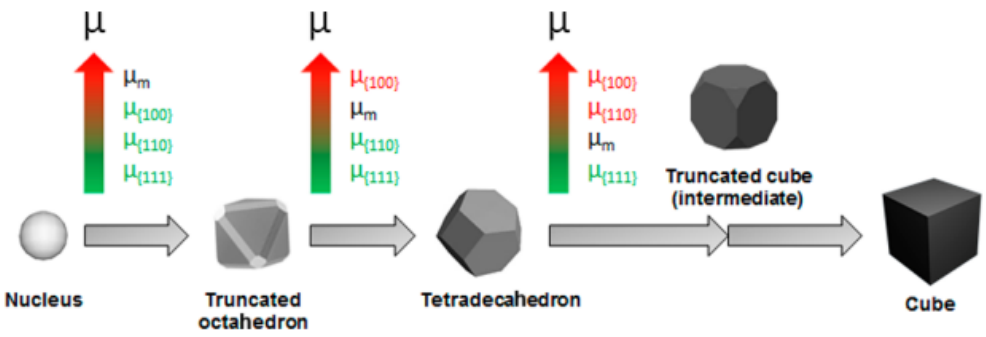

Figure 15 Transition of a nucleus of Fe_3O_4 to a cubic particle [4].

1.7 Conclusions

With guidance from this past literature, this project explored the two different synthesis methods in efforts of producing dispersed cubic nanoparticles of barium titanate and strontium titanate with roughly uniform particle size. The two synthesis methods adapted are the molten hydrothermal synthesis and the aqueous hydrothermal synthesis.

Acknowledgements

Chapter 1, in part is currently being prepared for submission for publication of the material. Sanchez, Maritza; Barraza, Paul; Zhou, Jin; and Graeve, Olivia, A. The dissertation author was the primary author of this chapter.

Chapter 2 Comparative analysis of molten hydrothermal and aqueous hydrothermal synthesis methods of barium titanate and strontium titanate for faceted particle formation

Abstract

Perovskite materials, specifically barium titanate (BT) and strontium titanate (ST), hold significant potential for a range of applications, including ferroelectric devices and multilayer capacitors. The particle morphology of these materials can significantly influence their electronic properties, such as their dielectric constant and ferroelectric behavior. This study aims to understand the formation mechanisms of faceted particles of BT and ST, synthesized using both molten hydrothermal and aqueous hydrothermal methods. Our experimental results obtained through scanning electron microscopy (SEM) reveal successful development of faceted particles for BT using the molten hydrothermal method and for ST using the aqueous hydrothermal method. However, X-ray diffraction results indicate the presence of unreacted $SrCO_3$ and an amorphous structure in the ST sample synthesized by the molten hydrothermal method, pointing towards an in-situ growth mechanism of ST. Transmission electron microscopy (TEM) results suggest that the formation of faceted particles occurs through the aggregation of smaller crystallites in identical crystallographic directions. This research provides valuable insights into the particle morphology control of perovskite materials through different synthesis methods, shedding light on their potential in advanced electronic applications.

2.1 Introduction

Perovskite materials like barium titanate ($BaTiO_3$) and strontium titanate ($SrTiO_3$) have been of great interest for applications as ferroelectrics, multilayer capacitors, thermistors, transducers and infrared detectors [56][57][58]. Controlling the particle morphology of these materials has

opened new opportunities for increased dielectric and ferreoelectric properties. Previous studies have shown that thin films of sintered ordered arrangements of barium titanate nanocubes exhibit a high dielectric constant of >4000 because of misorientation between neighboring nanocubes that give rise to misfit strain that enhances the dielectric properties [16][17]. Other studies have also shown that the high charge polarization on the surface of the barium titanate nanocubes has led to increased reversibility in the dielectric polarization and low hysteresis loss [69]. The results obtained from studies begin to expose the potential in tailoring material properties through morphology control on particles and the need to explore methods to produce them.

Faceted particles have been previously synthesized through a number of methods including molten salt [59][60], microwave-assisted [61], composite-hydroxide [62][63][64][65], solvothermal [66], and aqueous surfactant-assisted [56][12][57][67][13][16][14][68][69]. Depending on the synthesis, there are several parameters such as the addition of salts, hydroxides, additives, or surfactants that have a strong effect on the type of particle morphology that forms for perovskite materials. The composite-hydroxide-mediated method includes the addition of hydroxides to facilitate the nucleation of barium titanate from the precursor materials. Nucleates begin to aggregate and form larger particles to reduce the overall energy of the system. These aggregates can then form cubic particle morphologies through a surface reconstruction [62]. The low melting point of the hydroxides (NaOH, 318°C and KOH, 360°C [85]) also allows for reduced synthesis temperatures to produce barium titanate [63], but low synthesis temperatures also means that an ample amount of time is needed for the reaction to occur and to begin to grow the crystal facets [60]. Shorter synthesis times do not allow for crystals to grow into well-defined faceted particles.

Similarly for the molten salt synthesis of barium titanate the addition of salts affects the final particle morphology. The salts in combination with barium oxide (BaO) and rod-shaped titanium dioxide (TiO_2) as the starting precursors permit the formation of cubic particles of barium titanate to form as a result of the slower dissolution rate of BaO than TiO_2 in the salts [59]. The slower dissolution rate allows for the breakdown of TiO_2 rods to occur before the BaO is dissolved in the molten salts and begins to form a BT shell on the TiO_2 cubes [59]. The two synthesis methods have shown that hydroxides/salts, the starting Ba and Ti precursors and the reaction time all have an effect on the final particle morphology of BT.

Furthermore, for aqueous synthesis methods there are other parameters that play a role in the formation of faceted morphologies of perovskite materials; this includes type of solvent used, pH of solution, and the addition of surfactants [56][58][86][11][87]. Specifically, solvents like hexane, toluene, 1-butanol, 1-decanol, phenyl ether, and benzyl ether have been used to synthesize cubic particles [11]. The polarity of the solvent is what causes the stabilization of certain crystallographic planes that lead to the formation of faceted particles [11]. In particular, solvents with lower dielectric constants (~2-4) like phenyl ether, benzyl ethel or toluene stabilize the terminal (001) planes that are crucial for cubic morphology formation [11]. Decreasing the surface energy of certain crystallographic planes allows for the growth of other planes to occur changing the final morphology of the particle [88]. This has been observed for the oleic acid surfactant-assisted synthesis of barium titanate and strontium titanate, where the oleic acid has preferential absorption on the (100) crystal plane which leads to the stabilization of the (100) face [87]. The stabilization of the (100) crystal plane allows other crystal faces like the (111) and (110) faces to grow.

Keeping the formation mechanisms that have been proposed previously, aims at identifying the differences in faceted particle formation between barium titanate and strontium titanate. A comparison between the molten hydrothermal and the aqueous hydrothermal synthesis methods for both barium titanate (BT) and strontium titanate (ST) to produce faceted particles is analyzed. The two methods were used to identify the ideal synthesis environment and parameters to produce cubic particle morphologies of each of the materials. The formation mechanism of the observed faceted particle structures is also proposed for barium titanate and strontium titanate.

2.2 Experimental Methods

Two synthesis methods were used to produce barium titanate and strontium titanate in efforts in controlling their particle morphology. A molten hydrothermal and aqueous hydrothermal methods were used as to compare the successful development and particle morphology of BT and ST. Preliminary experiments were also conducted using the molten hydrothermal method to determine the ideal synthesis parameters that resulted in the highest yield of BT nanocubes.

For the preliminary BT molten hydrothermal experiments, $BaCO_3$ (99+%, A.C.S Reagent, Sigma-Aldrich) and titanium dioxide, TiO_2 (99.9%, anatase, SkySpring Nanomaterials) were used as the starting materials at a concentration of 0.5 mmol. Sodium hydroxide, NaOH (pellets, anhy, Sigma-Aldrich) and potassium hydroxide, KOH (Sigma-Adrich) were placed in a 25mL Teflon-lined autoclave reactor in a 51.5:48.5 Na/K ratio. $BaCO_3$ and TiO_2 were added into the Teflon-lined autoclave reactor. The Teflon-lined autoclave reactor was sealed and placed in a box furnace at a range of temperatures and times, provided in **Error! Reference source not f ound.**.

For the molten hydrothermal method of producing barium carbonate, $BaCO_3$ (99+%, A.C.S Reagent, Sigma-Aldrich) and titanium dioxide, TiO_2 (99.9%, anatase, SkySpring Nanomaterials)

were used as the starting materials at a concentration of 0.5 mmol. Sodium hydroxide, NaOH (pellets, anhy, Sigma-Aldrich) and potassium hydroxide, KOH (Sigma-Adrich) were placed in a 25mL Teflon-lined autoclave reactor in a 51.5:48.5 Na/K ratio. $BaCO_3$ and TiO_2 were added into the Teflon-lined autoclave reactor. The Teflon-lined autoclave reactor was sealed and placed in a box furnace at a range of temperatures and times, provided in **Error! Reference source not f ound.**. Similarly for the molten hydrothermal synthesis of strontium titanate, strontium carbonate, $SrCO_3$ (>=99.9% metals bas, Sigma-Aldrich) and titanium dioxide, TiO_2 (99.9%, anatase, SkySpring Nanomaterials) were used as the starting materials at a concentration of 0.5 mmol. NaOH and KOH (mentioned above) were placed in a 25mL Teflon-lined autoclave reactor in a 51.5/48.5 Na/K ratio. $SrCO_3$ and TiO_2 were added into the Teflon-lined autoclave reactor. The reactor was sealed and placed in a box furnace at the temperatures and times outlined in **Error! Reference source not found.**.

For the aqueous hydrothermal method of producing barium nitrate, $Ba(NO_3)_2$ (99+%, A.C.S. Reagent, Sigma-Aldrich) and titanium dioxide, TiO_2 (99.9%, anatase, SkySpring Nanomaterials) were used as the starting materials with a molar ratio of Ti/Ba = 1:1. $Ba(NO_3)_2$ was added into 25mL of distilled water and magnetically stirred for 10 minutes. Once the $Ba(NO_3)_2$ was dissolved, 5g of sodium hydroxide, NaOH (pellets, anhy, Sigma-Aldrich) was added into the solution. After 5 minutes of stirring, TiO_2 was added to the solution to form a white liquid. The solution was equally split into two 25mL Teflon-lined autoclave reactors. The reactors were sealed and placed in a box furnace at a range of different temperatures and times, presented in **Error! Reference source not found.**. Similarly, strontium nitrate, $Sr(NO_3)_2$ (99+%, A.C.S. R eagent, Sigma-Aldrich) and titanium dioxide, TiO_2 (99.9%, anatase, SkySpring Nanomaterials) were used as the starting materials for the aqueous hydrothermal synthesis of ST, with a molar

ratio of Ti/Sr = 1:1. $Sr(NO_3)_2$ was added into 25mL of distilled water and magnetically stirred for 10 minutes. Once the $Sr(NO_3)_2$ was dissolved, 5g of NaOH was added into the solution. After 5 minutes of stirring, TiO_2 was added to the solution to form a white liquid. The solution was equally split into two 25mL Teflon-lined autoclave reactors. The reactors were sealed and placed in a box furnace at a the temperatures and times outlined in **Error! Reference source not found.**.

Table 1 Times and temperatures used for preliminary molten hydrothermal synthesis experiments of barium titanate, and the comparative studies of the molten hydrothermal and aqueous hydrothermal synthesis experiments of barium titanate and strontium titanate.

Preliminary Molten Hydrothermal Synthesis		Molten Hydrothermal Synthesis		Aqueous Hydrothermal Synthesis	
Time (hrs)	Temperature (°C)	Time (hrs)	Temperature (°C)	Time (hrs)	Temperature(°C)
24	220	12	180	12	180
36	220	12	200	12	200
48	220	12	220	12	220
60	220	18	180	18	180
		18	200	18	200
		18	220	18	220
		24	180	24	180
		24	200	24	200
		24	220	24	220

After the synthesis all the samples were washed three times via centrifugation. The samples were first washed once in a diluted acetic acid solution at 10,000 rpm for 10 min, followed by two washes in ethanol at 10,000 rpm for 10 min. The samples were then dried in a box furnace at 60°C for 12 hrs and prepared for characterization. The phase purity of the powders was analyzed through X-ray diffraction (XRD) on a D2 Phaser (Bruker AXS, Inc., Madison, WI) using CuKα radiation. The count time was 0.3 sec with a step size of 0.014° 2θ from 20 to 90° 2θ. Particle morphologies were imaged using scanning electron microscopy (SEM) on a Quanta 250 FEG

(FEI, Hillsboro, Oregon) at an accelerating voltage of 5 kV. To prevent charging, the samples were coated with iridium for 8 sec. Particle morphology and size, as well as electron diffraction patterns, were analyzed by transmission electron microscopy (TEM) on a Talos F200X G2 S/TEM (Thermofisher, Waltham, MA) with an operating voltage of 200 kV. The sample preparation for TEM consisted of ~0.5 mg of BT or ST powder dispersed in 300 mL of isopropanol alcohol (IPA). Three drops of this suspension were subsequently dispersed in 25 mL of IPA and ultrasonicated for 25 min. One drop of the 25 mL suspension was deposited onto a 200-mesh carbon-coated copper grid. The grid was placed in a vacuum furnace at 75°C to completely evaporate the solvent.

2.3 Results and Discussion

2.3.1 X-ray diffraction

The XRD patterns of BT synthesized via the molten hydrothermal method are provided in Figure 16. All the synthesis temperatures and times (**Error! Reference source not found.**) showed the successful production of cubic BT with space group *Pm3m* (PDF 01-070-9165). All diffraction peaks were sharp and clearly defined. This indicated high crystallinity of the material. There was no evidence of peak broadening indicating no large changes in the crystallite size of the samples synthesized at different times and temperatures. Crystallite sizes calculated by the Scherrer equation of BT samples (Table 2) also showed relatively uniform crystallite sizes for the samples synthesized via the molten hydrothermal method. The average crystallite size was 23.61 nm and a standard deviation of 3.67 nm. Based on the XRD results, BT with high purity and crystallinity can be successfully synthesized by the molten hydrothermal method.

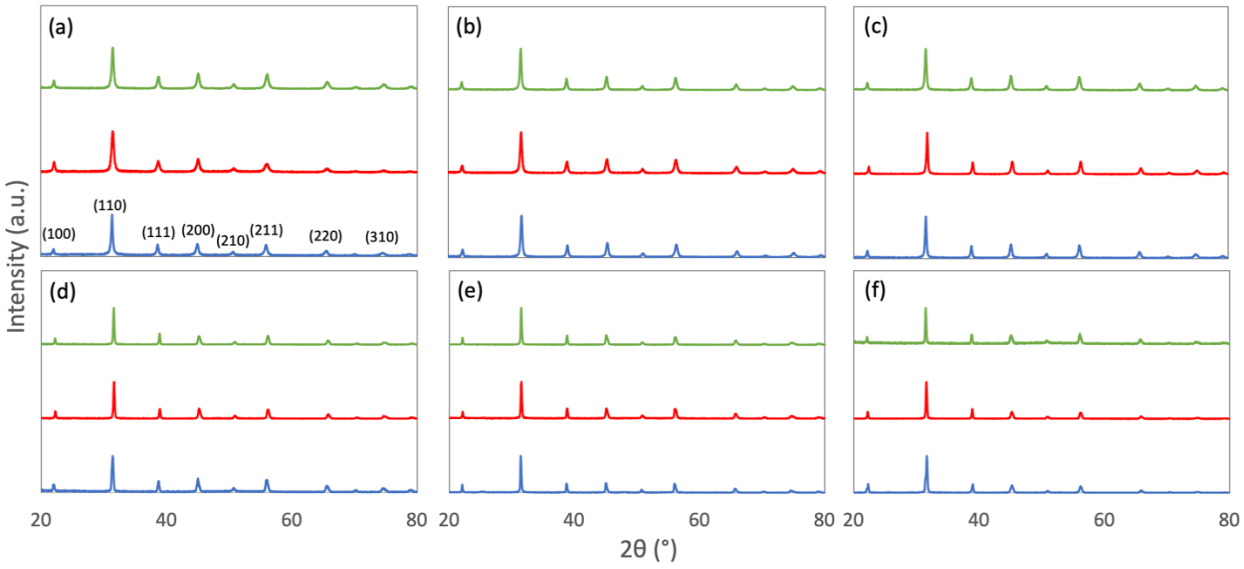

Figure 16 X-ray diffraction patterns of barium titanate samples synthesized via the molten hydrothermal method at (a) 180C, (b) 200C, (c) 220C and for 12 hours (blue curve), 18 hours (red curve), and 24 hours (green curve). X-ray diffraction of barium titanate samples synthesized via the aqueous hydrothermal method at (d) 180C, (e) 200C, (f) 220C and for 12 hours (blue curve), 18 hours (red curve), and 24 hours (green curve). All synthesis temperatures and times show the successful development of cubic barium titanate, Pm3m (PDF 01-070-9165).

Table 2 Calculated crystallite sizes from X-ray diffraction of barium titanate samples synthesized by the molten hydrothermal and the aqueous hydrothermal synthesis methods at various synthesis times and temperatures.

		Molten Hydrothermal	**Aqueous Hydrothermal**
Synthesis Temperature (°C)	**Synthesis Time (hr)**	**Crystallite Size (nm)**	**Crystallite Size (nm)**
180	12	23.05	27.21
180	18	16.74	36.93
180	24	20.13	38.52
200	12	23.91	42.40
200	18	22.05	38.49
200	24	25.80	40.47
220	12	27.72	28.53
220	18	28.36	39.95
220	24	24.75	39.87

The XRD patterns of ST synthesized via the molten hydrothermal method are provided in Figure 17. All synthesis temperatures and times showed the presence of cubic ST with space group *Pm3m* (PDF 01-070-8508). The sample synthesized at 180°C for 18 hours also showed a

small presence of orthorhombic strontium carbonate ($SrCO_3$, PDF 00-005-0418) at $2\theta \sim 25°$ (Figure 17(a)). The formation of the $SrCO_3$ secondary phase has been seen previously by other groups [61][89][90][91][92][65]. The presence of $SrCO_3$ in the synthesis of $SrTiO_3$ are likely due to an incomplete reaction or traces of the CO_3^{2-} ion in barium or alkalis [91]. The presence of $SrCO_3$ in this study is likely due to an incomplete reaction at this low temperature and time because this phase was not observed at higher temperatures and times (see Figure 17(b), 17(c)). In addition, the samples synthesized at 180°C for 18 and 24 hours and 200°C for 12 and 18 hours had much broader peaks than the sample synthesized at 220°C, evident in the (110) peak (see Figure 17(a), 2(b)). The broadening of the XRD peaks likely indicated smaller crystallite sizes of the sample. Given the presence of $SrCO_3$ in the sample synthesized at 180°C for 18 hours, likely due to an incomplete reaction it can be concluded that crystallites begin to form at 180°C and need further time or higher temperatures to continue growing. The samples synthesized at 220°C showed the narrowest peaks indicating higher crystallinity at the higher synthesis temperature (see Figure 17(c)). Calculations of the crystallite size from the Scherrer equation revealed that the smallest crystallite sizes were for the samples with the broader XRD peaks, synthesized at 180°C for 18 and 24 hours and 200°C for 12 and 18 hours. These samples had calculated crystallite size between 3-5 nm.

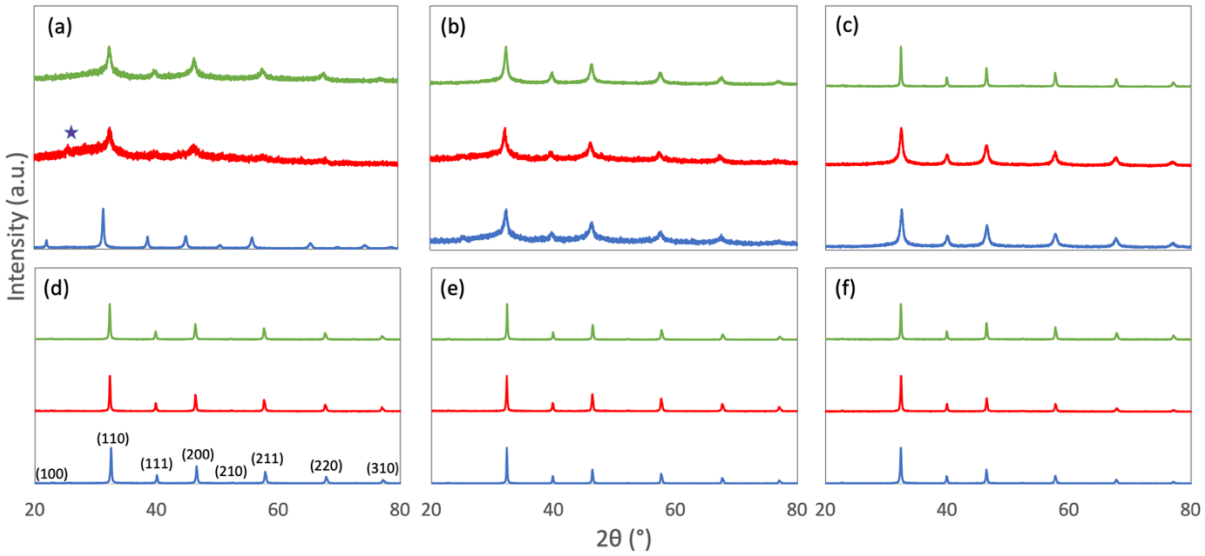

Figure 17 X-ray diffraction of strontium titanate samples synthesized via the molten hydrothermal method at A) 180C, B) 200C, C) 220C and for 12 hours (blue curve), 18 hours (red curve), and 24 hours (green curve). X-ray diffraction of strontium titanate samples synthesized via the aqueous hydrothermal method at A) 180C, B) 200C, C) 220C and for 12 hours (blue curve), 18 hours (red curve), and 24 hours (green curve). All synthesis temperatures and times show the successful development of cubic strontium titanate, Pm3m (PDF 01-070-8508). The sample synthesized at 180C for 18 hours (blue curve in (a)) also shows the presence of orthorhombic strontium carbonate (PDF 00-005-0418) at about 25° 2θ represented by the purple star.

The XRD patterns of BT synthesized via the aqueous hydrothermal method are provided in Figure 16. All the synthesis temperatures and times showed the successful production of cubic BT (PDF 01-070-9165). XRD showed sharp well-defined peaks at all synthesis temperatures and times, indicating the high crystallinity of the samples. Crystallite sizes calculated by the Scherrer equation of BT samples (Table 2) also showed relatively uniform crystallite sizes for the samples synthesized via the molten hydrothermal method. The average crystallite size was 36.93 nm and a standard deviation of 5.36 nm. Based on the XRD results, both the molten and aqueous hydrothermal methods successfully produce BT with high crystallinity and no secondary phases.

The XRD patterns of ST synthesized via the aqueous hydrothermal method are provided in Figure 17. All the synthesis temperatures and times showed the successful production of cubic ST (PDF 01-070-8508). XRD showed sharp-well defined peaks at all synthesis temperatures and times, indicating the high crystallinity of the samples. The average crystallite size calculated by the Scherrer equation was 37.51 nm and a standard deviation of 3.36 nm.

Overall, the XRD results showed the successful production of the BT and ST compositions with both the molten hydrothermal and aqueous hydrothermal synthesis methods. The aqueous hydrothermal synthesis of ST showed the slight presence of $SrCO_3$ at the lower synthesis temperatures and times. Following X-ray diffraction, scanning electron microscopy was used to observe the particle morphologies of all the samples.

2.3.2 Scanning electron microscopy

The scanning electron micrographs of the preliminary molten hydrothermal experiments showed the development of faceted particles at all synthesis temperatures and times (Figure 18 (a)-(d)). Larger cubic and rod-like particle structures were observed with increasing synthesis time. The sample synthesized at 220°C for 24 hours showed the greatest uniformity in particle morphology and size (Figure 18(a)) compared to the longer synthesis times. These experiments and previous work on aqueous synthesis of ST helped identify the maximum synthesis time and temperature as 24 hours and 220°C, respectively, to prevent the formation of rod-like structures and to keep the greatest uniformity in particle morphology and size [60][86].

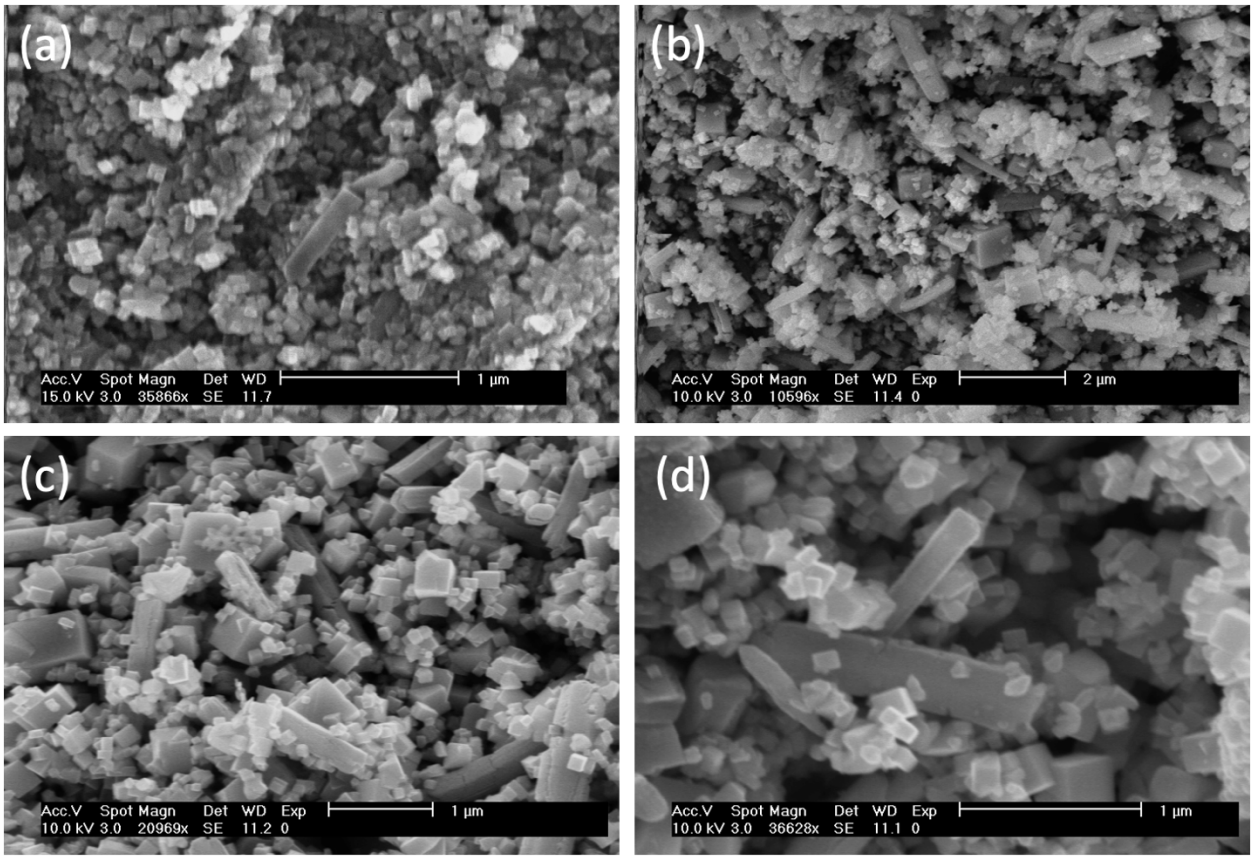

Figure 18 Scanning electron micrographs showing BT samples synthesized for A) 24 hours, B) 36 hours, C) 48 hours, D) 60 hours at 220°C, and E) transmission electron micrograph of . The samples synthesized for 24 hours showed higher homogeneity in particle size and morphology. Longer synthesis times produced more rod-like particle structures.

The SEM micrographs of the BT samples synthesized by the molten hydrothermal method are shown in Figure 19. Figure 19(a)-(b) and Figure 19(d)-(e) did not show the formation of clear faceted particles. As the temperature increased to 220°C (Figure 19(g)-(i)), the presence of faceted particles was observed. This was most apparent in the sample synthesized at the highest temperature (220°C) and time (24hrs) (Figure 19(i)). All samples synthesized at 220°C showed the successful production of cubic particles (Figure 19(g)-(i)), while the samples synthesized for 24 hours at temperatures lower than 220°C displayed a lower yield of faceted particles. The results of the SEM micrographs suggest that 220°C is a critical temperature to

produce uniform, faceted particles and synthesis temperatures below 220°C may require longer synthesis times to allow the facets of the particles to form.

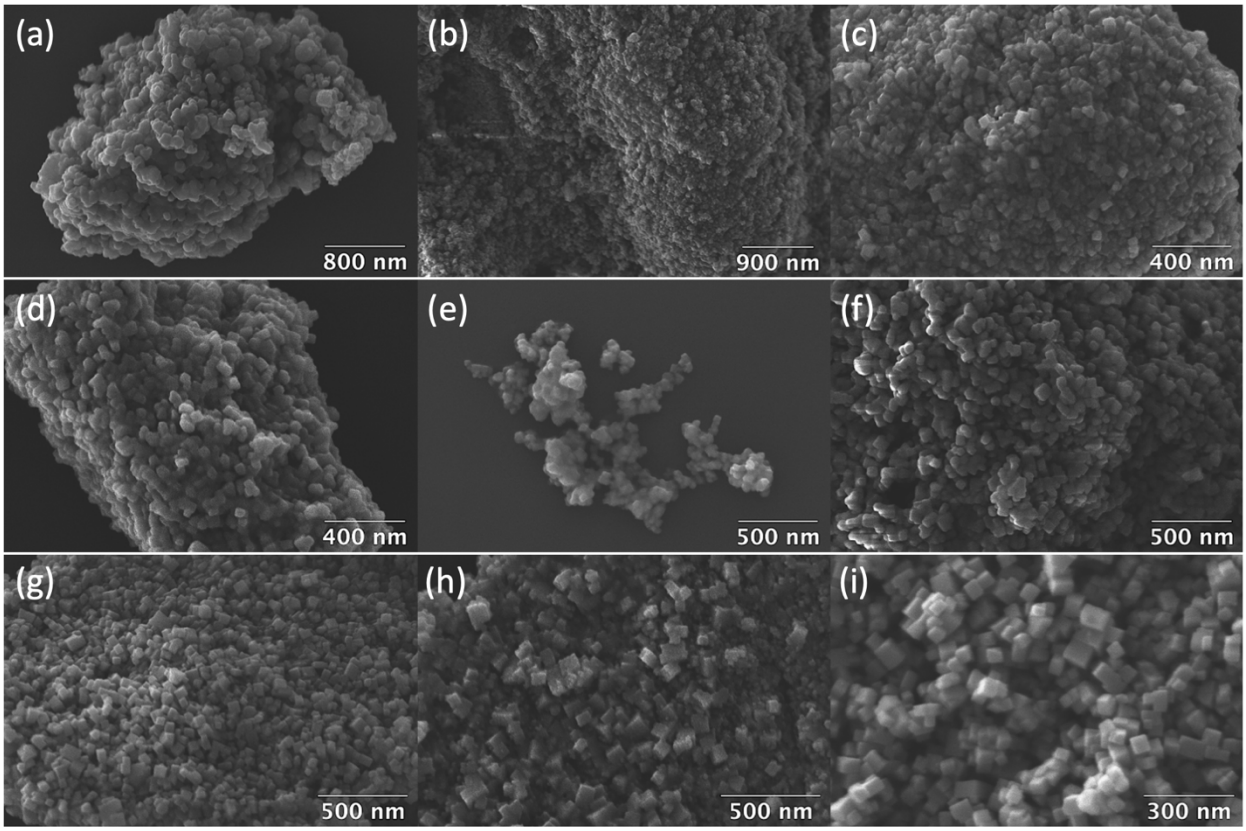

Figure 19 Scanning electron micrographs showing particle morphology of BT synthesized by the molten hydrothermal method. A) 180C - 12 hrs, B) 180C - 18 hrs, C) 180C - 24 hrs, D) 200C - 12 hrs, E) 200C - 18 hrs, F) 200C - 24 hrs, G) 220C - 12 hrs, H) 220C - 18 hrs, I) 220C - 24 hrs

SEM micrographs of ST samples synthesized by the molten hydrothermal method did not show the successful production of cubic particle morphologies (Figure 20). At synthesis temperature 180°C, the 12- and 18-hour synthesis times displayed random morphologies (see Figure 20(a)-(b)). The samples synthesized at higher temperatures and times showed longer particle structures with non-smooth surfaces (Figure 20(c)-(i)). The ridges along the length of the rod-like particles suggest the aggregation of the smaller particles along the same direction with

increasing temperature and time. These results indicate that the molten hydrothermal synthesis method was only successful in producing faceted particles with the right composition for barium titanate and was unsuccessful in producing faceted particles of strontium titanate.

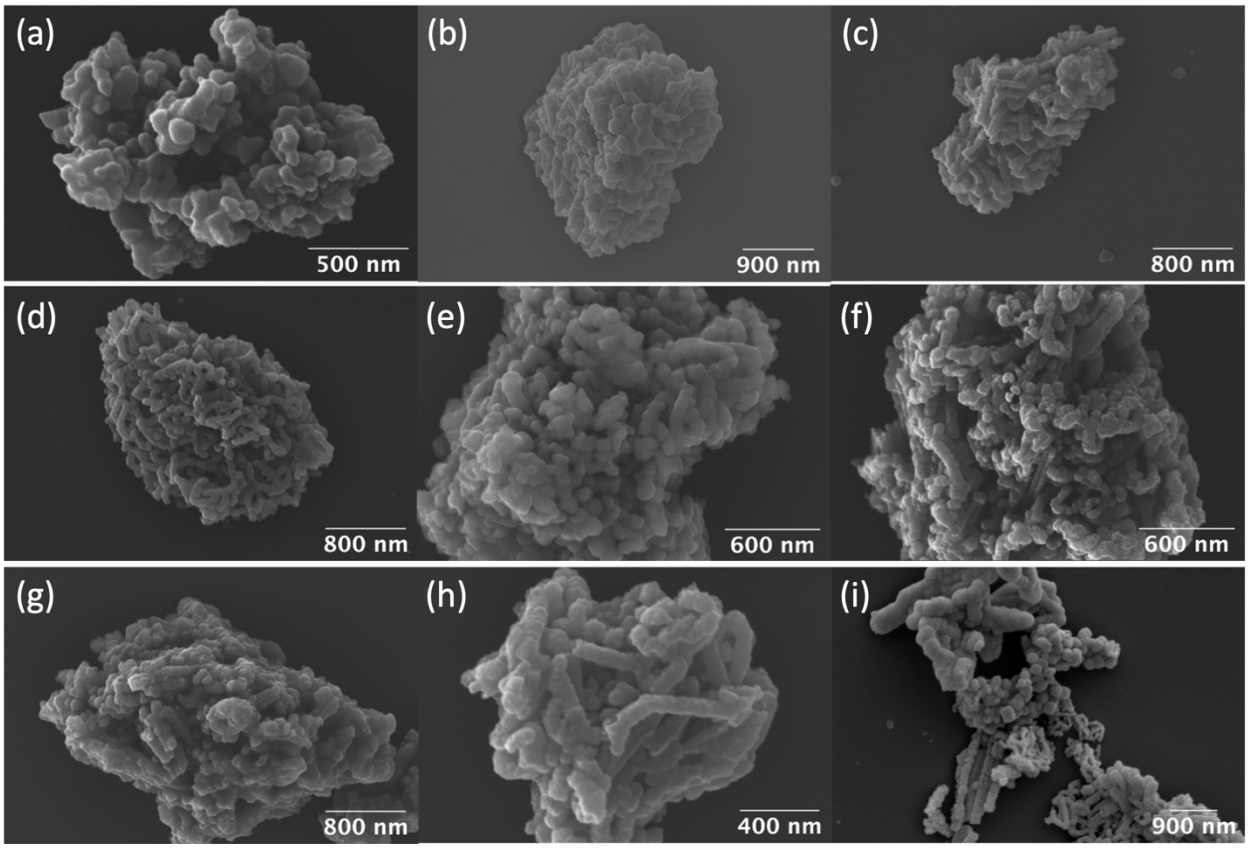

Figure 20 Scanning electron micrographs showing particle morphology of ST synthesized by the molten hydrothermal method. A) 180C - 12 hrs, B) 180C - 18 hrs, C) 180C - 24 hrs, D) 200C - 12 hrs, E) 200C - 18 hrs, F) 200C - 24 hrs, G) 220C - 12 hrs, H) 220C - 18 hrs, I) 220C - 24 hrs

The SEM micrographs of BT synthesized by the aqueous hydrothermal method are shown in Figure 21. All the samples portrayed random particle morphologies. There was no evidence of faceted particle morphologies at any of the synthesis times and temperatures. The particles were highly agglomerated and smaller in size, therefore is was concluded that unlike the molten hydrothermal synthesis this method was not successful in developing faceted particles of BT.

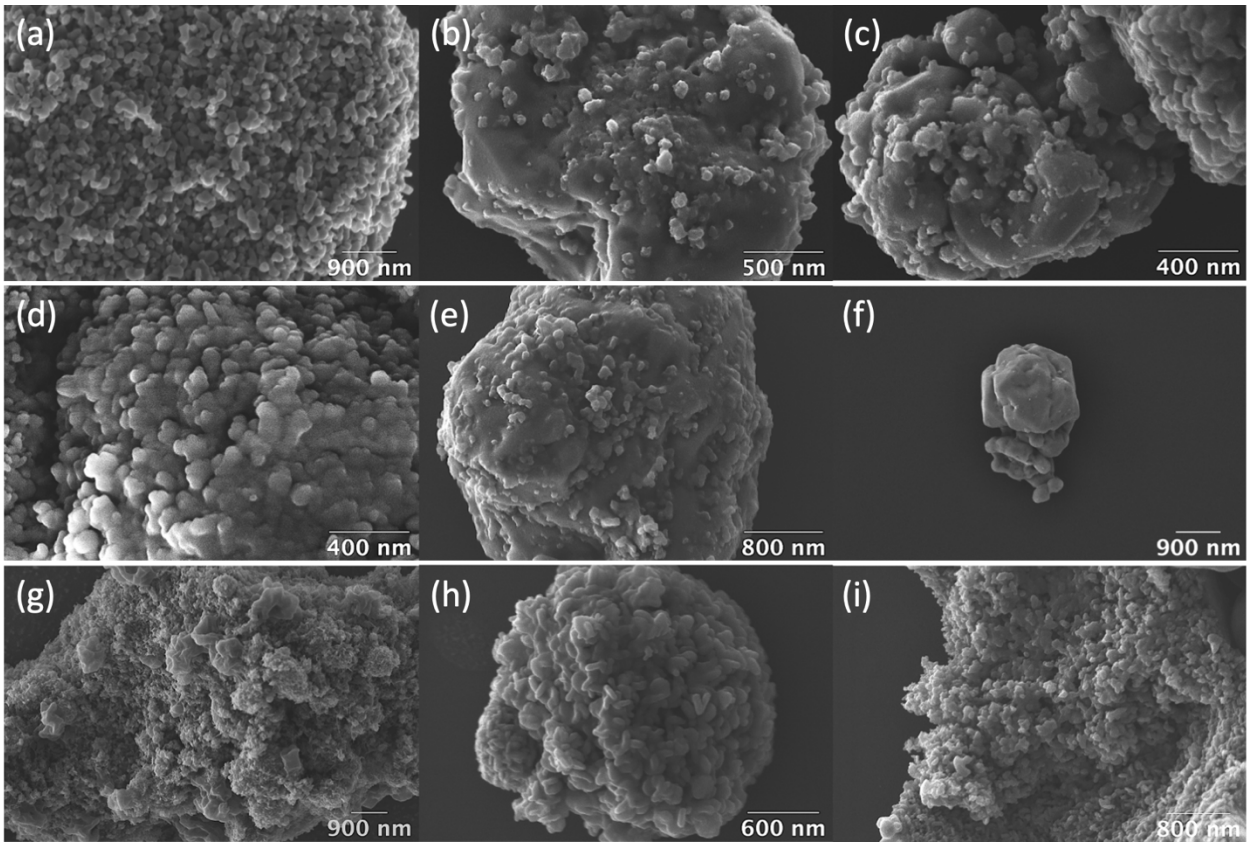

Figure 21 Scanning electron micrographs showing particle morphology of BT synthesized by the aqueous hydrothermal method. A) 180C - 12 hrs, B) 180C - 18 hrs, C) 180C - 24 hrs, D) 200C - 12 hrs, E) 200C - 18 hrs, F) 200C - 24 hrs, G) 220C - 12 hrs, H) 220C - 18 hrs, I) 220C - 24 hrs

The SEM micrographs for the ST samples synthesized by the aqueous hydrothermal method are shown in Figure 22. The samples at all synthesis temperatures and times show the development of faceted particles. The samples synthesized at 180°C displayed a combination of smaller non-faceted particles and larger faceted particles. This suggests that longer reaction times and higher synthesis temperatures are needed to allow the faceted particles to fully form. The sample synthesized at 200°C for 24 hours showed the greatest uniformity in particle size and morphology (Figure 22(f)) with particle sizes of about 60-80 nm. The SEM micrographs showed that the aqueous hydrothermal synthesis method was only successful in producing the right composition of faceted particles of strontium titanate. The difference in starting precursor,

$BaCO_3$ vs. $Ba(NO_3)_2$, as well as the starting environment plays a role in the final particle morphology of BT. The starting precursors in the aqueous hydrothermal method were barium and strontium nitrate. Differences in solubility in water between the two, where the solubility of barium nitrate at room temperature is 10.3 g/100 g water and the solubility of strontium nitrate is 80.2 g/100 g water [93], can potentially change the reactivity of the mixture. The lower solubility of BT would cause the Ba to be consumed much faster into solution than the strontium. The lack of faceted particles in the BT samples may suggest that the Ba is consumed much quicker than the time needed for the reaction to happen and for the faceted particles to form.

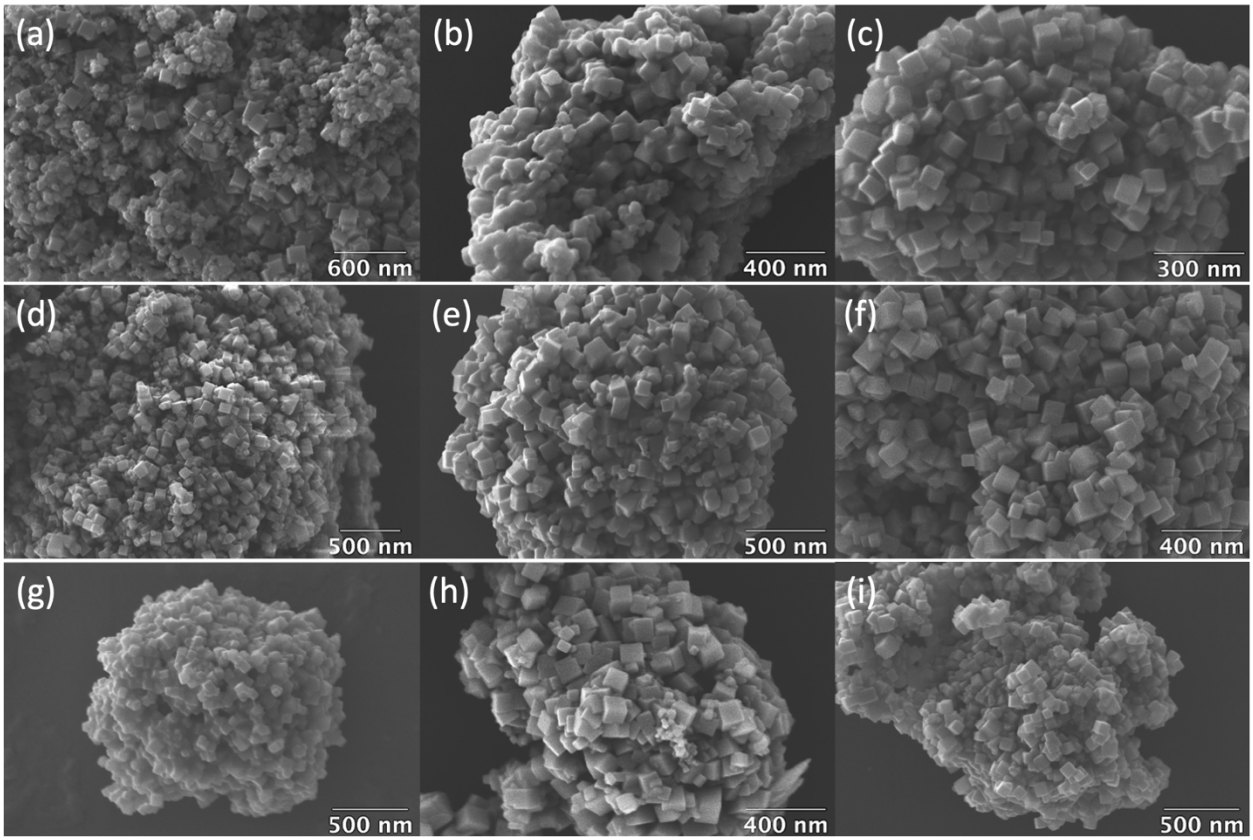

Figure 22 Scanning electron micrographs showing particle morphology of ST synthesized by the aqueous hydrothermal method. A) 180C - 12 hrs, B) 180C - 18 hrs, C) 180C - 24 hrs, D) 200C - 12 hrs, E) 200C - 18 hrs, F) 200C - 24 hrs, G) 220C - 12 hrs, H) 220C - 18 hrs, I) 220C - 24 hrs

In summary, the SEM results showed that the molten hydrothermal method was only successful in producing faceted particle morphologies of BT. Similarly, the aqueous hydrothermal method was only able to produce faceted particle morphologies of ST. The differences in the results between the two materials may be related to the differences in reactivity and solubility of the barium and strontium precursors.

2.3.3 Transmission electron microscopy

TEM micrographs of the cubic particles for BT, synthesized by the molten hydrothermal method at 220°C for 24 hours, and ST, synthesized by the aqueous hydrothermal method at 220°C for 24 hours, are shown in Figure 23. These samples were chosen to analyze via TEM because they showed very well-defined and uniformly sized faceted particles. They also produced the greatest yield of faceted particles among all the samples. The faceted particle morphology is clearly observed in the TEM micrographs (Figure 23(a) and (d)). The size of the nanocubes shown in the TEM micrographs for BT and ST were ~50 nm and 575 nm respectively. The fast Fourier transform (FFT) micrographs are shown in Figure 23(b) and (e). The interplanar spacings from the FFT micrographs were determined as 0.41 and 0.31 nm for BT and ST respectively. This differs from the interplanar spacings calculated from the X-ray diffraction peaks, where the interplanar spacings were 0.28 nm and 0.39 nm for BT and ST respectively. The electron diffraction patterns oriented about the 110 and 100 zone axis for BT and ST respectively are shown in 23(c) and Figure 23(f).

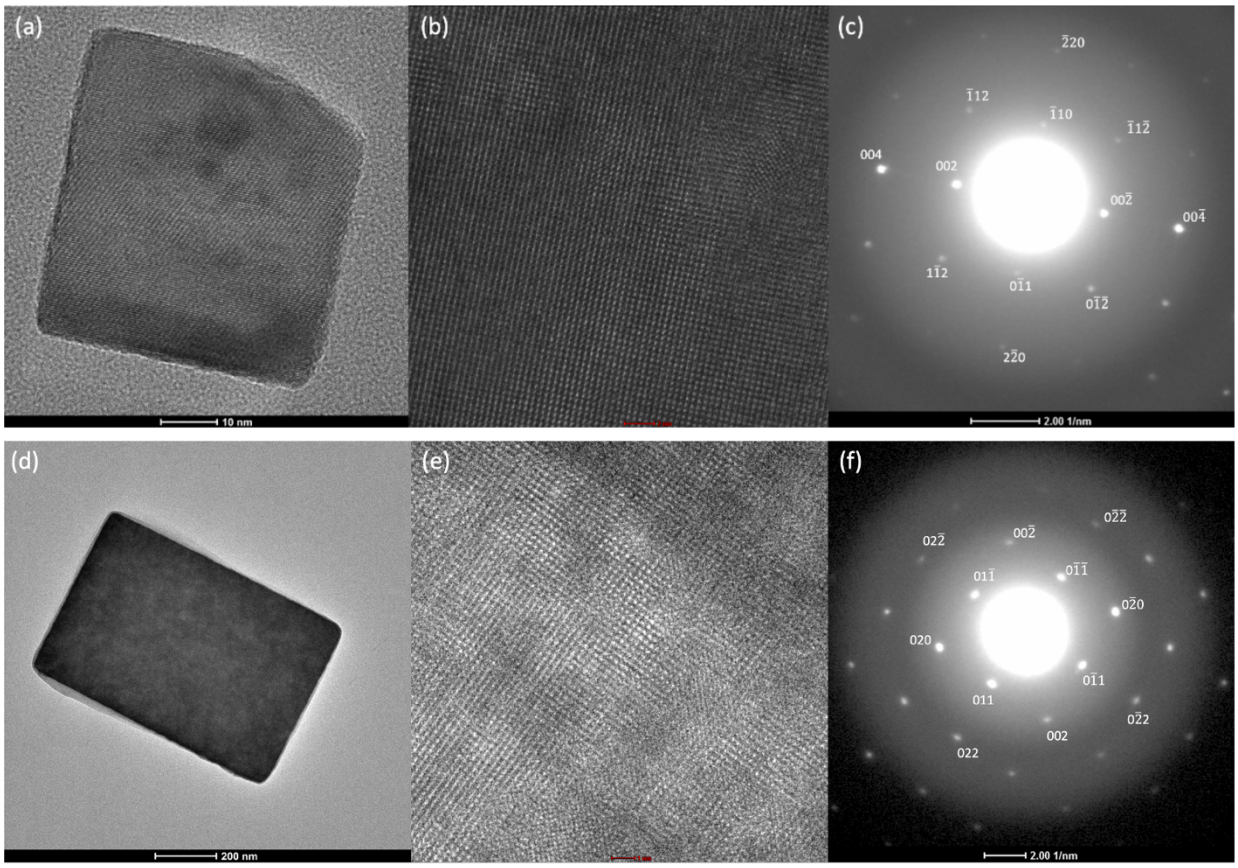

Figure 23 Transmission electron micrographs of A) 110 zone axis of BT synthesized at 220C for 24h with molten hydrothermal method and B) 100 zone axis of ST synthesized at 220C for 24h with aqueous hydrothermal method

2.3.4 Faceted particle formation mechanisms

Two main growth mechanisms have been proposed for the hydrothermal synthesis BT, in situ and dissolution-precipitation. The in-situ growth process involves the reaction of TiO_2 with dissolved barium from the precursor. As the reaction continues a layer of $BaTiO_3$ begins to form on the surface of TiO_2 and continues to grow as more barium diffuses and until the TiO_2 is consumed. It has also been speculated that the nucleation of nanocubes in the amorphous colloidal gel of the titanium precursor and the coalescence and aggregation of the nucleates lead to larger cubic particles. Within the colloidal gel the nucleates orient themselves into preferential directions to aggregate and reduce the high energy surfaces and the overall free energy of the

system [70]. The suppressed crystal growth of certain crystallographic planes allows for faster exposure of characteristic planes of the cubic structure. An important factor in the successful production of cubic particle morphologies is controlling the growth rate of the {100} surfaces. In BT the {110} surfaces have a higher density of metal ions, creating a protective shell on these surfaces reduces the growth rate along these directions so that other surfaces like {100} are able to grow faster giving rise to the cubic particle structure [71].

The second growth mechanism that has been previously reported for the hydrothermal synthesis of both BT and ST faceted particles is dissolution-precipitation [65][94][95]. This growth method begins with the breakdown of the titanium precursor to form $Ti(OH)_x^{4-x}$ that will later dissolve and react with barium ions to precipitate BT [94]. Contrary to. The in-situ growth, the dissolution-precipitation involves a fast dissolution of the titanium precursor which provides sufficient Ti to allow the reaction to come to completion and be able to form the faceted particles. This means that for an in-situ growth a lack of Ti would result in unreacted barium. This was seen in the X-ray diffraction patterns of the ST sample synthesized by the molten hydrothermal method at 180°C for 18 hours (Figure17(a)). The X-ray diffraction patterns also show these ST samples to be more amorphous. This unreacted precursor and the amorphous state suggest an in-situ growth mechanism of ST at low synthesis temperatures and times. Unlike ST, this was not observed for the BT samples synthesized by the molten hydrothermal method.

The SEM micrographs of the preliminary molten hydrothermal synthesis experiments shown in Figure 18 demonstrated the effect of time on the development and growth of the BT faceted particles (see Figure 18(a)-(d)). The size of the particles increased, from ~80 nm to >100nm, with longer synthesis times as shown in Figure 18(a)-(d). There was a larger distribution of small and large faceted particles for the samples synthesized at the longer times. The SEM

micrographs also show evidence of the formation of longer rod-like structures for the longer synthesis times, shown in Figure 18(d). Figure 24 shows a closer inspection of the BT cubic particles composed of a grid like pattern of small components, ~1-2 nm in size.

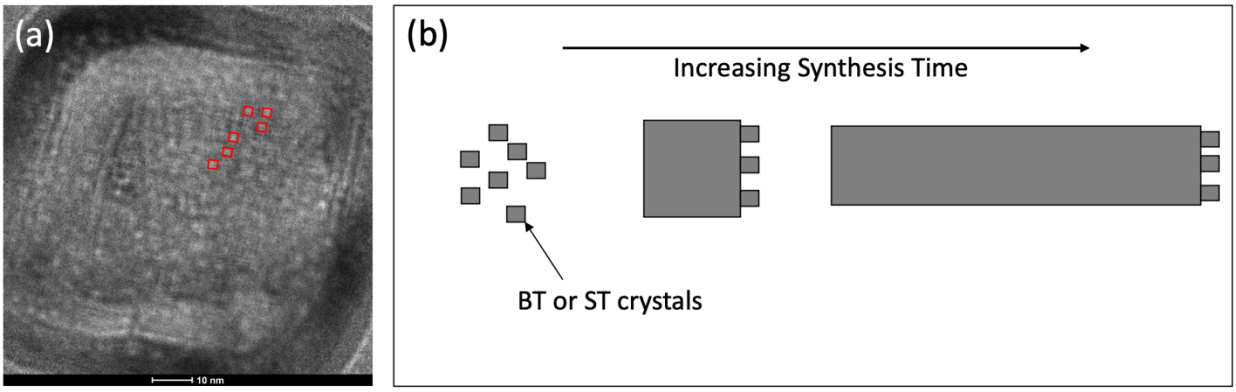

Figure 24 (a) Transmission electron micrograph of ST synthesized by the aqueous hydrothermal method at 220°C for 24 hours. The micrograph shows a grid-like pattern, marked with the red squares, on the faceted particle suggesting the coalescence of smaller crystallites in specific crystallographic directions to produce the larger faceted particle. (b) Schematic of the growth mechanism of the smaller crystallites into larger faceted particle structures with increasing synthesis time.

The results of the SEM and TEM evaluations suggest aggregation of smaller crystallites along specific crystallographic directions to form the larger faceted particles. For synthesis times lower than 24 hours the faceted particles tend to grow uniformly and have an average size of 80-100 nm (see Figure 17(a)). The coalescence of these smaller cubic particles begins to happen at synthesis times above 24 hours. These samples show a larger range of faceted particle sizes from the 80-100 nm to faceted particles as large as 500 nm (see Figure 17(d)). The TEM micrograph shown on Figure 24 suggests that these larger faceted particles are able to grow as a result of the aggregation of the smaller nanocubes. The SEM micrographs summarized on Figure 17 suggest that the aggregation of the smaller nanocubes occurs on preferential faces, indicated by the formation of the rod-like structures at the longer synthesis times (see Figure 17(b)-(c)). Further

synthesis time causes even further growth of the rod-like structures (see Figure 17(d)). The development of these faceted morphologies through aggregation for BT synthesized by the molten hydrothermal method can be described by the model shown in Figure 24.

In summary, the results of the X-ray diffraction, SEM and TEM results suggest the growth of faceted particles of BT and ST through aggregation of smaller crystallites in specific crystallographic directions. The growth mechanism for the ST sample synthesized by the molten hydrothermal method was proposed as in-situ, while the growth mechanism for all other samples was proposed as dissolution-precipitation.

2.4 Conclusions

Perovskite materials like barium titanate and strontium titanate have been promising materials for applications as ferroelectrics and multilayer capacitors. Morphology control of the particles of these materials can enhance the electronic properties like the dielectric constant and the ferroelectricity behavior. This study looked at understanding the formation mechanisms of faceted particles of barium titanate and strontium titanate synthesized by the molten hydrothermal and aqueous hydrothermal methods. SEM results showed the successful development of faceted particles for BT synthesized by the molten hydrothermal method and for ST synthesized by the aqueous hydrothermal method. X-ray diffraction results revealed the presence of unreacted $SrCO_3$ and an amorphous structure for the ST sample synthesized by the molten hydrothermal method, suggesting an in-situ growth mechanism of ST. The TEM results suggested the formation of faceted particles through aggregation of smaller crystallites in the identical crystallographic directions.

Acknowledgements

The dissertation author greatly acknowledges the undergraduate student researchers on this team who contributed to the synthesis of these materials, Paul Barraza and Jarren Ayars. The dissertation also acknowledges the master's student researcher who helped with the synthesis and characterization of the samples, Jin Zhou. Lastly, the dissertation author also acknowledges the Xtreme Materials Laboratory Research Scientist, Ekaterina Novitskaya, for all her help on X-ray diffraction of some of the synthesized samples.

Chapter 2, in part is currently being prepared for submission for publication of the material. Sanchez, Maritza; Barraza, Paul; Ayars, Jarren; Zhou, Jin; and Graeve, Olivia, A. The dissertation author was the primary author of this chapter.

Chapter 3 Phase Transitions and Oxidation Behavior During Oxyacetylene Torch Testing of TaC-HfC Solid Solutions

3.1 Abstract

Tantalum carbide (TaC) and hafnium carbide (HfC) have some of the highest melting temperatures among the transition metal carbides, borides, and nitrides, making them promising materials for high-speed flight and high temperature structural applications. Solid solutions of TaC and HfC are of particular interest due to their enhanced oxidation resistance compared to pure TaC or HfC. This study looks at the effect of Hf content on the oxidation resistance of TaC-HfC sintered specimens. Five compositions (100 vol.% TaC, 80 vol.% TaC + 20 vol.% HfC, 50 vol.% TaC + 50 vol.% HfC, 20 vol.% TaC + 80 vol.% HfC, and 100 vol.% HfC) were fabricated into bulk samples using spark plasma sintering (2173 K, 50 MPa, 10 min hold). Oxidation behavior of a subset of the compositions (100 vol.% TaC, 80 vol.% TaC + 20 vol.% HfC, and 50 vol.% TaC + 50 vol.% HfC) was analyzed using an oxyacetylene torch for 60 s. The TaC-HfC samples exhibited a reduction in the oxide scale thickness and the mass ablation rate with increasing HfC content. The improved oxidation resistance can be attributed to the formation of a $Hf_6Ta_2O_{17}$ phase. This phase enhances oxidation resistance by reducing oxygen diffusion and serving as a protective layer for the unoxidized material. The superior oxidation resistance of TaC-HfC samples makes these materials strong contenders for the development of high-speed flight coatings.

3.2 Introduction

Ultra-high temperature ceramics have been identified as promising materials for nozzle throats/liners, jet engine components, and high-speed aircraft, among many other unique uses [96][97][98][99]. This broad family of materials includes borides [100][101][102], carbides

[103], and nitrides, that exhibit extremely high melting temperatures resulting in high chemical stability [104][105][106][107], in some cases high thermal and electrical conductivities [108][109][110], and significant strength and hardness [111][112][113][114]. In particular, transition metal carbides such as tantalum carbide (TaC) and hafnium carbide (HfC) have gained significant interest because they possess the highest melting temperatures, above 4000 K, among transition metal carbides [115]. TaC and HfC crystallize in the cubic rock-salt ($Fm\bar{3}m$) structure, and exhibit mixed covalent, ionic, and metallic bonding [116], which gives rise to high thermal conductivity (~55.8 W/m•K) [117], significant flexural strength (~500 MPa) [118][119], and relatively high hardness (~15 GPa) [120][121]. These carbides can also form a passive oxide surface layer that provides some oxidation resistance. However, improving oxidation resistance in these materials is still a critical issue to enable their use in high-temperature applications [122].

Previous oxidation studies [123][124] of monolithic TaC have shown limitations in its oxidation resistance at high temperatures. Specifically, the formation and presence of α-Ta_2O_5 on the surface of TaC causes melting at temperatures (~2145 K) much lower than the melting temperature of TaC (4041 K) [115], thus the resistance to temperature is very negatively impacted. Additionally, the formation of the α-Ta_2O_5 melt further attacks the original, unoxidized material (*i.e.*, increases the amount of oxidized material recession) causing thicker, porous oxide layers and delamination. Furthermore, the porosity present in the oxide layer exacerbates oxygen diffusion and reduces the mechanical integrity. Monolithic HfC exhibits better oxidation resistance than TaC due to the creation of a three-layer structure consisting of an HfO_2 outer layer, a dense intermediate layer containing hafnium, carbon, and oxygen, and the unoxidized bulk carbide. The intermediate layer has good adhesion to the HfO_2 outer layer and to

the unoxidized bulk material, preventing delamination of the oxide [125]. The lack of cracks and pores allow the intermediate layer to act as an oxygen diffusion barrier and prevent further oxidation of the bulk carbide [125][126]. Although HfC outperforms TaC at high temperatures (>2273 K), it can still develop a highly porous HfO_2 layer that provides poor oxidation resistance at temperatures below 2073 K, making it unsuitable for high-temperature and high-speed applications [127].

The development of TaC-HfC solid solutions is promising for improving the oxidation resistance beyond that of the individual constituents [128]. Although there are very limited studies on the oxidation performance of such samples, preliminary oxyacetylene torch tests have shown the development of a protective, crack-free oxide layer, although it is on solid solutions that also contain $MoSi_2$ [129]. The superior oxidation resistance is related to the presence of an intermediate tantalum/hafnium oxide phase ($Hf_6Ta_2O_{17}$). This phase serves as a barrier between liquid Ta_2O_5 and solid HfO_2, leading to the development of a scaffold structure that prevents further materials recession of the underlying bulk carbide [128]. While this is an excellent first step, a more refined and comprehensive understanding of the oxidation resistance in these materials is necessary. For this purpose, the oxyacetylene torch is becoming a popular rapid screening technique as a ground test to replicate heat fluxes expected in high-speed flight.
In this study, we describe the relationship between chemical composition and oxidation resistance of TaC-HfC samples prepared using the spark plasma sintering technique. We prepared various compositions (single-phase 100 vol% TaC, 80 vol.% TaC + 20 vol.% HfC solid solution, 50 vol.% TaC + 50 vol.% HfC solid solution, 20 vol.% TaC + 80 vol.% HfC solid solution, single-phase 100 vol% HfC) and measured their densities and hardness values. Lower relative densities were obtained for the 20 vol.% TaC + 80 vol.% HfC solid solution and the

single-phase100 vol% HfC sample. To allow for accurate comparison between all compositions, only those with higher relative densities were studied for oxidation resistance. Oxyacetylene torch tests of single-phase TaC, 80 vol.% TaC + 20 vol.% HfC solid solution, and 50 vol.% TaC + 50 vol.% HfC solid solution, were completed and the surface phases and elemental compositions were determined from X-ray diffraction and energy dispersive X-ray spectroscopy. As a result, we show the influence of composition on oxidation resistance in this paper.

3.3 Experimental Procedure

Commercial tantalum carbide (TaC, American Elements, 99.5%, 325 mesh) and hafnium carbide (HfC, Stanford Advanced Materials, 99.5%, 50-150 micrometer size) powders were used as starting materials. As-received powders were ball milled for 24 hours using ethanol as the solvent and 5.15 mm SiC milling media to reduce particle size. The ball-to-powder weight ratio was 3:1. Powders were dried using a rotary evaporator. The particle sizes of the ball-milled powders were measured using a laser diffraction particle size analyzer (Beckman Coulter LS 13 320). Corresponding amounts of ball-milled TaC and HfC powders were weighed to produce compositions 100TaC (*i.e.*, 100 vol.% TaC), 80TaC-20HfC (*i.e.*, 80 vol.% TaC and 20 vol.% HfC), 50TaC-50HfC, 20TaC-80HfC, and 100HfC. The TaC-HfC mixtures were ball milled for an additional 24 hours in ethanol using 5.15 mm SiC media. In preparation for spark plasma sintering, 15 g of powder for each composition were loaded into a 20 mm graphite die to create a ~3 mm thick pellet. The samples were densified on a FCT Systeme GmbH HP D25 system at a temperature of 2173 K using a heating rate of 100 K/min for a 10 min hold time at temperature and a pressure of 50 MPa. Densities of the sintered specimens were determined using the Archimedes method. Vicker's microhardness was measured using a QATM Qness60 A+ with

Qpix Control2 software, using a 1 kgf load and 12 s dwell time. Five different microhardness indents were measured for each sample.

Oxidation tests were conducted using an oxyacetylene torch. The samples were mounted on a mechanical stage that positions the samples at the desired distance from the torch tip, thus controlling the heat flux experienced by the sample. The sample was mounted at a 90° angle relative to the torch tip, and the sample was swung into the lit torch (0°) via a rotary motor to begin the oxidation test. The 100TaC, 80TaC-20HfC, and 50TaC-50HfC samples were exposed to the torch for 60 s at a heat flux of 400 W/cm^2, corresponding to a distance of 52 mm from the torch tip. The heat flux at this distance was measured using a Gardon gauge (TG-1000-52, Vatell Corporation). The gas flow rates were 8 slpm for acetylene and 10.81 slpm for oxygen. The fuel to oxidizer ratio was 0.74. The surface temperature and emissivity values of the samples were measured using a Teledyne FLIR one-color pyrometer (FLIR A300 series with FLIR ResearchIR software; T: -15-3000°C) and a Pyrofiber® Lab Automatic Emissivity Measurement System (AEMS) one-color pyrometer with laser pulse (Pyrofiber Lab System, Pyrometer LLC; T: 850-3000°C). The phases of the powders and densified samples before and after oxidation testing were identified using X-ray diffraction on a Bruker D2 Phaser with Lynxeye (1D mode) detector and Cu Kα radiation. The surface and cross sections of each oxidized sample were evaluated using scanning electron microscopy and energy dispersive X-ray spectroscopy on a FEI Quanta 650 system with a Zeiss Gemini 500 Xmax 80 detector.

3.4 Results and Discussion

Scanning electron micrographs of commercial TaC (100TaC), mixed TaC-HfC [corresponding to 80 vol.% TaC + 20 vol.% HfC (80TaC-20HfC), 50 vol.% TaC + 50 vol.% HfC (50TaC-50HfC), and 20 vol.% TaC + 80 vol.% HfC (20TaC-80HfC) mixtures prepared by ball

milling], and commercial HfC (100HfC) powders after milling are illustrated in Figure 25. The average particle sizes of the as-received powders were 0.7 μm and 1.8 μm for TaC and HfC, respectively. The particle sizes of the powders after milling, listed in Table 3, increase with HfC content since the HfC powders are larger compared to TaC both in the as-received state and after milling. High relative densities were achieved for the 100TaC (100.6%), 80TaC-20HfC (100.4%), and 50TaC-50HfC (97.9%) samples consolidated using the spark plasma sintering technique, which has been effectively used for densification of carbides [130][131][132], as well as a variety of other materials [133][134][135][136][137][138][139]. One of the benefits of this sintering technique is the capability to consolidate difficult to sinter powders, such as carbides, at lower temperatures compared to other techniques [140][141][142][143], thus the relevancy of its use in this study.

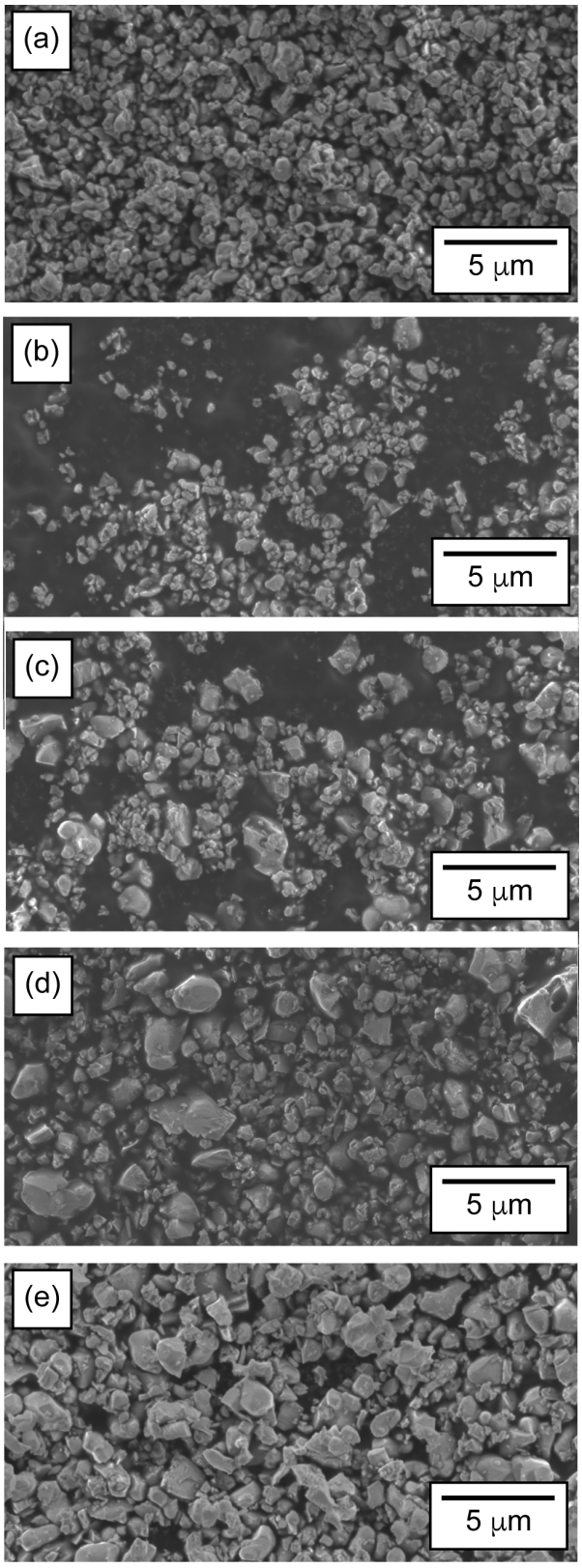

Figure 25 Scanning electron micrographs of ball milled (a) 100TaC, (b) 80TaC-20HfC, (c) 50TaC-50HfC, (d) 20TaC-80HfC, and (e) 100HfC powders.

Table 3 Particle size of the ball-milled powders, relative density and hardness values of TaC, TaC-HfC composites, and HfC following spark plasma sintering. Values for density and hardness reported from literature are also provided.

Composition (vol.%)	Particle size (μm)	Relative density (%)	Hardness (GPa)	Reported relative density (%)[121]	Reported hardness (GPa)[121]
100TaC	0.7 ± 0.6	100.6	14.9 ± 0.4	97.2	14.9 ± 0.3
80TaC-20HfC	0.6 ± 0.6	100.4	22.6 ± 0.5	97.8	18.1 ± 0.2
50TaC-50HfC	0.7 ± 0.6	97.9	22.2 ± 0.7	97.7	19.9 ± 0.6
20TaC-80HfC	0.9 ± 0.6	93.6	24.2 ± 0.5	97.5	18.4 ± 0.3
100HfC	1.3 ± 0.8	95.1	20.4 ± 1.0	94.5	18.5 ± 0.5

The 20TaC-80HfC (93.6%) and 100HfC (95.1%) samples had lower densities and, thus, were not included in the oxyacetylene torch testing. This amount of porosity (~5%+) would likely dominate the ablation behavior of the materials, making it difficult to assess the role of the composition. The decrease in density in these two latter samples is likely an effect of the larger particle sizes and particle size distributions (*i.e.*, larger standard deviation values) of the HfC powders (1.3 ± 0.8 μm) compared to all other powders. Larger particle size distributions are known to inhibit sintering due to rapid depletion of smaller grains by large neighboring grains, leading to a decreasing densification rate and reduction of necks between particles [144].

Hardness values for all samples are listed in Table 3. The lower relative density of the 100HfC sample (95.1%) may also explain the lower hardness of this sintered sample [115], compared to the 80TaC-20HfC (H_v = 24.2 ± 0.5 GPa) and 50TaC-50HfC (H_v = 22.2 ± 0.7 GPa) samples. Previous studies have shown higher hardness values for mixtures with increasing hafnium content [145] due to the greater bonding energy between hafnium and oxygen, compared to tantalum and oxygen [146]. The slightly higher hardness value for the 20TaC-80HfC sample (24.2 ± 0.5 GPa) may be explained by the higher hafnium content, regardless of the lower density. One would expect a similar hardness behavior for the 100HfC sample (*i.e.*, it

should be higher), but as mentioned previously, the hardness value for this specimen is the lowest of all specimens. Similar behavior has been reported in literature. The solid solutions exhibit lattice distortions that occur from replacements if the Ta atoms with Hf atoms in the lattice. Since Hf atoms are greater in size then the Ta atoms then the distortions cause local stress fields that result in hardening [147].

The X-ray diffraction patterns for all sintered specimens are illustrated in Figure 26. All diffraction peaks of the 100TaC and 100HfC samples correspond to the TaC ($Fm\bar{3}m$, PDF 00-006-0524) and HfC ($Fm\bar{3}m$, PDF 00-039-1491) structures, respectively. Dashed lines in the figure demarcate the locations of the peaks in the powder diffraction files for each compound. The TaC-HfC samples exhibit diffraction peaks intercalated between the corresponding 100TaC and 100HfC peaks, indicating the formation of single-phase TaC-HfC solid solutions. This is expected since the TaC-HfC binary phase diagram [148] describes the formation of a TaC-HfC solid solution at a temperature of 1160 K and higher, significantly lower than the sintering temperature used in this study (2173 K), thus, thermodynamically there is an opportunity to form a solid solution. Peak shifts towards lower 2θ values for increasing hafnium content in the solid solutions, indicates that the lattice parameter increases due to the larger atomic radius of hafnium compared to tantalum [149].

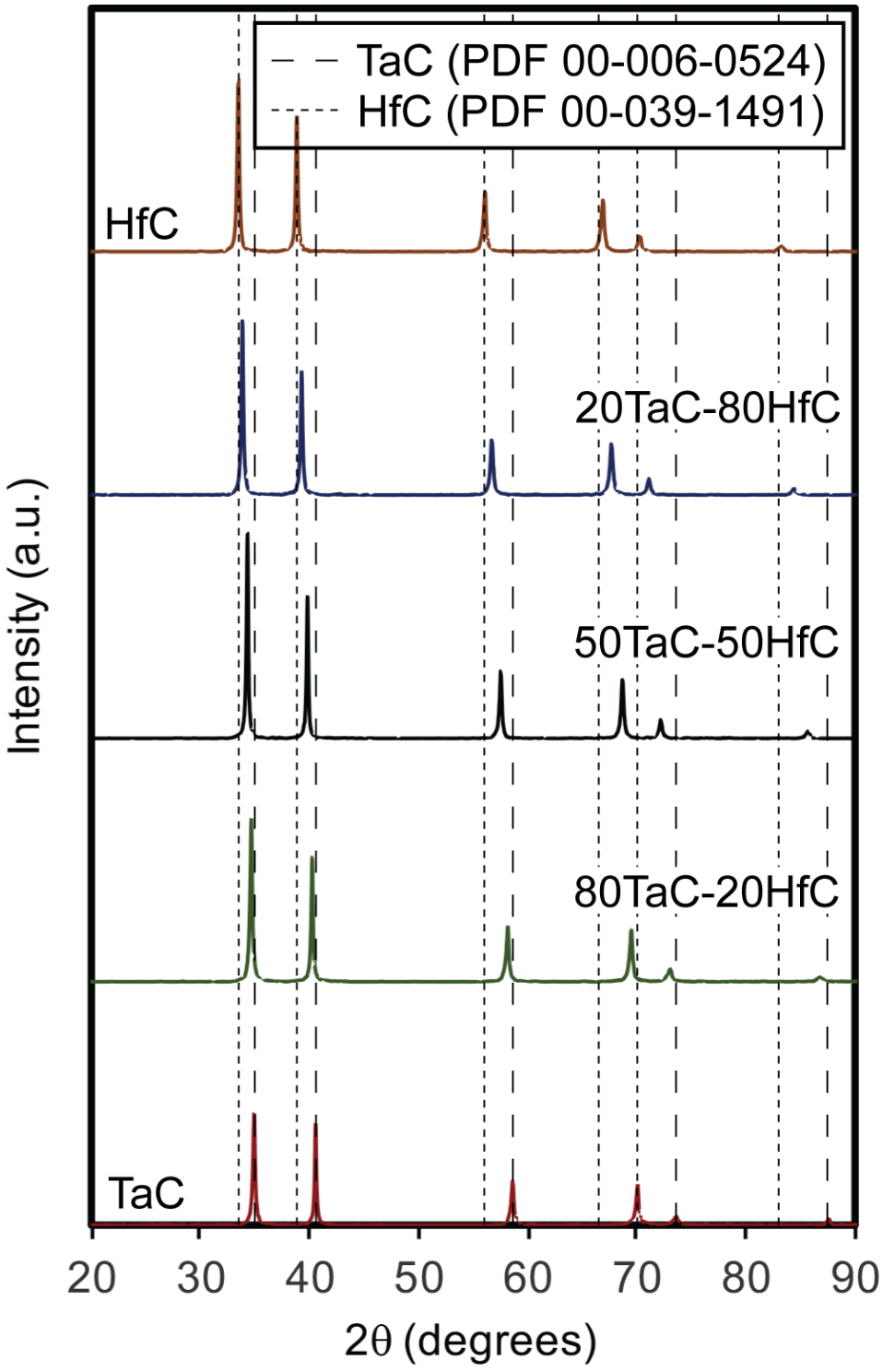

Figure 26 X-ray diffraction patterns of the TaC, TaC-HfC, and HfC sintered specimens. Dashed lines indicate peaks for TaC PDF 00-006-0524 (longer dashes) and HfC PDF 00-039-1491 (shorter dashes).

The emissivity-corrected temperature for the torch-facing surface of the 100TaC (T_{max} = 2021 K), 80TaC-20HfC (T_{max} = 1966 K), and 50TaC-50HfC (T_{max} = 1987 K) samples during oxidation testing are illustrated in Figure 27. The inset of Figure 27 shows a slightly more steady-state behavior (*i.e.*, decreased slope) of the 100TaC sample at the maximum temperature (~1873-2023 K) compared to the solid solutions. This likely occurs due to differences in thermal conductivity between TaC and HfC. The thermal conductivity of TaC (22.1 $W \bullet mK^{-1}$) is slightly higher than HfC (20 $W \bullet mK^{-1}$) and increases more rapidly with temperature [150][151]. As such, the 100TaC sample more effectively transfers heat allowing the sample to reach a steady-state temperature more quickly than the TaC-HfC samples. This also results in faster heating rates and higher maximum temperatures, which may not be desirable for high-speed vehicle applications, as it could lead to accelerated formation of the passive oxide phases and overall loss in structural rigidity [123].

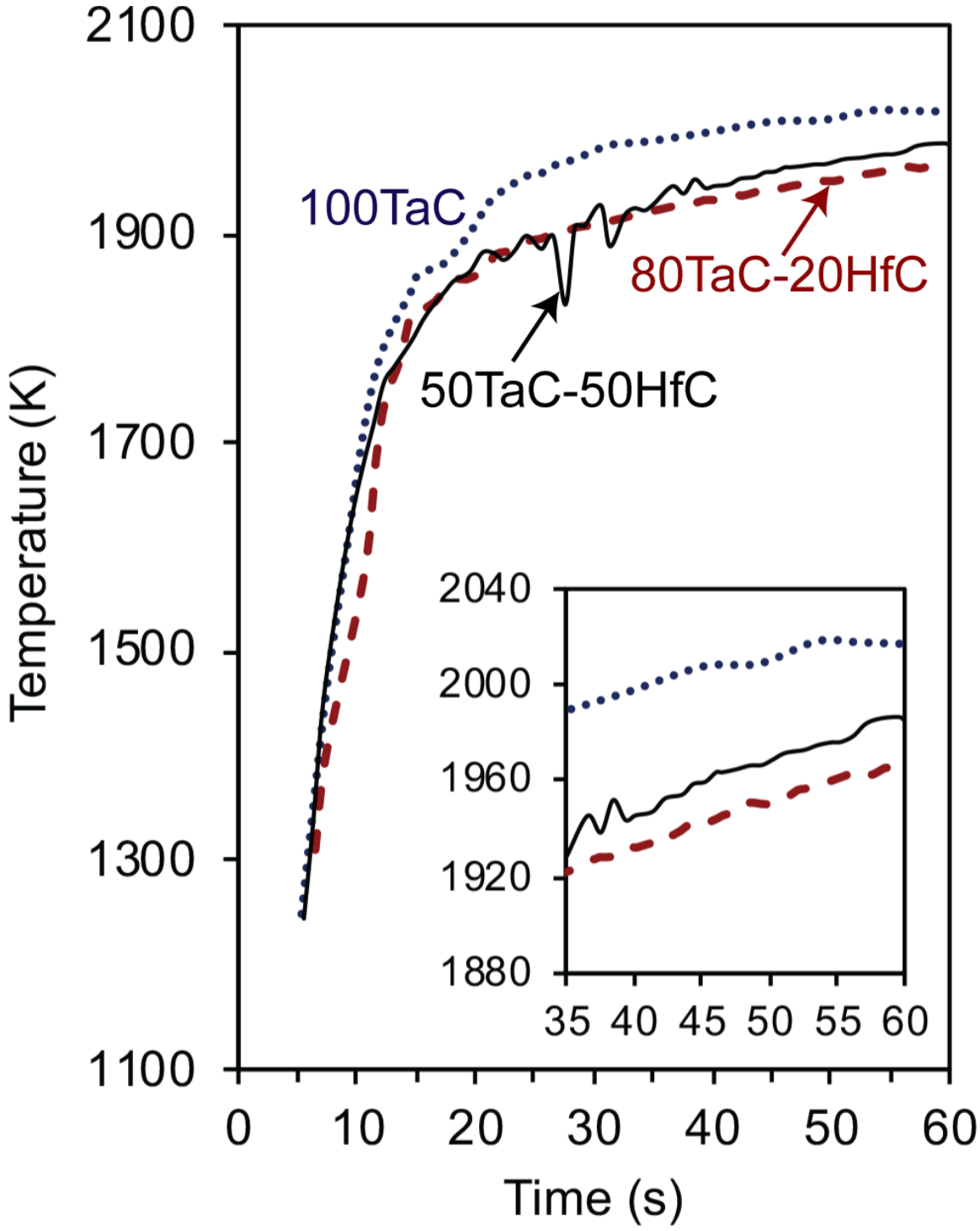

Figure 27 Emissivity-corrected temperature with respect to time for the torch-facing surface of the 100TaC (blue, short dashes), 80TaC-20HfC (red, long dashes), and 50TaC-50HfC (black, solid line) specimens during oxyacetylene torch testing.

The optical micrographs of the oxidized samples after torch testing are shown in Figure 28. The micrographs demonstrate higher oxidation for the 100TaC sample [Figure 28(a)], evident in the whiter coloration of the sample surface, compared to the TaC-HfC samples, which exhibit a slight gray coloration. The samples were dark gray before torch testing, typical of TaC and HfC. To quantify oxidation resistance, mass ablation rates were calculated, resulting in values of 2.1 mg/s for 100TaC, 1.4 mg/s for 80TaC-20HfC, and 0.8 mg/s for 50TaC-50HfC [Figure 29(a)]. Reduction in the mass ablation rate represents a lower mass of material undergoing ablation per unit time, equating to an increase in oxidation resistance. The rate decreases with increasing hafnium content, with the rate of the 50TaC-50HfC sample characterized by a value that is less than half compared to the 100TaC sample. Note in Figure 29(b)-(d) that the oxidation was uniform across the entire specimen, not in localized regions. The 80TaC-20HfC sample displayed evidence of delamination [Figure 29(c)]. Closer inspection on the SEM micrographs of the 50TaC-50HfC sample also revealed crack formation between the bulk material and the oxide layer, suggesting early stages of delamination. The delamination in the solid solution samples may be due to the development of local stresses as a result of lattice changes between the bulk material and the oxide layer. The bulk carbide material exhibits a cubic crystal structure and the oxides formed for the solid solutions display monoclinic (α-Ta_2O_5) and orthorhombic ($Hf_6Ta_2O_{17}$) structures. Similar to the effect on the hardness, the distortions that occur due to the replacement of Ta atoms by Hf atoms give rise to local stresses in the solid solutions which may be contributing to the delamination of the 80TaC-20HfC sample.

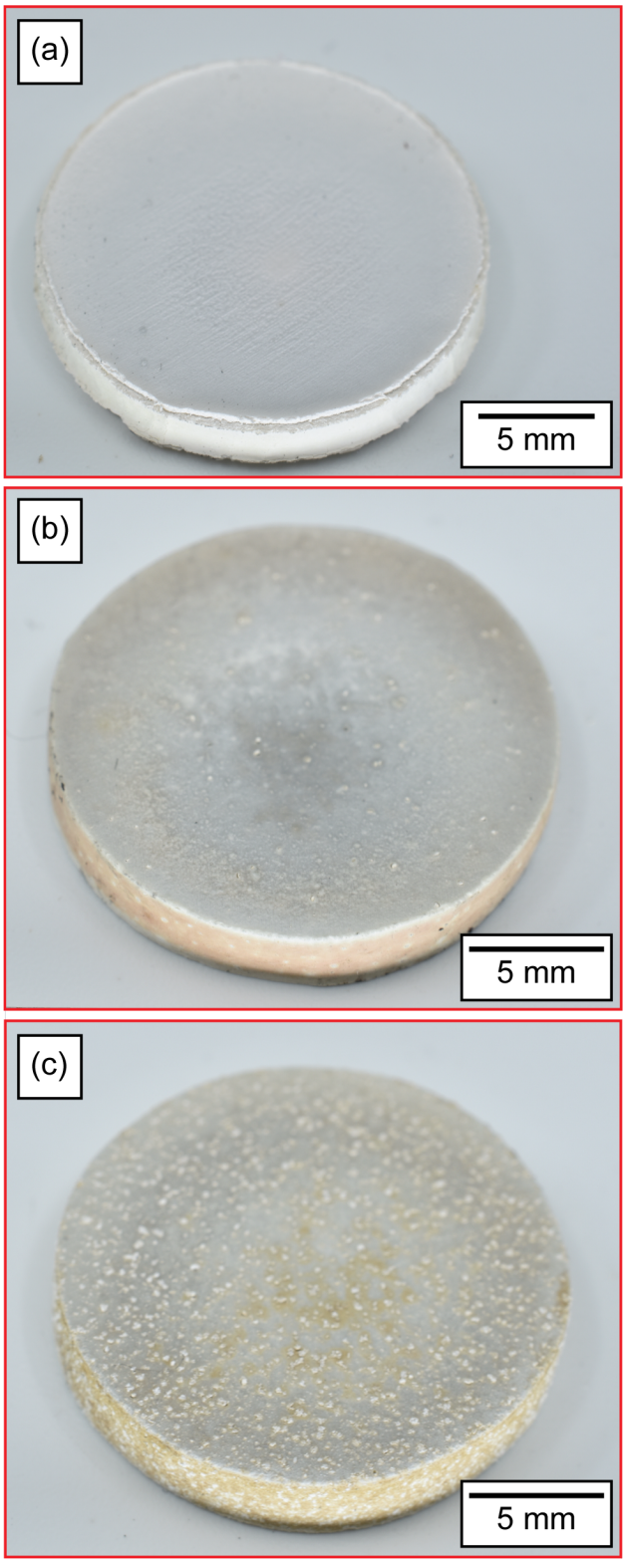

Figure 28 Optical micrographs of the (a) 100TaC, (b) 80TaC-20HfC, and (c) 50TaC-50HfC oxidized samples.

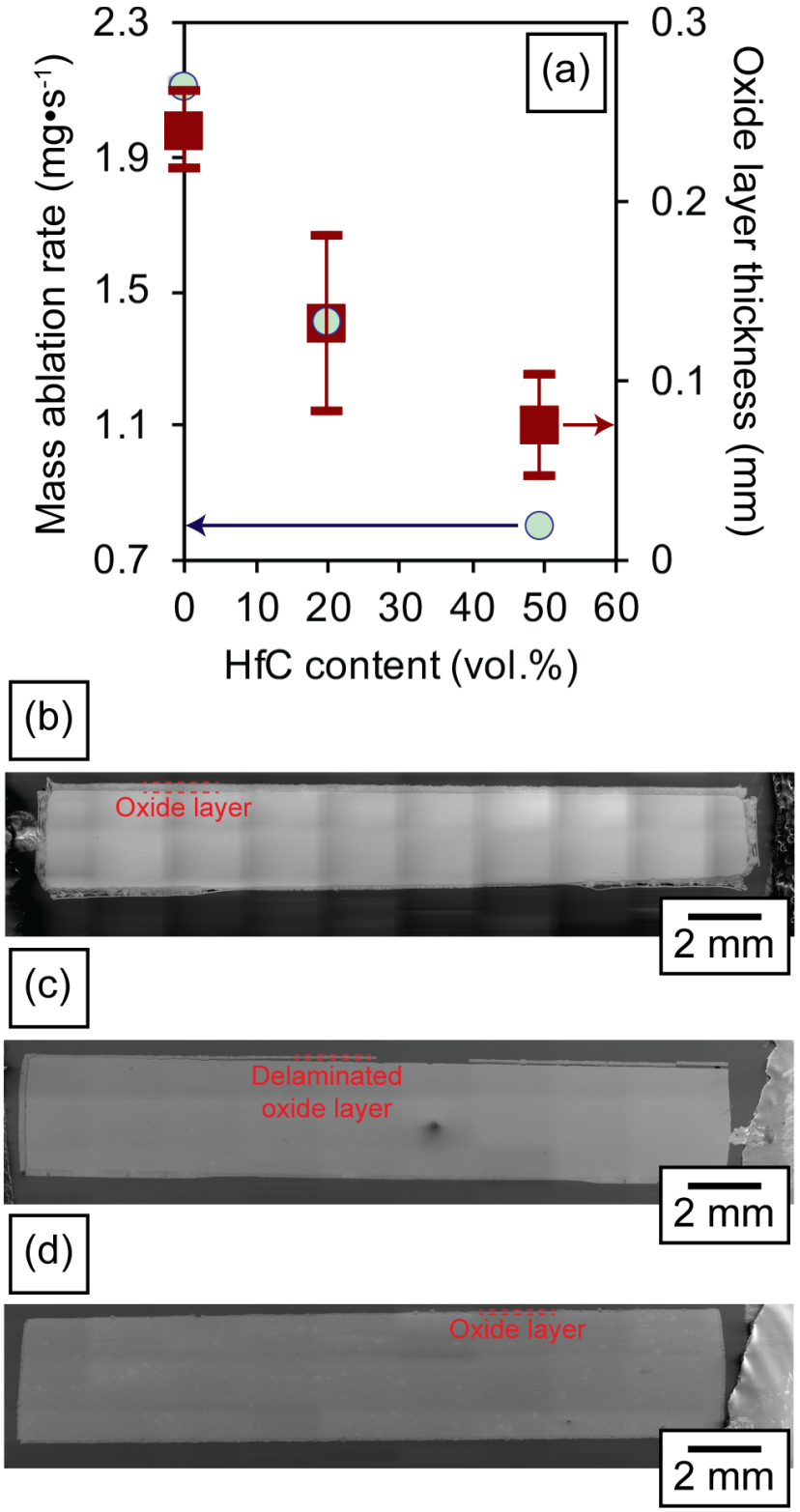

Figure 29 (a) Mass ablation rate and oxide layer thickness of torch-tested samples; the mass ablation rate (left y-axis) is represented by circles and the oxide layer thickness (right y-axis) by squares. Combined images from scanning electron micrographs of the (b) 100TaC, (c) 80TaC-20HfC, and (d) 50TaC-50HfC specimens after torch testing. Top of each image is the torch-facing side of the sample.

X-ray diffraction was used to identify the oxide phases that formed on the surface during torch testing, illustrated in Figure 30. The samples incorporate mainly α-Ta_2O_5. The triclinic Ta_2O_5 phase may be present, albeit minimally. Only the 50TaC-50HfC sample contains monoclinic HfO_2, whereas both samples containing Hf result in the formation of $Hf_6Ta_2O_{17}$ from the following chemical process [128]:

$$Ta_2O_5 + 6HfO_2 \longrightarrow Hf_6Ta_2O_{17}$$

From this, it can be surmised that the 80TaC-20HfC sample formed some small amount of HfO_2 that reacted with Ta_2O_5 to form the $Hf_6Ta_2O_{17}$ phase, depleting HfO_2 from the surface. Since the 50TaC-50HfC sample contains more hafnium, the amount of HfO_2 is higher and does not become depleted during the formation of the $Hf_6Ta_2O_{17}$ phase. Previous studies have described the formation of $Hf_6Ta_2O_{17}$ as a four-part process. First, the TaC-HfC solid solution forms α-Hf-O and a Ta-rich Ta-Hf solid solution. Then, the oxygen saturation of the α-Hf-O causes the transformation to monoclinic HfO_2 and Ta-rich Ta-Hf solid solution. Further diffusion of oxygen results in the development of monoclinic HfO_2, a metastable tantalum oxide phase, and a Ta-Hf-O solid solution that finally produces $Hf_6Ta_2O_{17}$ [152]. The driving force for the formation of the intermediate phases is a result of the slow kinetics of the process associated with the higher diffusivity of oxygen compared to tantalum and hafnium. The $Hf_6Ta_2O_{17}$ phase is known to improve oxidation resistance. It is thermally stable up to ~2523 K [153] and has low oxygen diffusion [152], resulting in a passive protective layer against further oxidation [128][154]. The presence of this phase is likely contributing to the reduction in the ablation rate and oxide scale thickness in our samples.

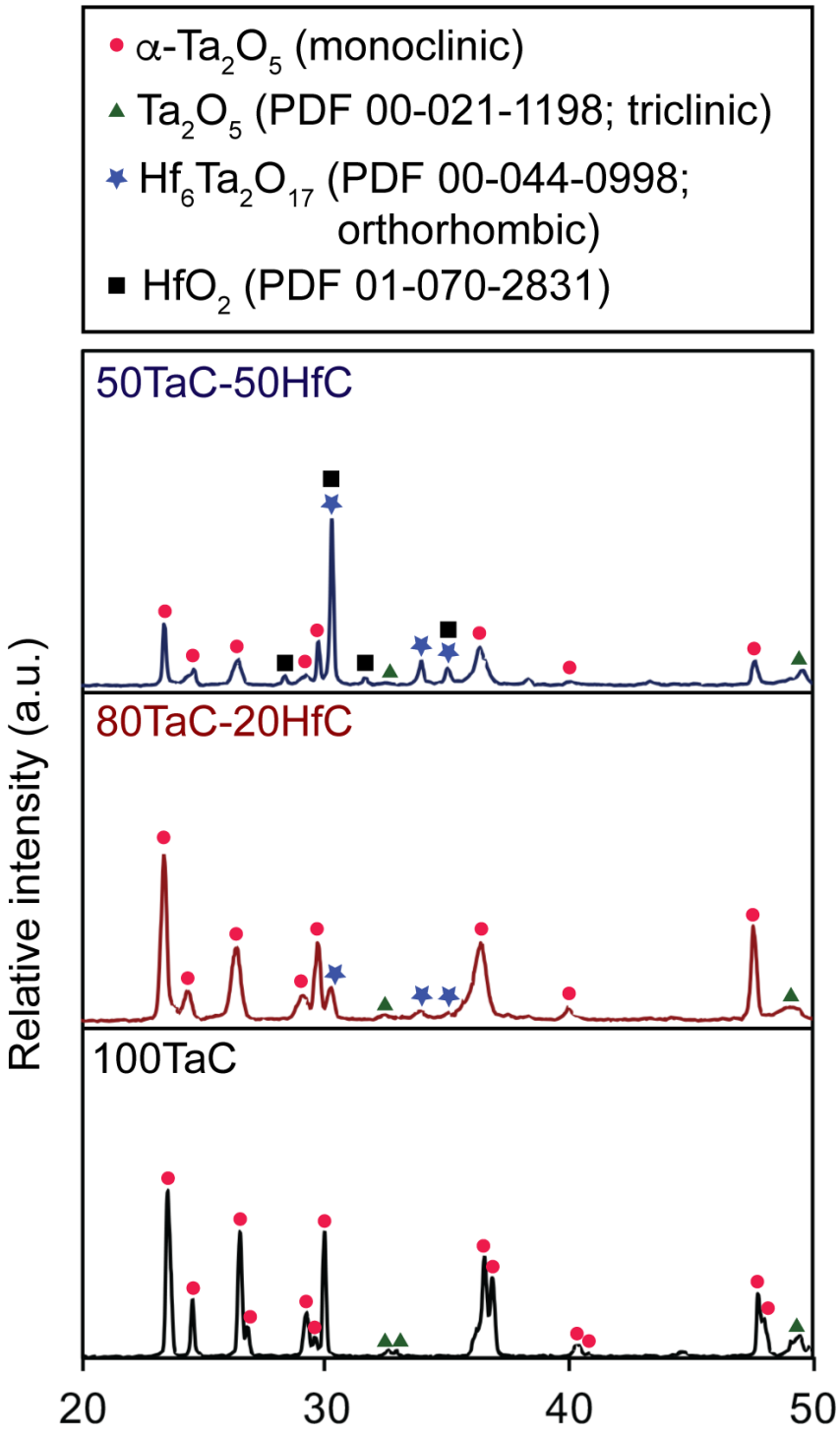

Figure 30 X-ray diffraction patterns of the torch-facing surface for the oxidized (a) 100TaC, (b) 80TaC-20HfC, and (c) 50TaC-50HfC specimens. As the content of Hf is increased, the peaks associated with $Hf_6Ta_2O_{17}$ phase increase in intensity, whereas the peaks associated with Ta_2O_5 decrease in intensity. The monoclinic phase of Ta_2O_5 has several PDF cards that are very similar (PDF #00-01801303, #01-075-9706, #00-018-1303, #00-027-1447). The presence of the triclinic form of Ta_2O_5 is somewhat speculative, as the peaks have very low intensity.

Figure 31 illustrates the energy dispersive spectroscopy maps of the three oxidized samples. The oxide scale thickness decreases as the hafnium content increases [see Figure 31(a), (e), and (j)], as previously discussed. The homogeneous Ta- and O-rich areas within the oxide scale in the 100TaC sample [Figure 31(b) and (d)] are likely corresponding to the α-Ta_2O_5 phase identified from X-ray diffraction (Figure 30). A line scan across the oxide scale [Figure 32(a)] corroborates the results from the X-ray mapping, where we see a significant increase in the oxygen signal within the scan region demarcated by the two dashed lines. The 80TaC-20HfC and 50TaC-50HfC samples both have tantalum [Figure 31(f) and (k)] and hafnium [Figure 31(i) and (n)] in the oxide layer, likely the $Hf_6Ta_2O_{17}$ phase. The 80TaC-20HfC sample exhibits a homogenous distribution of the Ta, Hf, and O [Figure 31(f), (h), and (i)] throughout the oxide scale, indicating absence of the HfO_2 phase and supporting the X-ray diffraction findings. A large majority of the oxide layer is then composed of the α-Ta_2O_5 phase and regions of the $Hf_6Ta_2O_{17}$ phase, based on the phase information obtained from X-ray diffraction in Figure 30 and from the variations in Hf concentration from the energy dispersive X-ray line scan in Figure 32(b), which indicates the presence of small, dispersed, regions of $Hf_6Ta_2O_{17}$ as the scan moves across the oxide layer, resulting in peaks of Hf. The 50TaC-50HfC sample exhibits Hf- and O-rich regions within the oxide layer, most evident between 40 and 60 μm [Figure 32(c)], which shows significant variation in the Hf and O signal as the scan moves across the oxide layer, which can be attributed to the HfO_2 phase identified from X-ray diffraction. Directly below the oxide layer at approximately 80 μm, the composition gradually changes to Hf and C. The deeper unoxidized sections of the sample show the presence of Hf, Ta, and C, beyond the ~80 μm interface. This coincides with the layered structure described by Yang *et al.* [152] where the

oxide layer consists of the $Hf_6Ta_2O_{17}$ phase followed by two intermediate layers that are Hf- and O-rich, and the bulk TaC-HfC solid solution.

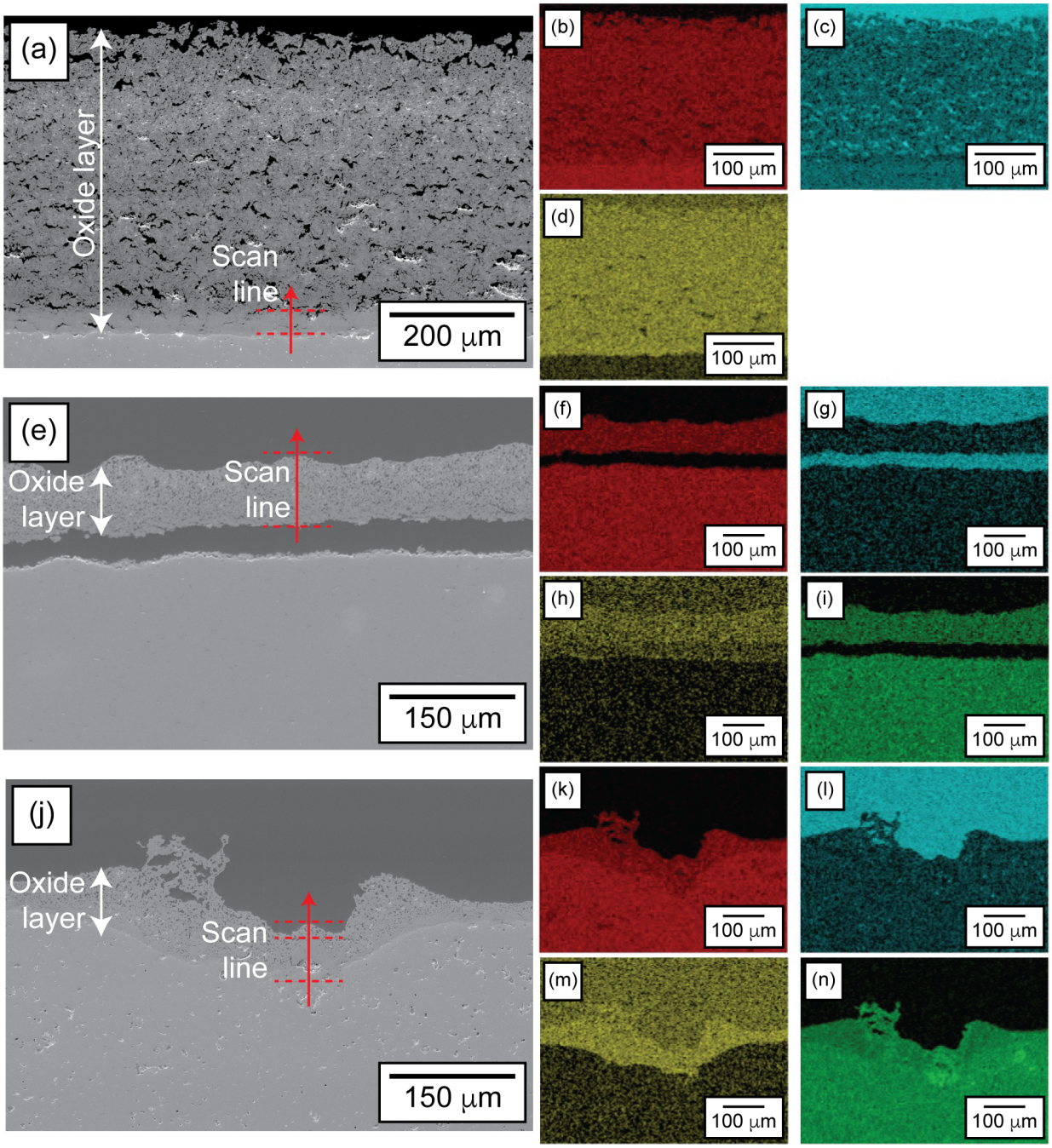

Figure 31 (a) Scanning electron micrograph, and X-ray maps of (b) Ta $M\alpha_1$, (c) C $K\alpha_{1,2}$, and (d) O $K\alpha_1$, of 100TaC. (e) Scanning electron micrograph, and X-ray maps of (f) Ta $M\alpha_1$, (g) C $K\alpha_{1,2}$, (h) O $K\alpha_1$, and (i) Hf $M\alpha_1$, of 80TaC-20HfC. (j) Scanning electron micrograph, and X-ray maps of (k) Ta $M\alpha_1$, (l) C $K\alpha_{1,2}$, (m) O $K\alpha_1$, and (n) Hf $M\alpha_1$, of 50TaC-50HfC. The arrow marked as the scan line is relevant to the results presented in Figure 32.

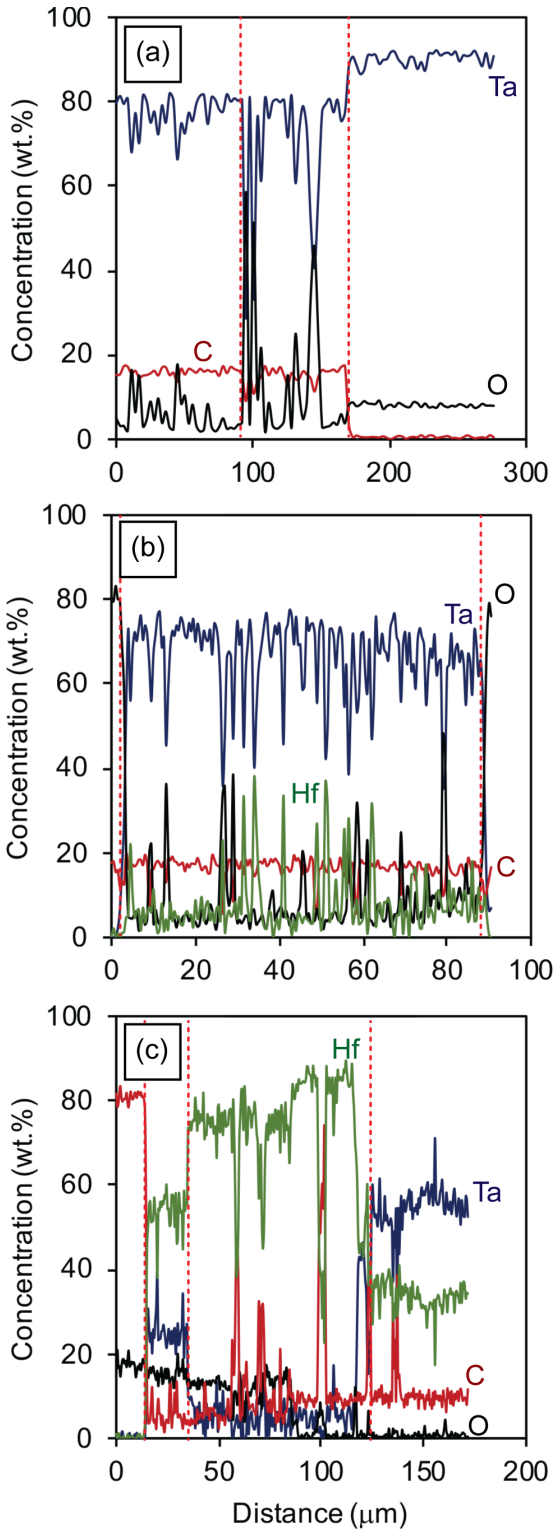

Figure 32 Energy dispersive line scans across the interface between the oxide layer and the unoxidized bulk material of the (a) 100TaC, (b) 80TaC-20HfC, and (c) 50TaC-50HfC samples. The red dashed lines correspond to the red dashed lines marked in the micrographs of Figure 31.

In summary, oxyacetylene torch tests were conducted on three spark plasma sintered samples (100TaC, 80TaC-20HfC, and 50TaC-50HfC) to assess the oxidation resistance of TaC-HfC solid solutions in comparison to TaC. Emissivity-corrected temperature curves showed a higher maximum temperature and a more steady-state behavior in the 100TaC sample compared to the TaC-HfC samples. The oxidized samples showed a decrease in mass ablation rates and oxide scale thickness with increasing Hf content. The improved oxidation resistance of the TaC-HfC samples can be attributed to the presence of a complex oxide phase, $Hf_6Ta_2O_{17}$, identified from X-ray diffraction. The high thermal stability and low oxygen diffusion of $Hf_6Ta_2O_{17}$ allows it to act as a protective oxide layer for the unoxidized carbide material. Energy dispersive X-ray line scans show the formation of two layers within the oxide scale for the 50TaC-50HfC sample, with a Hf-, Ta, and O-rich surface layer, followed by a Hf- and O-rich layer that decreases in oxygen concentration deeper into the oxide scale.

3.5 Conclusion

Transition metal carbides, including TaC and HfC, have some of the highest melting temperatures among the large family of carbide, boride, and nitride ceramics, making them promising materials for high-speed flight and high temperature structural applications. TaC-HfC solid solutions are of particular interest in efforts to improve the oxidation resistance of TaC and HfC. In this study, oxyacetylene torch tests were conducted on TaC and TaC-HfC sintered samples. X-ray diffraction results showed that the Hf content influences the oxide phase formation in the TaC-HfC solid solutions, resulting in $Hf_6Ta_2O_{17}$. This oxide phase is known to enhance oxidation resistance by reducing oxygen diffusion, thus serving as a protective layer for the unoxidized material. Energy dispersive X-ray line scans revealed a Hf-, Ta-, and O-rich surface layer on the oxide scale that transitions into Hf- and O-rich with decreasing oxygen

concentration further into the oxide scale. The TaC-HfC solid solutions showed a reduction in oxide scale from 0.24 μm for the 100TaC sample, to 0.13 for the 80TaC-20HfC sample, and 0.08 μm for the 50TaC-50HfC sample, and a mass ablation rate from 2.1 mg/s for the 100TaC sample, to 1.4 mg/s for the 80TaC-20HfC sample, and 0.8 mg/s for the 50TaC-50HfC sample. The results presented in this study show enhanced oxidation resistance in the TaC-HfC samples. As such, TaC-HfC solid solutions are promising materials for the development of next generation aerospace vehicle protective coatings.

3.6 Supplementary Experiments

3.6.1 Phase separation of HfC powders

The reduction in density of the 20TaC-80HfC and 100HfC samples (Table 3) can be related to the larger particle sizes of the starting HfC powder, evidence from the higher densities of the samples with larger TaC content. In efforts to increase the density of the 20TaC-80HfC and 100HfC samples phase separation experiments were conducted to try to reduce the starting particle size of the HfC powder. The ball-milled powders of 100HfC were dispersed in isopropanol alcohol (IPA) and centrifuged at various RPMs for 1 min to separate and collect the smaller particles in the solution. The ball-milled powders were centrifuged at 1000 RPM. The solution, after centrifugation, was collected and any sedimentation on the bottom or the sides of the container was removed from the next round of centrifugation. The size of the particles dispersed in solution were measured using a laser diffraction particle size analyzer (Beckman Coulter LS 13 320). The collected solution was centrifuged again at 1000 RPM for 1 min and any sedimentation on the bottom or the sides of the container was removed. The size of the particles dispersed in the resultant solution were again measured using the Beckman Coulter particle size analyzer.

The particle size analyzer results showed a significant decrease in particle size after each round of centrifugation as shown in Figure 33. The HfC powder after ball-milling and before centrifugation had a d_{50} value of 1.63 μm. After one round of centrifugation at 1000 RPM for 1 min, the d_{50} value of the powder was reduced to 1.082 μm. After an additional round of centrifugation at 1000 RPM for 1 min the d_{50} value was reduced even further to 0.773 μm, less than half of the original d_{50} value before any centrifugation.

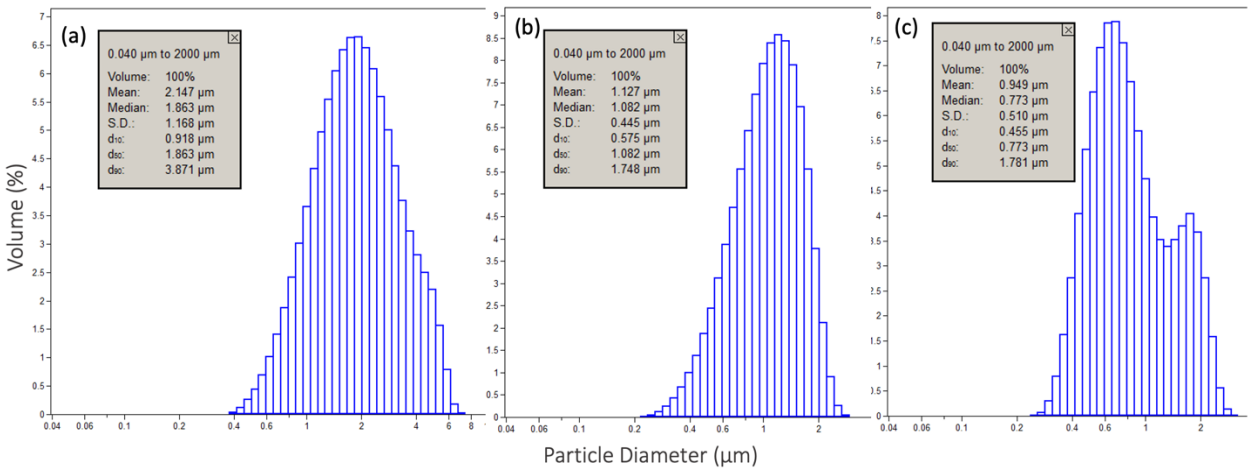

Figure 33 Particle diameter vs. volume percent of HfC powders (a) after ball-milling and before centrifugation, (b) after centrifugation at 1000RPM for 1 min, and (c) after two rounds of centrifugation at 1000 RPM for 1 min.

Although the phase separation experiments led to a successful decrease in particle size of HfC, the time needed to yield enough powder for Spark Plasma Sintering (SPS) would be significant. The starting amount of HfC powder before centrifugation was 15 grams dispersed in about 500 mL of IPA. After the second round of centrifugation, the powder was dried using a rotary evaporator and weighed. The weight of the powder collected after the second round of centrifugation was about 0.6 grams. There was a significant loss of HfC powder after the phase separation experiments. The SPS experiments required 15 grams of powder to create a 100HfC

sintered sample. This means that ~25 rounds of phase separation experiments would be required to produce enough powder for one sample of 100HfC.

Based on these findings, future experiments will look into the synthesis or purchasing of finer HfC powder for the development of TaC, HfC, and TaC-HfC blends for oxyacetylene torch testing.

3.6.2 Preliminary Oxyacetylene Torch Tests

Several preliminary oxyacetylene torch tests were conducted in efforts of identifying the ideal testing parameters and sample set-up. The goal of the initial experiments was to identify at what position from the torch and after how long would the sample reach a temperature of 2800°C. This was set as the target temperature before running the oxyacetylene torch tests and was selected based on previous oxidation experiments done on TaC and HfC. The experimental plan was to begin the torch tests at a distance of 4 cm from the torch tip and then move in increments of 0.5 cm closer to the torch tip, while waiting for the temperature to saturate on the surface of the sample at each distance. The gas flow rates were 8 slpm for acetylene and 10.81 slpm for oxygen. The fuel to oxidizer ratio was 0.74. The surface temperature and emissivity values of the samples were measured using a Teledyne FLIR one-color pyrometer (FLIR A300 series with FLIR ResearchIR software; T: -15-3000°C) and a Pyrofiber® Lab Automatic Emissivity Measurement System (AEMS) one-color pyrometer with laser pulse (Pyrofiber Lab System, Pyrometer LLC; T: 850-3000°C).

The first sample that was tested under the oxyacetylene torch was 100TaC. The 100TaC was attached to a graphite rod sample holder using a graphite adhesive. Once the sample was positioned on the graphite sample holder the graphite adhesive was cured for 10 hours at 120°C in a large box furnace. After curing the sample was taken to the oxyacetylene torch and mounted

for testing. The sample was mounted at a 90° angle relative to the torch tip, and the sample was swung into the lit torch (0°) via a rotary motor to begin the oxidation test. The starting distance was 4 cm from the torch tip. As stated above, the initial goal of the experiment was to try to reach a temperature of 2800°C by waiting for saturation at each distance from the torch tip and moving closer in 0.5 cm increments. During this first run, the 100TaC sample lasted 2 minutes and 7 seconds in front of the torch before spalling off the graphite sample holder. Pyrometer data revealed a maximum temperature achieved of 2600°C. The surface oxidation of the 100TaC sample is shown in Figure 34.

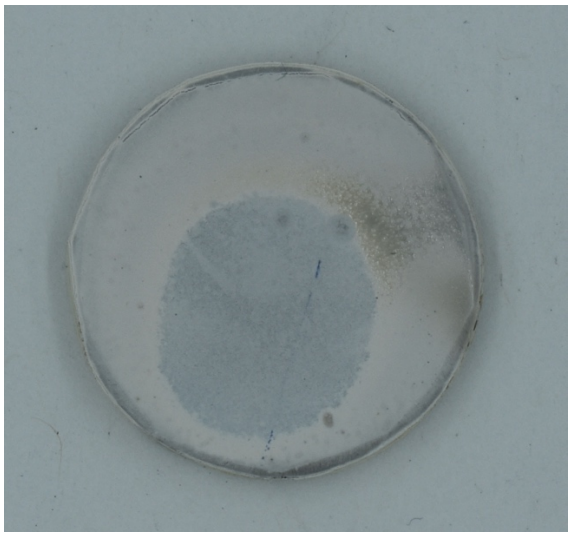

Figure 34 Optical micrograph of the 20-mm 100TaC sample oxyacetylene torch tested for 2 min and 7 sec at 4 cm from the torch tip.

In efforts of trying to achieve the target temperature of 2800°C, the next two 100TaC samples were oxyacetylene torch tested at a distance closer to the torch tip. The next two runs were conducted at a distance of 3 cm from the torch tip. The second 100TaC sample was mounted in the same manner as the first 100TaC, where the sample was mounted at a 90° angle relative to the torch tip and was swung into the lit torch (0°) via a rotary motor to begin the

oxidation test. The sample lasted about 56 seconds in front of the torch before exploding and breaking of the sample holder in 3 pieces, as shown in Figure 35a. The third 100Tac sample was also oxyacetylene torch tested at a distance of 3 cm from the torch tip. Similar to the second sample, this sample exploded and broke off the sample holder in 3 pieces after 10 seconds of being exposed to the torch (Figure 35b).

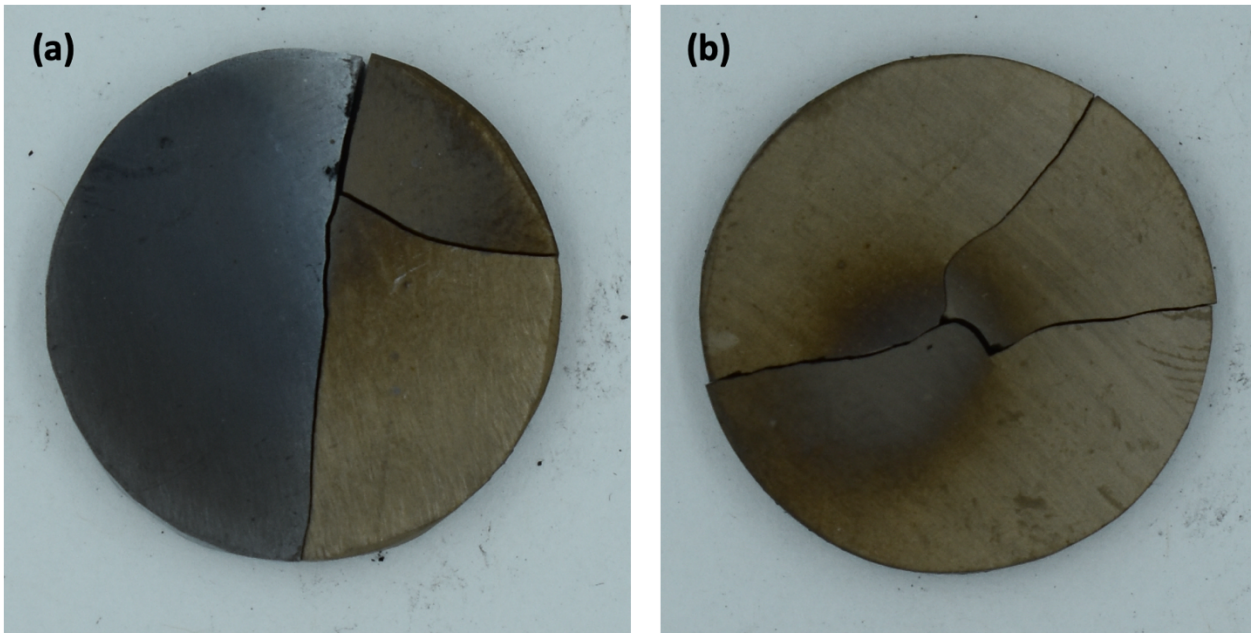

Figure 35 Optical micrographs of the 20-mm 100TaC sample oxyacetylene torch tested for (a) 56 seconds and (b) 10 sec at 3 cm from the torch tip.

These preliminary torch tests revealed an issue of mismatch between the thermal expansion of the sample (TaC) and the sample holder (graphite). Supplemental oxyacetylene torch experiments revealed that increasing the distances (6-10 cm) from the torch tip to reduce thermal shock did not allow for the sample surface to reach high enough temperatures for proper oxidation testing and analysis of these materials. The goal is to simulate temperature environments similar to the ones these materials will experience in high-speed flight. In order to

obtain valuable data and information to assess the feasibility of these materials for these applications, the torch tests must reflect temperatures closer to those seen in high-speed flight.

These results sparked the design of the vacuum sample holder that was used for the oxyacetylene torch experiments of the TaC-HfC samples discussed in the Results and Discussion section above. This eliminated the thermal shock that was occurring with the original graphite sample holder. The results of the preliminary torch tests also shifted the driving target to be heat flux instead of temperature. A heat flux of 400 W/cm^2 was selected and measured using a Gardon gauge (TG-1000-52, Vatell Corporation). The heat flux dictated the distance of the sample from the torch tip. These preliminary experiments were critical in identifying optimal torch testing parameters. The changes to the oxyacetylene torch tests described here allowed us to obtain the results outlined in the Results and Discussion section above.

3.7 Future Work

The results from the oxyacetylene torch tests on the 100TaC, 80TaC-20HfC, and 50TaC-50HfC samples provided a good starting point to begin to understand the improved oxidation resistance of the TaC-HfC solid solutions. Future experiments will aim to improve the density of the 20TaC-80HfC and 100HfC samples by purchasing starting HfC powders with smaller particle sizes for ball milling and sintering. The goal is to obtain relatively high densities (>95%) on these compositions to be able to conduct oxyacetylene torch tests with the same conditions as the first three compositions (100TaC, 80TaC-20HfC, and 50TaC-50HfC). This will provide a comprehensive analysis on the oxidation resistance of TaC-HfC solid solutions with respect to HfC content.

Acknowledgements

Chapter 3, in full, is a reprint of the material as it appears in Advanced Engineering Materials 2023. Sanchez, Maritza; Acord, Katherine, A.; Frueh, Samuel; Rueschhoff, Lisa, M.; Graeve, Olivia, A.; Wiley, 2023. The dissertation author was the primary investigator and author of this paper.

This project was supported by grant #FA9550-21-1-0061 from the Air Force Office of Scientific Research (AFOSR). MS gratefully acknowledges financial support through an INTERN supplement on award #1911372 from the National Science Foundation. LMR and KAA gratefully acknowledge financial support from the National Research Council Research Associateship Program and AFOSR Laboratory Research Initiation Request (21RXCOR032, PM: Dr. Ming-Jen Pan). The authors are grateful to Connor Wyckoff for acquiring hardness data. Any views expressed here are those of the authors' and do not reflect the official policy or position of the US Air Force, Department of Defense, or the US Government. Distribution A; cleared for public release (AFRL-2023-0723).

Chapter 4 REFERENCES

[1] W. E. Mahmoud, F. Al-Hazmi, F. Al-Noaiser, A. A. Al-Ghamdi, and L. M. Bronstein, "A facile method to syntheses monodisperse γ-Fe2O 3 nanocubes with high magnetic anisotropy density," *Superlattices Microstruct.*, vol. 68, pp. 1–5, 2014, doi: 10.1016/j.spmi.2014.01.009.

[2] G. Gao *et al.*, "Shape-controlled synthesis and magnetic properties of monodisperse Fe 3O4 nanocubes," *Cryst. Growth Des.*, vol. 10, no. 7, pp. 2888–2894, 2010, doi: 10.1021/cg900920q.

[3] K. Tsukiyama, M. Takasaki, Y. Oaki, and H. Imai, "Evolution of Co3O4 Nanocubes through Stepwise Oriented Attachment," *Langmuir*, vol. 35, no. 24, pp. 8025–8030, 2019, doi: 10.1021/acs.langmuir.9b00342.

[4] J. Muro-Cruces *et al.*, "Precise Size Control of the Growth of Fe3O4 Nanocubes over a Wide Size Range Using a Rationally Designed One-Pot Synthesis," *ACS Nano*, 2019, doi: 10.1021/acsnano.9b01281.

[5] H. Yang, T. Ogawa, D. Hasegawa, and M. Takahashi, "Synthesis and magnetic properties of monodisperse magnetite nanocubes," *J. Appl. Phys.*, vol. 103, no. 7, pp. 4–7, 2008, doi: 10.1063/1.2833820.

[6] Q. Song and Z. J. Zhang, "Shape Control and Associated Magnetic Properties of Spinel Cobalt Ferrite Nanocrystals," *J. Am. Chem. Soc.*, vol. 126, no. 19, pp. 6164–6168, 2004, doi: 10.1021/ja049931r.

[7] H. Itasaka, K. I. Mimura, K. Yasui, K. Hamamoto, and K. Kato, "Effect of heat treatment on internal stress in barium titanate nanocube assemblies and their dielectric property," *AIP Adv.*, vol. 11, no. 2, 2021, doi: 10.1063/5.0040765.

[8] S. Suehiro, T. Kimura, M. Tanaka, S. Takahashi, K. I. Mimura, and K. Kato, "Electrospray Deposition of {200} Oriented Regular-Assembly BaTiO 3 Nanocrystal Films under an Electric Field," *Langmuir*, 2019, doi: 10.1021/acs.langmuir.8b03813.

[9] K. I. Mimura and K. Kato, "Fabrication and electrical properties of barium titanate based solid solution nanocube assembly films," *Jpn. J. Appl. Phys.*, vol. 55, no. 10, 2016, doi: 10.7567/JJAP.55.10TA05.

[10] D. Chu, X. Lin, A. Younis, C. M. Li, F. Dang, and S. Li, "Growth and self-assembly of BaTiO3 nanocubes for resistive switching memory cells," *J. Solid State Chem.*, vol. 214, pp. 38–41, 2014, doi: 10.1016/j.jssc.2013.10.049.

[11] D. Caruntu, T. Rostamzadeh, T. Costanzo, S. Salemizadeh Parizi, and G. Caruntu, "Solvothermal synthesis and controlled self-assembly of monodisperse titanium-based

perovskite colloidal nanocrystals," *Nanoscale*, vol. 7, no. 30, pp. 12955–12969, 2015, doi: 10.1039/c5nr00737b.

[12] K. Kato *et al.*, "BaTiO3 nanocube and assembly to ferroelectric supracrystals," *J. Mater. Res.*, vol. 28, no. 21, pp. 2932–2945, 2013, doi: 10.1557/jmr.2013.299.

[13] K. I. Mimura and K. Kato, "Fabrication and characterization of barium titanate nanocube ordered assemblies on micro-patterned substrates," *J. Ceram. Soc. Japan*, vol. 123, no. 1439, pp. 579–582, 2015, doi: 10.2109/jcersj2.123.579.

[14] K. I. Mimura and K. Kato, "Fabrication and piezoresponse properties of {100} BaTiO3 films containing highly ordered nanocube assemblies on various substrates," *J. Nanoparticle Res.*, vol. 15, no. 10, 2013, doi: 10.1007/s11051-013-1995-5.

[15] M. Kuwabara, "Innovative nanocrystal-based technologies for ceramic devices with novel electronic functions," *J. Adv. Ceram.*, vol. 1, no. 2, pp. 79–88, 2012, doi: 10.1007/s40145-012-0016-y.

[16] K. I. Mimura and K. Kato, "Dielectric properties of barium titanate nanocube ordered assembly sintered at various temperatures," *Jpn. J. Appl. Phys.*, vol. 53, no. 9, 2014, doi: 10.7567/JJAP.53.09PA03.

[17] K. I. Mimura and K. Kato, "Enhanced dielectric properties of BaTiO3 nanocube assembled film in metal-insulator-metal capacitor structure," *Appl. Phys. Express*, vol. 7, no. 6, 2014, doi: 10.7567/APEX.7.061501.

[18] K. I. Mimura *et al.*, "Characterization of dielectric nanocubes ordered structures fabricated by solution self-assembly process," *Jpn. J. Appl. Phys.*, vol. 50, no. 9 PART 3, 2011, doi: 10.1143/JJAP.50.09NC09.

[19] K. I. Mimura, K. Kato, H. Imai, S. Wada, H. Haneda, and M. Kuwabara, "Fabrication and characterization of dielectric nanocube self-assembled structures," *Jpn. J. Appl. Phys.*, vol. 51, no. 9 PART 2, 2012, doi: 10.1143/JJAP.51.09LC03.

[20] T. Sreethawong, S. Ngamsinlapasathian, and S. Yoshikawa, "Surfactant-aided sol-gel synthesis of mesoporous-assembled TiO2-NiO mixed oxide nanocrystals and their photocatalytic azo dye degradation activity," *Chem. Eng. J.*, vol. 192, pp. 292–300, 2012, doi: 10.1016/j.cej.2012.04.006.

[21] M. El-Kemary, N. Nagy, and I. El-Mehasseb, "Nickel oxide nanoparticles: Synthesis and spectral studies of interactions with glucose," *Mater. Sci. Semicond. Process.*, vol. 16, no. 6, pp. 1747–1752, 2013, doi: 10.1016/j.mssp.2013.05.018.

[22] P. Poizot, S. Laruelle, S. Grugeon, L. Dupont, and J. Tarascon, "Nano-sized transition-metaloxidesas," *Nature*, vol. 407, no. September, 2000.

[23] S. H. Park, S. H. Kang, C. S. Johnson, K. Amine, and M. M. Thackeray, “Lithium-manganese-nickel-oxide electrodes with integrated layered-spinel structures for lithium batteries,” *Electrochem. commun.*, vol. 9, no. 2, pp. 262–268, 2007, doi: 10.1016/j.elecom.2006.09.014.

[24] I. Hotovy, J. Huran, L. Spiess, S. Hascik, and V. Rehacek, “Preparation of nickel oxide thin films for gas sensors applications,” *Sensors Actuators, B Chem.*, vol. 57, no. 1–3, pp. 147–152, 1999, doi: 10.1016/S0925-4005(99)00077-5.

[25] K. C. Liu and M. A. Anderson, “Porous nickel oxide films for electrochemical capacitors,” *Mater. Res. Soc. Symp. - Proc.*, vol. 393, pp. 427–432, 1995, doi: 10.1557/proc-393-427.

[26] E. Avendaño, L. Berggren, G. A. Niklasson, C. G. Granqvist, and A. Azens, “Electrochromic materials and devices: Brief survey and new data on optical absorption in tungsten oxide and nickel oxide films,” *Thin Solid Films*, vol. 496, no. 1, pp. 30–36, 2006, doi: 10.1016/j.tsf.2005.08.183.

[27] D. S. Dalavi, R. S. Devan, R. S. Patil, Y. R. Ma, and P. S. Patil, “Electrochromic performance of sol-gel deposited NiO thin film,” *Mater. Lett.*, vol. 90, pp. 60–63, 2013, doi: 10.1016/j.matlet.2012.08.108.

[28] G. Mattei, P. Mazzoldi, M. L. Post, D. Buso, M. Guglielmi, and A. Martucci, “Cookie-like Au/NiO nanoparticles with optical gas-sensing properties,” *Adv. Mater.*, vol. 19, no. 4, pp. 561–564, 2007, doi: 10.1002/adma.200600930.

[29] B. Sasi and K. G. Gopchandran, “Nanostructured mesoporous nickel oxide thin films,” *Nanotechnology*, vol. 18, no. 11, 2007, doi: 10.1088/0957-4484/18/11/115613.

[30] T. Lin, X. Li, and J. Jang, “High performance p-type NiOx thin-film transistor by Sn doping,” *Appl. Phys. Lett.*, vol. 108, no. 23, 2016, doi: 10.1063/1.4953222.

[31] S. Hüfner, “Electronic structure of NiO and related 3d-transition-metal compounds,” *Adv. Phys.*, vol. 43, no. 2, pp. 183–356, 1994, doi: 10.1080/00018739400101495.

[32] D. Zhang, S. Nozaki, and K. Uchida, “NiO/Si heterostructures formed by UV oxidation of nickel deposited on Si substrates,” *J. Vac. Sci. Technol. B, Nanotechnol. Microelectron. Mater. Process. Meas. Phenom.*, vol. 32, no. 3, p. 031202, 2014, doi: 10.1116/1.4868634.

[33] G. Bai *et al.*, “The microemulsion preparation and high catalytic performance of mesoporous NiO nanorods and nanocubes for toluene combustion,” *Chem. Eng. J.*, vol. 219, pp. 200–208, 2013, doi: 10.1016/j.cej.2013.01.008.

[34] J. R. C. Mateo, A. L. Salut, and M. C. Marquez, “Surfactant assisted sol-gel synthesis of nickel oxide nanostructures,” *Mater. Sci. Forum*, vol. 916 MSF, pp. 74–78, 2018, doi: 10.4028/www.scientific.net/MSF.916.74.

[35] D. Mateos *et al.*, “Synthesis of high purity nickel oxide by a modified sol-gel method,” *Ceram. Int.*, vol. 45, no. 9, pp. 11403–11407, 2019, doi: 10.1016/j.ceramint.2019.03.005.

[36] P. A. Sheena, K. P. Priyanka, N. Aloysius Sabu, S. Ganesh, and T. Varghese, “Effect of electron beam irradiation on the structure and optical properties of nickel oxide nanocubes,” *Bull. Mater. Sci.*, vol. 38, no. 4, pp. 825–830, 2015, doi: 10.1007/s12034-015-0953-5.

[37] C. Tabor, R. Narayanan, and M. A. El-Sayed, “Catalysis with transition metal nanoparticles in colloidal solution: Heterogeneous or homogeneous?,” *Model Syst. Catal. Single Cryst. to Support. Enzym. Mimics*, pp. 395–414, 2010, doi: 10.1007/978-0-387-98049-2_18.

[38] X. Xiao, Q. Luan, X. Yao, and K. Zhou, “Single-crystal CeO2 nanocubes used for the direct electron transfer and electrocatalysis of horseradish peroxidase,” *Biosens. Bioelectron.*, vol. 24, no. 8, pp. 2447–2451, 2009, doi: 10.1016/j.bios.2008.12.020.

[39] M. Alhumaimess, O. Aldosari, H. Alshammari, M. M. Kamel, M. A. Betiha, and H. M. A. Hassan, “Ionic liquid green synthesis of CeO 2 nanorods and nano-cubes: Investigation of the shape dependent on catalytic performance,” *J. Mol. Liq.*, vol. 279, pp. 649–656, 2019, doi: 10.1016/j.molliq.2019.02.014.

[40] M. Piumetti *et al.*, “Nanostructured ceria-based materials: Effect of the hydrothermal synthesis conditions on the structural properties and catalytic activity,” *Catalysts*, vol. 7, no. 6, 2017, doi: 10.3390/catal7060174.

[41] M. P. Chavhan, S. Som, and C. H. Lu, “Size-controlled ceria nanocubes obtained via hydrothermal route for electrochemical capacitors,” *Mater. Lett.*, vol. 257, p. 126598, 2019, doi: 10.1016/j.matlet.2019.126598.

[42] Y. Zhang, F. Yang, R. Gao, and W. L. Dai, “Manganese-doped CeO 2 nanocubes as highly efficient catalysts for styrene epoxidation with TBHP,” *Appl. Surf. Sci.*, vol. 471, no. September 2018, pp. 767–775, 2019, doi: 10.1016/j.apsusc.2018.11.246.

[43] H. He *et al.*, “Controllable synthesis, characterization, and CO oxidation activity of CeO2 nanostructures with various morphologies,” *Ceram. Int.*, vol. 42, no. 6, pp. 7810–7818, 2016, doi: 10.1016/j.ceramint.2016.02.005.

[44] H. X. Mai *et al.*, “Shape-selective synthesis and oxygen storage behavior of ceria nanopolyhedra, nanorods, and nanocubes,” *J. Phys. Chem. B*, vol. 109, no. 51, pp. 24380–24385, 2005, doi: 10.1021/jp055584b.

[45] N. K. Renuka, T. Divya, and T. Jency Mohan, “A facile route to ceria nanocubes,” *Mater. Lett.*, vol. 141, pp. 107–109, 2015, doi: 10.1016/j.matlet.2014.11.075.

[46] K. Huang *et al.*, “One-step synthesis of reduced graphene oxide-CeO2 nanocubes composites with enhanced photocatalytic activity,” *Mater. Lett.*, vol. 124, pp. 223–226, 2014, doi: 10.1016/j.matlet.2014.03.023.

[47] A. Arshad *et al.*, “In situ synthesis of highly populated CeO2 nanocubes grown on carbon nanotubes as a synergy hybrid and its electrocatalytic potential,” *J. Mater. Res. Technol.*, vol. 8, no. 6, pp. 5336–5343, 2019, doi: 10.1016/j.jmrt.2019.08.054.

[48] S. Farhang-Sahlevani *et al.*, “A facile hydrothermal synthesis of CeO2 nanocubes decorated ZnO nanostructures: optical and enhanced photocatalytic properties,” *J. Mater. Sci. Mater. Electron.*, vol. 30, no. 12, pp. 11643–11651, 2019, doi: 10.1007/s10854-019-01521-8.

[49] T. J. Fisher, M. Wang, Y. Ibrahim, B. Steffensmeier, and C. L. Cheung, “Effect of sodium nitrate on microwave-assisted synthesis of ceria nanocubes,” *Mater. Lett.*, vol. 178, pp. 71–74, 2016, doi: 10.1016/j.matlet.2016.04.186.

[50] Y. Tao, F. H. Gong, H. Wang, H. P. Wu, and G. L. Tao, “Microwave-assisted preparation of cerium dioxide nanocubes,” *Mater. Chem. Phys.*, vol. 112, no. 3, pp. 973–976, 2008, doi: 10.1016/j.matchemphys.2008.07.018.

[51] U. Castanet *et al.*, “Controlling the {111}/{110} Surface Ratio of Cuboidal Ceria Nanoparticles,” *ACS Appl. Mater. Interfaces*, vol. 11, no. 12, pp. 11384–11390, 2019, doi: 10.1021/acsami.8b21667.

[52] X. Han, L. Li, and C. Wang, “Template-free synthesis of uniform single-crystal hollow cerium dioxide nanocubes and their catalytic activity,” *Nanoscale*, vol. 5, no. 16, pp. 7193–7196, 2013, doi: 10.1039/c3nr01948a.

[53] K. Deori, C. Kalita, and S. Deka, “(100) surface-exposed CeO2 nanocubes as an efficient heterogeneous catalyst in the tandem oxidation of benzyl alcohol, para-chlorobenzyl alcohol and toluene to the corresponding aldehydes selectively,” *J. Mater. Chem. A*, vol. 3, no. 13, pp. 6909–6920, 2015, doi: 10.1039/c4ta06547f.

[54] Q. Wu *et al.*, “Great influence of anions for controllable synthesis of CeO2 nanostruetures: From nanorods to nanocubes,” *J. Phys. Chem. C*, vol. 112, no. 44, pp. 17076–17080, 2008, doi: 10.1021/jp804140e.

[55] O. Mendiuk, M. Nawrocki, and L. Kepinski, “The synthesis of Ce1-xLnxO2-y (Ln=Pr, Sm, Gd, Tb) nanocubes by hydrothermal methods,” *Ceram. Int.*, vol. 42, no. 1, pp. 1998–2012, 2016, doi: 10.1016/j.ceramint.2015.10.006.

[56] F. Dang *et al.*, “In situ growth BaTiO 3 nanocubes and their superlattice from an aqueous process,” *Nanoscale*, vol. 4, no. 4, pp. 1344–1349, 2012, doi: 10.1039/c2nr11594h.

[57] Q. Ma and K. Kato, “Crystallographic fusion behavior and interface evolution of mono-

layer BaTiO3 nanocube arrangement," *CrystEngComm*, vol. 18, no. 9, pp. 1543–1549, 2016, doi: 10.1039/c5ce02235e.

[58] Q. Liu, Z. Yan, G. Sun, and W. Zheng, "Solvothermal preparation and characterization of barium titanate nanocubes," *Chem. Lett.*, vol. 36, no. 3, pp. 458–459, 2007, doi: 10.1246/cl.2007.458.

[59] K. C. Huango, T. C. Huango, and W. F. Hsieh, "Morphology-controlled synthesis of barium titanate nanostructures," *Inorg. Chem.*, vol. 48, no. 19, pp. 9180–9184, 2009, doi: 10.1021/ic900854x.

[60] J. Yang, B. Geng, Y. Ye, and X. Yu, "Stick-like titania precursor route to MTiO 3 (M = Sr, Ba, and Ca) polyhedra," *CrystEngComm*, vol. 14, no. 8, pp. 2959–2965, 2012, doi: 10.1039/c2ce06532k.

[61] A. E. Souza *et al.*, "Photoluminescence of SrTiO 3: Influence of particle size and morphology," *Cryst. Growth Des.*, vol. 12, no. 11, pp. 5671–5679, 2012, doi: 10.1021/cg301168k.

[62] M. Borah and D. Mohanta, "Composite-hydroxide-mediated formation of barium titanate nanocubes and their optical emission response," *Chinese J. Phys.*, vol. 53, no. 1, pp. 1–11, 2015, doi: 10.6122/CJP.20140804C.

[63] J. Miao, C. Hu, H. Liu, and Y. Xiong, "BaTiO3 nanocubes: Size-selective formation and structure analysis," *Mater. Lett.*, vol. 62, no. 2, pp. 235–238, 2008, doi: 10.1016/j.matlet.2007.05.009.

[64] H. Liu, C. Hu, and Z. L. Wang, "Composite-hydroxide-mediated approach for the synthesis of nanostructures of complex functional-oxides," *Nano Lett.*, vol. 6, no. 7, pp. 1535–1540, 2006, doi: 10.1021/nl061253e.

[65] T. Tsumura, K. Matsuoka, and M. Toyoda, "Formation and annealing of BaTiO3 and SrTiO3 nanoparticles in KOH solution," *J. Mater. Sci. Technol.*, vol. 26, no. 1, pp. 33–38, 2010, doi: 10.1016/S1005-0302(10)60005-9.

[66] T. Kimijima, K. Kanie, M. Nakaya, and A. Muramatsu, "Solvothermal synthesis of shape-controlled perovskite MTiO3 (M = Ba, Sr, and Ca) Particles in H2O/polyols mixed solutions," *Mater. Trans.*, vol. 55, no. 1, pp. 147–153, 2014, doi: 10.2320/matertrans.M2013350.

[67] Q. Ma, K. I. Mimura, and K. Kato, "Diversity in size of barium titanate nanocubes synthesized by a hydrothermal method using an aqueous Ti compound," *CrystEngComm*, vol. 16, no. 36, pp. 8398–8405, 2014, doi: 10.1039/c4ce01195c.

[68] K. I. Mimura and K. Kato, "Characteristics of barium titanate nanocube ordered assembly thin films fabricated by dip-coating method," *Jpn. J. Appl. Phys.*, vol. 52, no. 9 PART2,

2013, doi: 10.7567/JJAP.52.09KC06.

[69] S. S. Parizi, A. Mellinger, and G. Caruntu, “Ferroelectric barium titanate nanocubes as capacitive building blocks for energy storage applications,” *ACS Appl. Mater. Interfaces*, vol. 6, no. 20, pp. 17506–17517, 2014, doi: 10.1021/am502547h.

[70] Q. Ma and K. Kato, “Nucleation and Growth Mechanism of Barium Titanate Nanoblocks in Hydrothermal Process Using Aqueous Titanium Compound,” *Cryst. Growth Des.*, vol. 17, no. 5, pp. 2507–2512, 2017, doi: 10.1021/acs.cgd.7b00025.

[71] H. Zhan *et al.*, “Multiple nucleation and crystal growth of barium titanate,” *Cryst. Growth Des.*, vol. 12, no. 3, pp. 1247–1253, 2012, doi: 10.1021/cg201259u.

[72] M. Abbas *et al.*, “Size-controlled high magnetization CoFe2O4 nanospheres and nanocubes using rapid one-pot sonochemical technique,” *Ceram. Int.*, vol. 40, no. 2, pp. 3269–3276, 2014, doi: 10.1016/j.ceramint.2013.09.109.

[73] Y. Xu, J. Sherwood, Y. Qin, R. A. Holler, and Y. Bao, “A general approach to the synthesis and detailed characterization of magnetic ferrite nanocubes,” *Nanoscale*, vol. 7, no. 29, pp. 12641–12649, 2015, doi: 10.1039/c5nr03096j.

[74] M. Ravichandran and S. Velumani, “Manganese ferrite nanocubes as an MRI contrast agent,” *Mater. Res. Express*, vol. 7, no. 1, pp. 0–8, 2020, doi: 10.1088/2053-1591/ab66a4.

[75] J. Hao *et al.*, “In situ controllable growth of CoFe2O4 ferrite nanocubes on graphene for colorimetric detection of hydrogen peroxide,” *J. Mater. Chem. A*, vol. 1, no. 13, pp. 4352–4357, 2013, doi: 10.1039/c3ta00774j.

[76] X. Zhang *et al.*, “NiFe2O4 nanocubes anchored on reduced graphene oxide cryogel to achieve a 1.8 V flexible solid-state symmetric supercapacitor,” *Chem. Eng. J.*, vol. 360, no. October 2018, pp. 171–179, 2019, doi: 10.1016/j.cej.2018.11.206.

[77] Z. P. Chen, W. Q. Fang, B. Zhang, and H. G. Yang, “High-yield synthesis and magnetic properties of ZnFe2O 4 single crystal nanocubes in aqueous solution,” *J. Alloys Compd.*, vol. 550, pp. 348–352, 2013, doi: 10.1016/j.jallcom.2012.10.105.

[78] A. Sathya *et al.*, “CoxFe3-xO4 Nanocubes for Theranostic Applications: Effect of Cobalt Content and Particle Size,” *Chem. Mater.*, vol. 28, no. 6, pp. 1769–1780, 2016, doi: 10.1021/acs.chemmater.5b04780.

[79] J. F. and H. C. Zeng, “Size-Controlled Growth of Co3O4 Nanocubes,” *Am. Chem. Soc.*, doi: 10.1021/cm020940d.

[80] W. E. M. Elsayed, F. S. Al-Hazmi, L. S. Memesh, and L. M. Bronstein, “A novel approach for rapid green synthesis of nearly mono-disperse iron oxide magnetic nanocubes with remarkable surface magnetic anisotropy density for enhancing

hyperthermia performance," *Colloids Surfaces A Physicochem. Eng. Asp.*, vol. 529, no. May, pp. 239–245, 2017, doi: 10.1016/j.colsurfa.2017.06.008.

[81] X. Wei *et al.*, "A novel functional material of Co3O4/Fe2O3 nanocubes derived from a MOF precursor for high-performance electrochemical energy storage and conversion application," *Chem. Eng. J.*, vol. 355, no. June 2018, pp. 336–340, 2019, doi: 10.1016/j.cej.2018.08.009.

[82] S. F. Situ-Loewenstein *et al.*, "A novel synthetic route for high-index faceted iron oxide concave nanocubes with high T2 relaxivity for in vivo MRI applications," *J. Mater. Sci. Mater. Med.*, vol. 29, no. 5, 2018, doi: 10.1007/s10856-018-6052-6.

[83] X. Liu, G. Qiu, and X. Li, "Shape-controlled synthesis and properties of uniform spinel cobalt oxide nanocubes," *Nanotechnology*, vol. 16, no. 12, pp. 3035–3040, 2005, doi: 10.1088/0957-4484/16/12/051.

[84] E. Wetterskog *et al.*, "Precise control over shape and size of iron oxide nanocrystals suitable for assembly into ordered particle arrays," *Sci. Technol. Adv. Mater.*, vol. 15, no. 5, 2014, doi: 10.1088/1468-6996/15/5/055010.

[85] W. K. Ham, G. F. Holland, and A. M. Stacy, "Low-Temperature Synthesis of Superconducting La^M,Cu04: Direct Precipitation from NaOH/KOH Melts," vol. X, no. 6, pp. 5214–5215, 1988.

[86] K. Fujinami, K. Katagiri, J. Kamiya, T. Hamanaka, and K. Koumoto, "Sub-10 nm strontium titanate nanocubes highly dispersed in non-polar organic solvents," *Nanoscale*, vol. 2, no. 10, pp. 2080–2083, 2010, doi: 10.1039/c0nr00543f.

[87] Z. Sun *et al.*, "Experimental and simulation-based understanding of morphology controlled barium titanate nanoparticles under co-adsorption of surfactants," *CrystEngComm*, vol. 19, no. 24, pp. 3288–3298, 2017, doi: 10.1039/c7ce00279c.

[88] K. Huang, L. Yuan, and S. Feng, "Crystal facet tailoring arts in perovskite oxides," *Inorg. Chem. Front.*, vol. 2, no. 11, pp. 965–981, 2015, doi: 10.1039/c5qi00168d.

[89] S. G. Cho, P. F. Johnson, and R. A. Condrate, "Thermal decomposition of (Sr, Ti) organic precursors during the Pechini process," *J. Mater. Sci.*, vol. 25, no. 11, pp. 4738–4744, 1990, doi: 10.1007/BF01129934.

[90] X. H. Zuo *et al.*, "A novel method for preparation of barium strontium titanate nanopowders," *Mater. Lett.*, vol. 64, no. 10, pp. 1150–1153, 2010, doi: 10.1016/j.matlet.2010.02.034.

[91] B. L. Newalkar, S. Komarneni, and H. Katsuki, "Microwave-hydrothermal synthesis and characterization of barium titanate powders," *Mater. Res. Bull.*, vol. 36, no. 13–14, pp. 2347–2355, 2001, doi: 10.1016/S0025-5408(01)00729-2.

[92] M. E. Ebrahimi, M. Allahverdi, and A. Safari, “Synthesis of high aspect ratio platelet SrTiO 3,” *J. Am. Ceram. Soc.*, vol. 88, no. 8, pp. 2129–2132, 2005, doi: 10.1111/j.1551-2916.2005.00427.x.

[93] W. M. Haynes, *CRC Handbook of Chemistry and Physics*, 95th ed. 1942.

[94] R. E. Eckert, J.O., Hung-Houston, C.C., Gersten, B.L., Lencka, M.M., Riman, “Kinetics and Mechanisms of Hydrothermal Synthesis of Barium Titanate,” *Angew. Chemie Int. Ed. 6(11), 951–952.*, pp. 2013–2015, 2021.

[95] H. Xu and L. Gao, “New evidence of a dissolution-precipitation mechanism in hydrothermal synthesis of barium titanate powders,” *Mater. Lett.*, vol. 57, no. 2, pp. 490–494, 2002, doi: 10.1016/S0167-577X(02)00817-0.

[96] J. Binner *et al.*, “Selection, processing, properties and applications of ultra-high temperature ceramic matrix composites, UHTCMCs–a review,” *Int. Mater. Rev.*, vol. 65, no. 7, pp. 389–444, 2020, doi: 10.1080/09506608.2019.1652006.

[97] W. G. Fahrenholtz and G. E. Hilmas, “Ultra-high temperature ceramics: Materials for extreme environments,” *Scr. Mater.*, vol. 129, pp. 94–99, 2017, doi: 10.1016/j.scriptamat.2016.10.018.

[98] A. Nisar, C. Zhang, B. Boesl, and A. Agarwal, “A perspective on challenges and opportunities in developing high entropy-ultra high temperature ceramics,” *Ceram. Int.*, vol. 46, no. 16, pp. 25845–25853, 2020, doi: 10.1016/j.ceramint.2020.07.066.

[99] M. M. Opeka, I. G. Talmy, and J. A. Zaykoski, “Oxidation-based materials selection for 2000°C + hypersonic aerosurfaces: Theoretical considerations and historical experience,” *J. Mater. Sci.*, vol. 39, no. 19, pp. 5887–5904, 2004, doi: 10.1023/B:JMSC.0000041686.21788.77.

[100] J. T. Cahill and O. A. Graeve, “Hexaborides: A review of structure, synthesis and processing,” *J. Mater. Res. Technol.*, vol. 8, no. 6, pp. 6321–6335, 2019, doi: 10.1016/j.jmrt.2019.09.041.

[101] R. Kanakala, G. Rojas-George, and O. A. Graeve, “Unique preparation of hexaboride nanocubes: A first example of boride formation by combustion synthesis,” *J. Am. Ceram. Soc.*, vol. 93, no. 10, pp. 3136–3141, 2010, doi: 10.1111/j.1551-2916.2010.03853.x.

[102] B. R. Golla, A. Mukhopadhyay, B. Basu, and S. K. Thimmappa, “Review on ultra-high temperature boride ceramics,” *Prog. Mater. Sci.*, vol. 111, no. February, p. 100651, 2020, doi: 10.1016/j.pmatsci.2020.100651.

[103] O. A. Graeve and Z. A. Munir, “Electric field enhanced synthesis of nanostructured tantalum carbide,” *J. Mater. Res.*, vol. 17, no. 3, pp. 609–613, 2002, doi: 10.1557/JMR.2002.0086.

[104] Y. Zhou, H. Xiang, Z. Feng, and Z. Li, “General Trends in Electronic Structure, Stability, Chemical Bonding and Mechanical Properties of Ultrahigh Temperature Ceramics TMB2 (TM=transition metal),” *J. Mater. Sci. Technol.*, vol. 31, no. 3, pp. 285–294, 2015, doi: 10.1016/j.jmst.2014.09.014.

[105] F. Monteverde and R. Savino, “Stability of ultra-high-temperature ZrB2-SiC ceramics under simulated atmospheric re-entry conditions,” *J. Eur. Ceram. Soc.*, vol. 27, no. 16, pp. 4797–4805, 2007, doi: 10.1016/j.jeurceramsoc.2007.02.201.

[106] F. Monteverde, “The thermal stability in air of hot-pressed diboride matrix composites for uses at ultra-high temperatures,” *Corros. Sci.*, vol. 47, no. 8, pp. 2020–2033, 2005, doi: 10.1016/j.corsci.2004.09.019.

[107] P. X. Zhang, L. Ye, F. H. Chen, W. J. Han, Y. H. Wu, and T. Zhao, “Stability, mechanical, and thermodynamic behaviors of (TiZrHfTaM)C (M = Nb, Mo, W, V, Cr) high-entropy carbide ceramics,” *J. Alloys Compd.*, vol. 903, 2022, doi: 10.1016/j.jallcom.2022.163868.

[108] E. Wuchina *et al.*, “Designing for ultrahigh-temperature applications: The mechanical and thermal properties of HfB2, HfCx, HfNx and αHf(N),” *J. Mater. Sci.*, vol. 39, no. 19, pp. 5939–5949, 2004, doi: 10.1023/B:JMSC.0000041690.06117.34.

[109] M. Gasch, S. Johnson, and J. Marschall, “Thermal conductivity characterization of hafnium diboride-based ultra-high-temperature ceramics,” *J. Am. Ceram. Soc.*, vol. 91, no. 5, pp. 1423–1432, 2008, doi: 10.1111/j.1551-2916.2008.02364.x.

[110] Y. P. Wang, G. Y. Gan, W. Wang, Y. Yang, and B. Y. Tang, “Ab Initio Prediction of Mechanical and Electronic Properties of Ultrahigh Temperature High-Entropy Ceramics (Hf0.2Zr0.2Ta0.2M0.2Ti0.2)B2 (M = Nb, Mo, Cr),” *Phys. Status Solidi Basic Res.*, vol. 255, no. 8, pp. 1–7, 2018, doi: 10.1002/pssb.201800011.

[111] Z. Y. Tan, X. Wu, W. Zhu, J. W. Guo, W. Wang, and Z. S. Ma, “Ultra-high hardness induced by W precipitation within Ta-Hf-W-C ultra-high temperature ceramic coatings,” *J. Eur. Ceram. Soc.*, vol. 42, no. 13, pp. 6288–6294, 2022, doi: 10.1016/j.jeurceramsoc.2022.05.069.

[112] X. J. Guo *et al.*, “High hardness (TiZr)C ceramic with dislocation networks,” *J. Am. Ceram. Soc.*, vol. 105, no. 9, pp. 5984–5993, 2022, doi: 10.1111/jace.18552.

[113] E. Castle, T. Csanádi, S. Grasso, J. Dusza, and M. Reece, “Processing and Properties of High-Entropy Ultra-High Temperature Carbides,” *Sci. Rep.*, vol. 8, no. 1, pp. 1–12, 2018, doi: 10.1038/s41598-018-26827-1.

[114] E. W. Neuman, G. E. Hilmas, and W. G. Fahrenholtz, “Transition metal diboride-silicon carbide-boron carbide ceramics with super-high hardness and strength,” *J. Eur. Ceram.*

Soc., vol. 42, no. 15, pp. 6795–6801, 2022, doi: 10.1016/j.jeurceramsoc.2022.08.019.

[115] O. Cedillos-Barraza *et al.*, "Investigating the highest melting temperature materials: A laser melting study of the TaC-HfC system," *Sci. Rep.*, vol. 6, 2016, doi: 10.1038/srep37962.

[116] T. Ren *et al.*, "Morphology Control of Tantalum Carbide Nanoparticles through Dopant Additions," *J. Phys. Chem. C*, vol. 125, no. 19, pp. 10665–10675, 2021, doi: 10.1021/acs.jpcc.1c01387.

[117] O. Cedillos-Barraza, S. Grasso, N. Al Nasiri, D. D. Jayaseelan, M. J. Reece, and W. E. Lee, "Sintering behaviour, solid solution formation and characterisation of TaC, HfC and TaC-HfC fabricated by spark plasma sintering," *J. Eur. Ceram. Soc.*, vol. 36, no. 7, pp. 1539–1548, 2016, doi: 10.1016/j.jeurceramsoc.2016.02.009.

[118] D. Demirskyi, H. Borodianska, T. Nishimura, T. S. Suzuki, K. Yoshimi, and O. Vasylkiv, "Deformation-resistant Ta0.2Hf0.8C solid-solution ceramic with superior flexural strength at 2000°C," *J. Am. Ceram. Soc.*, vol. 105, no. 1, pp. 512–524, 2022, doi: 10.1111/jace.18072.

[119] D. Demirskyi, H. Borodianska, T. S. Suzuki, Y. Sakka, K. Yoshimi, and O. Vasylkiv, "High-temperature flexural strength performance of ternary high-entropy carbide consolidated via spark plasma sintering of TaC, ZrC and NbC," *Scr. Mater.*, vol. 164, pp. 12–16, 2019, doi: 10.1016/j.scriptamat.2019.01.024.

[120] D. Demirskyi, O. Vasylkiv, and K. Yoshimi, "High-temperature deformation in bulk polycrystalline hafnium carbide consolidated using spark plasma sintering," *J. Eur. Ceram. Soc.*, vol. 41, no. 15, pp. 7442–7449, 2021, doi: 10.1016/j.jeurceramsoc.2021.08.038.

[121] B. Zhang *et al.*, "Low temperature densification mechanism and properties of Ta1-xHfxC solid solutions with decarbonization and phase transition of Cr3C2," *J. Mater.*, vol. 7, no. 4, pp. 672–682, 2021, doi: 10.1016/j.jmat.2020.12.001.

[122] K. A. Kane, B. A. Pint, D. Mitchell, and J. A. Haynes, "Oxidation of ultrahigh temperature ceramics: kinetics, mechanisms, and applications," *J. Eur. Ceram. Soc.*, vol. 41, no. 13, pp. 6130–6150, 2021, doi: 10.1016/j.jeurceramsoc.2021.05.055.

[123] A. Paul, J. G. P. Binner, B. Vaidhyanathan, A. C. J. Heaton, and P. M. Brown, "Oxyacetylene torch testing and microstructural characterization of tantalum carbide," *J. Microsc.*, vol. 250, no. 2, pp. 122–129, 2013, doi: 10.1111/jmi.12028.

[124] A. Lashtabeg, M. Smart, D. Riley, A. Gillen, and J. Drennan, "The effect of extreme temperature in an oxidising atmosphere on dense tantalum carbide (TaC)," *J. Mater. Sci.*, vol. 48, no. 1, pp. 258–264, 2013, doi: 10.1007/s10853-012-6740-4.

[125] C. B. Bargeron, R. C. Benson, R. W. Newman, A. N. Jette, and T. E. Phillips, “Oxidation mechanisms of hafnium carbide and hafnium diboride in the temperature range 1400 to 2100°C,” *Johns Hopkins APL Tech. Dig. (Applied Phys. Lab.*, vol. 14, no. 1, pp. 29–36, 1993.

[126] S. Shimada and F. Yunazar, “Oxidation of Hafnium Carbide and Titanium Carbide Single Crystals with the Formation of Carbon at High Temperatures and Low Oxygen Pressures,” *J. Am. Ceram. Soc.*, vol. 28, no. 189395, pp. 721–728, 2000.

[127] E. L. Courtright, J. T. Prater, G. R. Holcomb, G. R. S. Pierre, and R. A. Rapp, “Oxidation of hafnium carbide and hafnium carbide with additions of tantalum and praseodymium,” *Oxid. Met.*, vol. 36, no. 5–6, pp. 423–437, 1991, doi: 10.1007/BF01151590.

[128] C. Zhang, B. Boesl, and A. Agarwal, “Oxidation resistance of tantalum carbide-hafnium carbide solid solutions under the extreme conditions of a plasma jet,” *Ceram. Int.*, vol. 43, no. 17, pp. 14798–14806, 2017, doi: 10.1016/j.ceramint.2017.07.227.

[129] S. A. Ghaffari, M. A. Faghihi-Sani, F. Golestani-Fard, and S. Ebrahimi, “Pressureless sintering of Ta0.8Hf0.2C UHTC in the presence of MoSi2,” *Ceram. Int.*, vol. 39, no. 2, pp. 1985–1989, 2013, doi: 10.1016/j.ceramint.2012.08.050.

[130] J. P. Kelly, V. S. Vakharia, E. Novitskaya, and O. A. Graeve, “Densification and Fracture Responses of (Ta1−xWx)C–WC Composites,” *Adv. Eng. Mater.*, vol. 24, no. 8, pp. 1–9, 2022, doi: 10.1002/adem.202200026.

[131] J. T. Cahill, J. P. Kelly, E. Novitskaya, M. McKee, J. A. Bahena, and O. A. Graeve, “Suppressing η-phase development in steel-cemented tungsten carbide: A spark plasma sintering study,” *J. Am. Ceram. Soc.*, vol. 102, no. 2, pp. 595–601, 2018, doi: 10.1111/jace.15814.

[132] J. P. Kelly and O. A. Graeve, “Mechanisms of pore formation in high-temperature carbides: Case study of TaC prepared by spark plasma sintering,” *Acta Mater.*, vol. 84, pp. 472–483, 2015, doi: 10.1016/j.actamat.2014.11.005.

[133] E. Novitskaya *et al.*, “Current assisted extrusion of metallic alloys: Insight into microstructure formation and mechanical properties,” *Mater. Sci. Eng. A*, vol. 717, no. January, pp. 62–67, 2018, doi: 10.1016/j.msea.2018.01.076.

[134] J. T. Cahill, V. R. Vasquez, S. T. Misture, D. Edwards, and O. A. Graeve, “Effect of Current on Diffusivity in Metal Hexaborides: A Spark Plasma Sintering Study,” *ACS Appl. Mater. Interfaces*, vol. 9, no. 42, pp. 37357–37363, 2017, doi: 10.1021/acsami.7b04563.

[135] J. T. Cahill *et al.*, “Phase Stability of Mixed-Cation Alkaline-Earth Hexaborides,” *Cryst. Growth Des.*, vol. 17, no. 6, pp. 3450–3461, 2017, doi: 10.1021/acs.cgd.7b00391.

[136] J. P. Kelly *et al.*, “Designing in situ and ex situ bulk metallic glass composites via spark plasma sintering in the super cooled liquid state,” *Mater. Des.*, vol. 93, pp. 26–38, 2016, doi: 10.1016/j.matdes.2015.12.130.

[137] O. A. Graeve, M. S. Saterlie, R. Kanakala, S. D. De La Torre, and J. C. Farmer, “The kinetics of devitrification of amorphous alloys: The time-temperature-crystallinity diagram describing the spark plasma sintering of Fe-based metallic glasses,” *Scr. Mater.*, vol. 69, no. 2, pp. 143–148, 2013, doi: 10.1016/j.scriptamat.2013.02.019.

[138] K. Sinha, B. Pearson, S. R. Casolco, J. E. Garay, and O. A. Graeve, “Synthesis and consolidation of BaAl2Si2O 8:Eu: Development of an integrated process for luminescent smart ceramic materials,” *J. Am. Ceram. Soc.*, vol. 92, no. 11, pp. 2504–2511, 2009, doi: 10.1111/j.1551-2916.2009.03242.x.

[139] O. A. Graeve *et al.*, “Spark plasma sintering of Fe-based structural amorphous metals (SAM) with Y2O3 nanoparticle additions,” *Mater. Lett.*, vol. 62, no. 17–18, pp. 2988–2991, 2008, doi: 10.1016/j.matlet.2008.01.092.

[140] J. P. Kelly and O. A. Graeve, “Spark Plasma Sintering as an Approach to Manufacture Bulk Materials: Feasibility and Cost Savings,” *Jom*, vol. 67, no. 1, pp. 29–33, 2015, doi: 10.1007/s11837-014-1202-x.

[141] Z. A. Munir, U. Anselmi-Tamburini, and M. Ohyanagi, “The effect of electric field and pressure on the synthesis and consolidation of materials: A review of the spark plasma sintering method,” *J. Mater. Sci.*, vol. 41, no. 3, pp. 763–777, 2006, doi: 10.1007/s10853-006-6555-2.

[142] O. Guillon *et al.*, “Field-assisted sintering technology/spark plasma sintering: Mechanisms, materials, and technology developments,” *Adv. Eng. Mater.*, vol. 16, no. 7, pp. 830–849, 2014, doi: 10.1002/adem.201300409.

[143] Z. A. Munir and M. Ohyanagi, “Perspectives on the spark plasma sintering process,” *J. Mater. Sci.*, vol. 56, no. 1, pp. 1–15, 2021, doi: 10.1007/s10853-020-05186-1.

[144] R. Bjørk, V. Tikare, H. L. Frandsen, and N. Pryds, “The effect of particle size distributions on the microstructural evolution during sintering,” *J. Am. Ceram. Soc.*, vol. 96, no. 1, pp. 103–110, 2013, doi: 10.1111/jace.12100.

[145] S. A. Ghaffari, M. A. Faghihi-Sani, F. Golestani-Fard, and H. Mandal, “Spark plasma sintering of TaC-HfC UHTC via disilicides sintering aids,” *J. Eur. Ceram. Soc.*, vol. 33, no. 8, pp. 1479–1484, 2013, doi: 10.1016/j.jeurceramsoc.2013.01.017.

[146] L. Silvestroni and D. Sciti, “Sintering behavior, microstructure, and mechanical properties: A comparison among pressureless sintered ultra-refractory carbides,” *Adv. Mater. Sci. Eng.*, vol. 2010, no. 1994, 2010, doi: 10.1155/2010/835018.

[147] C. Zhang, A. Gupta, S. Seal, B. Boesl, and A. Agarwal, “Solid solution synthesis of tantalum carbide-hafnium carbide by spark plasma sintering,” *J. Am. Ceram. Soc.*, vol. 100, no. 5, pp. 1853–1862, 2017, doi: 10.1111/jace.14778.

[148] A. I. Gusev, “Phase diagrams for pseudo-binary carbide systems TiC-NbC, TiC-TaC, ZrC-NbC, ZrC-TaC, and HfC-TaC,” *Russ. J. Phys. Chem.*, vol. 59, no. 3, pp. 579–584, 1985.

[149] S. A. Ghaffari, M. A. Faghihi-Sani, F. Golestani-Fard, and M. Nojabayy, “Diffusion and solid solution formation between the binary carbides of TaC, HfC and ZrC,” *Int. J. Refract. Met. Hard Mater.*, vol. 41, pp. 180–184, 2013, doi: 10.1016/j.ijrmhm.2013.03.009.

[150] A. Nino, T. Hirabara, S. Sugiyama, and H. Taimatsu, “Preparation and characterization of tantalum carbide (TaC) ceramics,” *Int. J. Refract. Met. Hard Mater.*, vol. 52, pp. 203–208, 2015, doi: 10.1016/j.ijrmhm.2015.06.015.

[151] Wendell S. Williams, “The Thermal Conductivity of Metallic Ceramics,” *Jom*, vol. 50, no. June, pp. 62–66, 1998.

[152] Y. Yang, J. H. Perepezko, and C. Zhang, “Oxidation synthesis of Hf6Ta2O17 superstructures,” *Mater. Chem. Phys.*, vol. 197, pp. 154–162, 2017, doi: 10.1016/j.matchemphys.2017.04.055.

[153] S. J. McCormack, R. J. Weber, and W. M. Kriven, “In-situ investigation of Hf6Ta2O17 anisotropic thermal expansion and topotactic, peritectic transformation,” *Acta Mater.*, vol. 161, pp. 127–137, 2018, doi: 10.1016/j.actamat.2018.08.029.

[154] A. Nisar, C. Zhang, B. Boesl, and A. Agarwal, “Synthesis of Hf6Ta2O17 superstructure via spark plasma sintering for improved oxidation resistance of multi-component ultra-high temperature ceramics,” *Ceram. Int.*, vol. 49, no. 1, pp. 783–791, 2023, doi: 10.1016/j.ceramint.2022.09.050.